# Diverse and highly differentiated lava suite in Jezero crater, Mars: Constraints on intracrustal magmatism revealed by Mars 2020 PIXL

*Diverse and highly differentiated lava suite on Mars*


**Authors**

Mariek E. Schmidt,[1]* Tanya V. Kizovski,[1†] Yang Liu,[2] Juan D. Hernandez-Montenegro,[3] Michael M.Tice,[4] Allan H. Treiman,[5] Joel A. Hurowitz,[6] David A. Klevang,[7] Abigail L. Knight,[8] Joshua Labrie,[1] Nicholas J. Tosca,[9] Scott J. VanBommel,[8] Sophie Benaroya,[10] Larry S. Crumpler,[11] Briony H.N. Horgan,[12] Richard V. Morris,[13] Justin I. Simon,[13] Arya Udry,[14] Anastasia Yanchilina,[3] Abigail C. Allwood,[2] Morgan L. Cable,[2] John R. Christian,[8] Benton C. Clark,[15] David T. Flannery,[16] Christopher M. Heirwegh,[2] Thomas L. J. Henley,[1] Jesper Henneke,[7] Michael W. M. Jones,[17] Brendan J. Orenstein,[16] Christopher D. K. Herd[10], Nicholas Randazzo[10], David Shuster[18], Meenakshi Wadhwa[19]

**Affiliations**

[1]Department of Earth Sciences, Brock University, St. Catharines, ON L2S 3A1, Canada
[2]Jet Propulsion Laboratory, California Institute of Technology, Pasadena, CA 91109, USA
[3]Division of Geological and Planetary Sciences, California Institute of Technology, Pasadena, CA 91125, USA
[4] Department of Geology & Geophysics, Texas A&M University, College Station, TX 77843, USA
[5] Lunar and Planetary Institute (USRA), Houston, TX 77058, USA
[6] Department of Geosciences, Stony Brook University, Stony Brook, NY 11794-2100, USA
[7] Technical University of Denmark, DTU Space, Department of Measurement and Instrumentation, Kongens Lyngby, 2800, Denmark
[8] McDonnell Center for the Space Sciences, Department of Earth and Planetary Sciences, Washington University in St. Louis, St. Louis, MO 63130, USA
[9] Department of Earth Sciences, University of Cambridge, Cambridge CB2 3EQ, UK
[10] Department of Earth and Atmospheric Sciences, University of Alberta, Edmonton, Alberta T6G 2E3, Canada
[11] New Mexico Museum of Natural History & Science, Albuquerque, NM 87104, USA
[12] Earth, Atmospheric, and Planetary Sciences, Purdue University, West Lafayette, IN, USA
[13] NASA Johnson Space Center, Houston, TX 77058
[14] Department of Geosciences, University of Nevada Las Vegas, Las Vegas, NV, USA
[15] Space Science Institute, Boulder, CO 80301, USA
[16] School of Earth and Atmospheric Sciences, Queensland University of Technology, Brisbane, QLD 4000, Australia
[17] School of Chemistry and Physics and Central Analytical Research Facility, Queensland University of Technology, Brisbane, QLD 4000, Australia
[18] Department of Earth and Planetary Science, University of California, Berkeley, CA 94720-4767, USA
[19] School of Earth and Space Exploration, Arizona State University, Tempe, AZ 85287-6004, USA

* Corresponding author: mschmidt2@brocku.ca

† Now at Department of Earth and Space, Royal Ontario Museum, Toronto, ON M5S 2C6, Canada

**Abstract**
The Jezero crater floor features a suite of related, iron-rich lavas that were examined and sampled by the Mars 2020 rover *Perseverance*, and whose textures, minerals and compositions were characterized by the Planetary Instrument for X-ray Lithochemistry (PIXL). This suite, known as the Máaz formation (fm), includes dark-toned basaltic/trachy-basaltic rocks with intergrown pyroxene, plagioclase feldspar, and altered olivine and overlying trachy-andesitic lava with reversely zoned plagioclase phenocrysts in a K-rich groundmass. Feldspar thermal disequilibrium textures indicate they were carried from their crustal staging area. Bulk and mafic minerals have very high FeO and low MgO to $FeO_{total}$ ratios, which are partially reproduced by thermodynamic models involving high-degree fractional crystallization of a gabbroic assemblage and possibly also assimilation of iron-rich basement. Together, these *in-situ* constraints on petrogenesis provide a uniquely detailed record of intracrustal processes beneath Jezero crater during a time period not represented by Mars samples to date.

**Teaser**
Suite of iron-rich lavas provide a unique record of intracrustal crystallization, storage, and assimilation processes on Mars.

## MAIN TEXT

### Introduction

On terrestrial planets, the diversity of igneous rocks, that form by the solidification of magmas, reflect the composition of magma source regions (mantle), as well as a wide range of physical and chemical processes that segregate and mix melts from residual and accumulated crystals. Magma differentiation refers to any process that leads to a change in magma composition, including the removal of early crystalline products called fractional crystallization, and the remelting and assimilation of earlier generations of igneous rock (*1*). Differentiated, or 'evolved' magmas give insight to complementary (but otherwise hidden) crystalline materials that accumulated and built the continental crusts of the Earth (*2*, *3*) and likely the highlands of other terrestrial planets like Mars (e.g., (*4*)). Thus, differentiated magmas represent valuable windows into the dynamics and growth of planetary crusts.

Evolved igneous rock compositions on Mars have been identified among meteorites and chemical and spectral analyses from landed and orbital missions, and include iron- and feldspar-rich lithologies (*5*–*7*). Their compositions and mineral assemblages suggest extensive crystallization of basaltic parent magmas. Compared to basalts on Earth, martian basalts, including those analyzed *in-situ* or in meteorite collections to date have higher iron (*8*), appear more reduced (*9*, *10*), and may have had lower $H_2O$ contents (*11*), which affects the resulting physical and chemical characteristics of the martian crust (*12*, *13*).

Early in Mars' history, a thick lithosphere could have formed relatively rapidly (*14*), but its rate of further crustal growth would have been limited over time by its stagnant lid tectonic regime,

where heat loss occurs via conduction through a rigid plate (*15*). Mars' early mantle is inferred to have contained more water than at present (*16*), which would have enhanced melting, lowered melt viscosity, and thereby led to greater upward melt migration and crustal growth. In the absence of tectonic-driven recycling, decreasing fluxes of volatiles from Mars' mantle likely led to diminished effects of water on crustal growth rates (*15*, *17*). The transition to modern-day volcanism and crustal thickening driven by mantle plumes likely occurred at ~3.5 Ga, in the Early Hesperian (*18*). Around the same time, a decrease in degree of mantle melting is suggested by lower ratios of orthopyroxene:clinopyroxene in Hesperian terrains compared to older (>3.5 Ga) Noachian terrains (*19*).

The extent that martian intracrustal igneous processes, including crystallization and assimilation, have modified magmas and remade its crust is an open question for Mars, although the martian meteorites provide some clues. Among the augite-rich nakhlite meteorites, variable assimilation of basaltic crust is evidenced by Os isotopes (*20*). The shergottitic meteorites, which are generally basaltic and thought to have formed by high degrees of mantle melting (*21*) in the presence of minor amounts of water (14-73 ppm $H_2O$; (*11*, *22*)), followed by closed-system fractional crystallization (e.g., (*23*, *24*)), variations in light rare earth elements (LREE) indicate incorporation of an ancient enriched component (*25*, *26*). The iron-rich basaltic shergottite meteorites are among the most differentiated martian magmas (*27*). Their last-to-crystallize assemblages often include minerals with extreme iron enrichments, such as "forbidden zone" clinopyroxenes (*28*, *29*), and fine-grained breakdown products of ferrosilite and pyroxferroite (*27*), that are not found in terrestrial basalts crystallized at low pressure.

Importantly, while the martian meteorites provide invaluable information about Mars' mantle, they lack geologic context, with the majority crystallizing in the late Amazonian (<700 Ma; (*30*)). Only orthopyroxenite Allan Hills (ALH) 84001 and components in the martian regolith breccias (Northwest Africa, NWA 7034 and pairs) are pre-Noachian and older than 4.1 Ga (*31*, *32*). Thus, martian meteorites provide a limited view of Mars' igneous history and the extent to which martian magmas differentiated in the crust at other times, such as during the Noachian/Hesperian transition, is left unconstrained.

The *Mars 2020 Perseverance* rover, which landed in Jezero crater, a ~50 km Noachian age impact crater, has encountered and sampled late Noachian to Hesperian aged igneous rocks (*33*) and is expected to encounter and collect early Noachian basement lithologies that span this key transition in martian geological evolution (*34*). On the Jezero crater floor (Fig. 1), *Perseverance* investigated a suite of evolved, Fe-rich clinopyroxene-bearing basaltic to trachy-andesitic lavas, comprising the Máaz formation (fm) (*35*, *36*). The emplacement age(s) of Máaz fm lavas is not known, although it must be older than the impact crater age of its exposed surface - ~2 Ga (*37*), which reflects a complex history of exhumation after burial by Jezero crater lake, fan/delta, and transient eolian sedimentary deposits (*38*). Similar pyroxene-rich compositions, crater-retention, and other morphological characteristics possibly relate the Máaz fm to a widespread Circum-Isidis mafic capping unit outside the crater (*39*).

Here, we present micro-textural, mineralogical and bulk compositional data collected by the Planetary Instrument for X-ray Lithochemistry (PIXL; (*40*)) for Máaz fm outcrops at a resolution that has proven critical for identifying Jezero crater floor lithologies as igneous (*33*, *41*). To

evaluate key outcrops, *Perseverance* used an abrasion bit to create ~5 cm diameter, <1 cm deep circular abrasion patches that were analyzed *in-situ* by microscopic imaging and chemical and mineralogical analytical instruments, including PIXL and SHERLOC (Scanning Habitable Environments with Raman and Luminescence for Organics and Chemicals; (*42*)). PIXL results revealed rocks composed of interlocking mineral grains, some with compositions like the latest-stage iron-rich mineral assemblages in the Fe-rich shergottites (*29*, *43–45*). SHERLOC results complement PIXL by identifying certain anhydrous and hydrous ($H_2O$ & OH) phases by Raman spectroscopy and fluorescent spectral features that may be attributed to organics and(or) rare earth elements (REE's) under excitation by deep ultraviolet radiation (*46*, *47*).

Comparison of Máaz outcrops examined by PIXL indicates that the formation comprises a genetically related igneous suite. As the Máaz lavas range to compositions that are significantly more differentiated than the most differentiated shergottitic meteorites, they provide evidence of petrogenesis via extensive crystallization and possible assimilation within the martian crust. *Perseverance* has collected four samples from the Máaz fm (Table S2): a paired sample set of the relatively less evolved (Rochette member) and one of the more evolved Máaz units (Ch'al member). They are planned to be brought back to Earth by Mars Sample Return (*48*, *49*). Laboratory measurements of these samples will afford additional supporting geochemical and geochronological data to test the petrogenetic models developed by the present study. These data will additionally allow characterization of the timing, source reservoirs(s), and process(es) involved in forming the martian crust in the late Noachian to Hesperian time. Unraveling the igneous history of the Máaz fm also provides an important foundation for understanding the nature of aqueous alteration, some of which may have been driven by late-stage devolatilization, possibly during lava flow emplacement (*50*).

**PIXL instrument**

PIXL combines microscopic multispectral imaging (Micro Context Camera, MCC, ~50 μm per pixel) with an X-ray Fluorescence (XRF) spectrometer to map fine-scale (~120 μm X-ray spot) elemental compositions of surface materials, revealing rock textures (*40*). Multiple PIXL scans of varying types (map, line, grid) were conducted for some targets (Table S1). Microscopic images taken by the SHERLOC cameras, including the color WATSON (up to 15.9 μm per pixel) and high-resolution grayscale ACI (Autofocus and Context Imager, up to 10.1 μm per pixel) provide additional texture and context information (*42*).

PIXL bulk chemical composition of a full scan area and(or) for selected regions of interest (ROI) is provided by analyzing sums of individual X-ray spectra, with the position of each spectrum assigned a unique number referred to as a PMC (PIXL Motion Counter). Identification of X-ray diffraction (XRD) peaks superimposed on individual spectra allows interpretations about crystallinity, mineral grain size, and alteration (*51*). Surface topography and diffraction can have a negative influence on the reported elemental concentrations (*51*, *52*). Therefore, to accurately assess chemical variations between individual PMCs, individual X-ray spectra are corrected for effects of surface topography and diffraction to yield corrected elemental concentrations. A complete derivation of the method is presented in the Supplementary Materials.

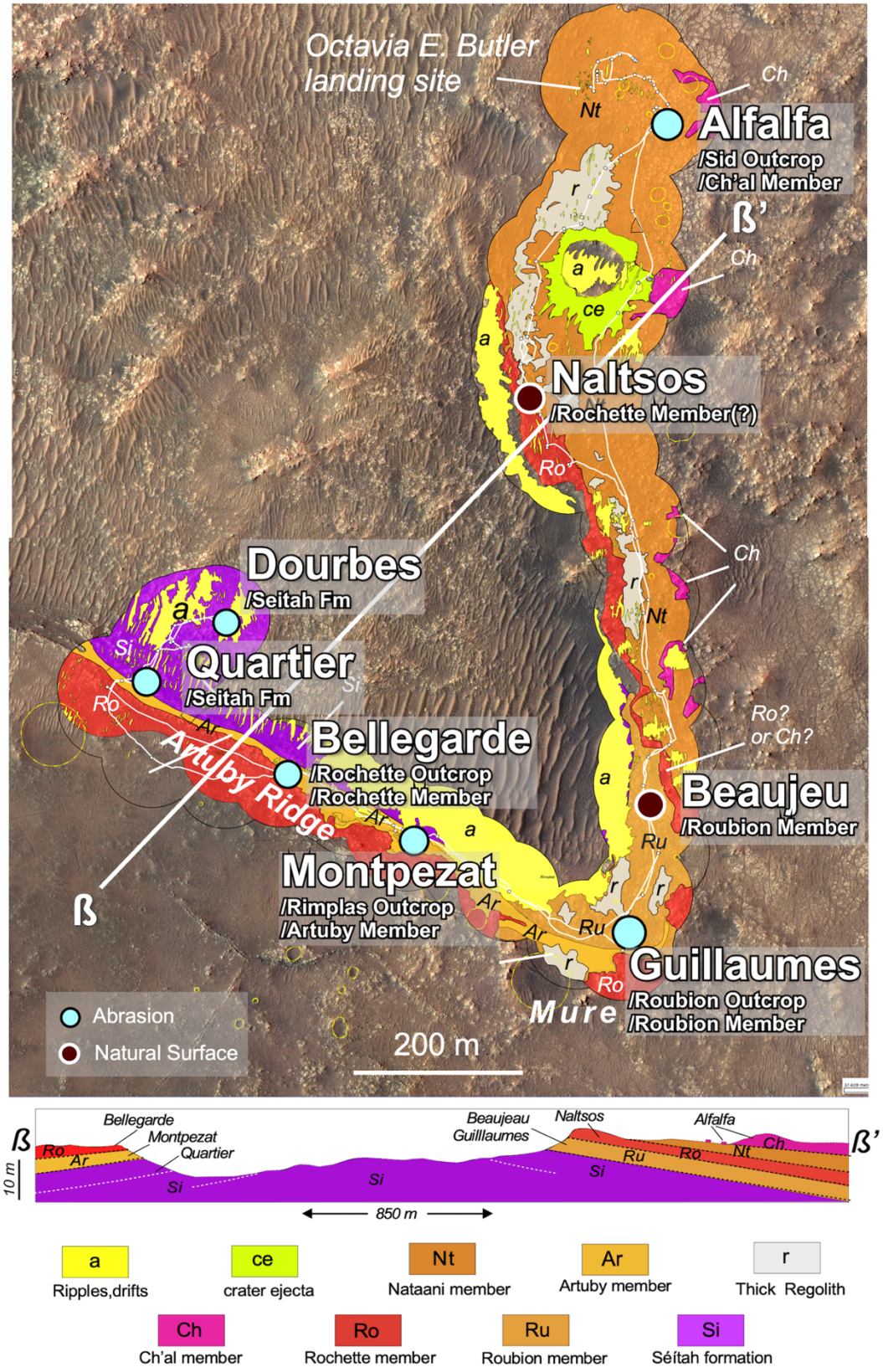
Octavia E. Butler
landing site
Alfalfa
/Sid Outcrop
/Ch'al Member
Naltsos
/Rochette Member(?)
Dourbes
/Seitah Fm
Quartier
/Seitah Fm
Bellegarde
/Rochette Outcrop
/Rochette Member
Artuby Ridge
Montpezat
/Rimplas Outcrop
/Artuby Member
Beaujeu
/Roubion Member
Guillaumes
/Roubion Outcrop
/Roubion Member
Mure
ß
ß'
Ch
Nt
Ro
Ro? or Ch?
Ru
Ar
Si
a
ce
r
Abrasion
Natural Surface
200 m
Bellegarde
Montpezat
Quartier
Beaujeau
Guilllaumes
Naltsos
Alfalfa
10 m
850 m
Ripples,drifts
crater ejecta
Nataani member
Artuby member
Thick Regolith
Ch'al member
Rochette member
Roubion member
Séítah formation

**Fig. 1. Geologic traverse map (53) and interpretive cross section with locations of PIXL analyses**. The stratigraphic positions of *Beaujeau* and *Guillaumes* are somewhat uncertain due to complexity of the exposures along the southern part of the traverse. Both could represent the Nataani member. The *Alfalfa* abrasion is located at the Sid outcrop, a block isolated from the main mass of the Ch'al member possibly by erosional retreat of the Ch'al member margin. Units were observed to dip on the order of 5° to 10° away from the interior of Séítah. The Content member of the Séítah fm is basaltic appears to unconformably overlie layered olivine cumulate wehrlites (54), but is not represented here due to its limited exposure. Two sets of paired core samples for MSR correspond with the *Bellegarde* and *Alfalfa* abrasions. A summary of Máaz names, including core sample names are in Table S2.

The PIXL results provide the clearest picture of the Máaz fm samples before they are returned to Earth by MSR. In addition, mineral grain sizes and compositions allow assessment of what lab-based analyses will be possible by providing important constraints on analytical and sample handling requirements.

**Geologic traverse**

The *Perseverance* rover began exploration in Jezero crater at the Octavia E. Butler (OEB) landing site within a unit defined from orbit as the Crater Floor-fractured rough (CF-fr; (*55*)) that spans ~400 km$^2$ of the central portion of the crater floor. Natural rock surfaces are variably covered by fine-grained dust and a patchy, indurated red coating (Fig. S2, S3). Accumulations of aeolian sand grains and dust may be found within vugs and depressions on and around rock surfaces. Where the rover has traversed (Fig. 1), the crater floor is subdivided into two formations: the stratigraphically higher, pyroxene basalts of the Máaz fm (CF-fr orbital unit) and the underlying olivine cumulate wehrlites of the Séítah fm (CF-F1 from orbit; (*41*, *49*, *53*)). The contact between the Séítah and Máaz formations is covered by aeolian sediments and may be either intrusive or stratigraphic in nature. Sediments of the Jezero delta (*56*) unconformably overlie the igneous units of the crater floor (*57*).

The outcrop expression of the Máaz fm varies both stratigraphically and laterally across the crater floor (*35*, *53*). East of the landing site, the Máaz fm is observed as massive, ventifact boulders that make up the tops of rough hummocks (Ch'al member; *Alfalfa* abrasion) and overlie low-lying, polygonaly fractured, vuggy outcrops (Nataani member; *Naltsos* natural surface). The Roubion member (*Guillaumes* abrasion and *Beaujeu* natural surface) appears to underlie the Nataani member in eroded sections near the Mure outcrop. Máaz fm outcrops to the west of Mure at Artuby ridge and south of Séítah are defined by apparent layers of more resistant dark gray caprock with concentrations of vugs along curvilinear layers (Rochette member; *Bellegarde* abrasion; (*58*). Below layered blocks of the Rochette member that comprise the cliff-forming Artuby ridge, the Máaz fm transitions to knob-forming and round or even recessive and friable layers (Artuby member; *Montpezat* abrasion). While it is generally accepted that the Ch'al/Nataani members represent the stratigraphically highest members, and the Rochette/Artuby members the lowest, no unambiguous contact between them was observed. Likewise, distribution of the Roubion member away from the Mure area is unclear, and thus, the relationship between the Roubion and Rochette/Artuby members is also unknown. Multiple stratigraphic scenarios have been considered to explain the observed geology (*35*). Where

potential contacts between these members are visible, possible weathered paleosurfaces observed from MastCam-Z and SuperCam as well as radar shadow zones from RIMFAX, are consistent with erosion and(or) paleosurfaces and suggest that some time has lapsed between their deposition (*35*, *59*, *60*).

## Results

### Igneous textures

SHERLOC WATSON and PIXL MCC microscopic images of Máaz abraded patches show a range of fine-grained igneous textures, which provide constraints on crystallization history (Fig. 2A, S1, S3, S4). Three of the four abraded targets (*Montpezat*, *Guillaumes*, and *Bellegarde*) are largely devoid of glassy material (holocrystalline) and contain blocky dark- and light-toned crystals with grain sizes of ~0.5 to 2 mm. No obvious intergranular porosity and(or) cement are identified. Irregular to round holes or hollows in the *Guillaumes* abrasion patch are likely primary vesicles with mineral grains surrounding or projecting into some holes, which (if vesicles) suggests that a crystalline framework existed prior to their formation (i.e., diktytaxitic texture). At the wind-scoured outcrop Rochette (Fig. S2D), the site of the *Bellegarde* abrasion, circular holes (likely vesicles; ~0.5 cm) are observed in the lower part of the outcrop. The Bellegarde abrasion reveals potential amygdules, where secondary, bright white phase(s) occupy pre-existing voids (or vesicles). Red-brown alteration variably occurs on abraded surfaces and is found along throughgoing, irregular cracks (*Guillaumes*), rimming vugs (*Bellegarde*), and as discrete areas where secondary phases appear to replace primary igneous minerals (*Montpezat 2*). The fourth abraded target, *Alfalfa* has textural features consistent with a two-stage crystallization history, where relatively large light-toned laths (up to 5 mm length) and smaller darker-toned grains (~ 1 mm long axis) formed by slow cooling are surrounded by a red-brown, fine-grained groundmass that cooled more rapidly (i.e., porphyritic texture).

Details of the Máaz fm fabrics and high temperature crystalline phases typical of igneous rocks are well-defined by PIXL element abundance and diffraction maps (Fig. 2B-D, S5). PIXL also affords a view of the rock texture and make up of *Beaujeu*, a dust and regolith-covered and coated natural surface target. Elongated regions that are rich in Ca and Fe correspond with the dark-toned (black to dark green) regions in WATSON microscopic images (Figure S3) and are interpreted to be Ca-rich pyroxene grains (purple in Fig. 2C). In the *Alfalfa* scan, pyroxene occurs as ~1 mm microphenocrysts and in clots (glomerocrysts) along with various Al-, Ti-, and P-bearing phases, such as plagioclase feldspar, FeTi oxide, and Ca-phosphates (likely apatite and merrillite).

Light-toned prismatic crystal laths in Alfalfa are Al-rich (green in Fig. 2C) and identified as plagioclase feldspar based on chemistry determined by PIXL. The Al-rich laths were also analyzed by SHERLOC, which found Raman spectra suggestive of a non-olivine, non-pyroxene silicate, tentatively identified as amorphous silicate or feldspar (*61*). Red regions with abundant Fe in Fig. 2C include fine-grained Fe and FeTi oxide minerals and larger (1-2 mm) zones comprised of Fe-silicate phases that are interpreted to be altered olivine. Ca-phosphate (blue in Fig. 2D) mostly occurs at the interstices between larger silicate minerals. A fine-grained KSi-rich phase that also contains Al (green in Fig. 2D) is most apparent as groundmass in the *Alfalfa* abrasion where it makes up ~60% of the scan area. A similar KSi-rich phase also occurs in the

other Máaz targets in varying amounts between the prismatic silicate grains as mesostasis, and its abundance generally corresponds with decreasing proportions of Ca-rich pyroxene.

Secondary S and Cl-rich salts (Fig. 2E) and other alteration phases in Máaz rocks are identified by PIXL and other M2020 instruments, including SHERLOC and SuperCam (*33*, *61–63*) and often appear bright white in microscopic images. Salt phases include Ca-sulfate (possible anhydrite) in *Guillaumes* and *Bellegarde*, and Na-perchlorate in *Guillaumes*. A secondary FeSi-rich phase is also identified in *Montpezat 2* and *Alfalfa* in association with olivine and, on the basis of data from PIXL XRF and MCC and SuperCam-IR is interpreted to be serpentinized Fe-rich olivine (hisingerite) with late-stage, adsorbed nonstoichiometric Cl. The chlorine distributions are consistent with concentration of fluid soluble elements and interaction of Máaz fm rocks with late percolating aqueous fluids in a manner similar to that observed in the underlying Séítah fm (*51*).

The PIXL data also provide insight into crystallinity, fabric and grain size. A minimum ~30-50 μm grain size is required for diffraction peaks to be identified in the PIXL X-ray spectra (*51*). The generally non-diffracting (i.e., PIXL amorphous; (*51*)) KSi-rich groundmass in the *Alfalfa* scan is therefore likely aphanitic (or glassy) with a <50 μm grain size. Secondary phases also do not typically exhibit diffraction peaks, including sulfates, perchlorates, hydrated Fe-oxides, and on natural surfaces, airfall dust and coatings, indicating a <50 μm grain size. In contrast, most primary igneous phases do have observable diffraction peaks. Contiguous regions where multiple PMCs display similar diffraction characteristics in terms of peak position and relative intensity are interpreted to represent single crystals. The sizes and shapes of monocrystalline grains can therefore be investigated even when compositionally similar grains are nearby (Table 3). In the *Montpezat 2* scan (Fig. 2F), two Fe-rich regions (~0.4 mm across) are revealed to comprise a single olivine crystal on the basis of their similar diffraction peak positions. The olivine crystal is surrounded and bisected by a non-diffracting region that is relatively enriched in Cl (Fig. 2E) and likely secondary. In the *Alfalfa* scan, two large (~5 mm), Al-rich rectangular diffracting regions (pl-1 and pl-2; Fig. 2A, C) are interpreted to represent single crystalline feldspar crystals that are not extensively altered or shocked. Variations in diffraction peak positions within these feldspars (Fig. 2F) produce concentric and mosaic patterns that suggest the presence of compositional zoning, thermal disequilibrium, and/or minor secondary alteration.

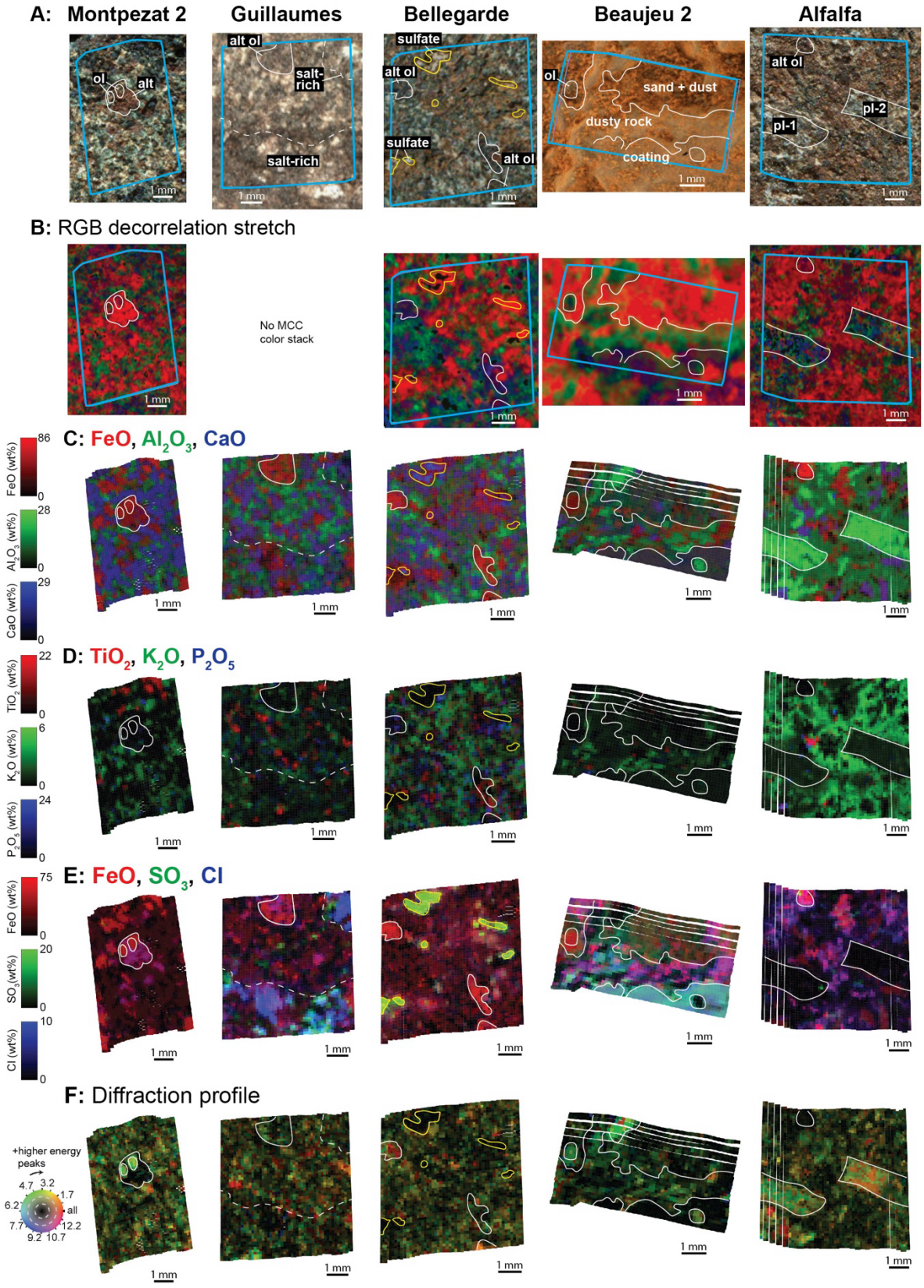
A: Montpezat 2
Guillaumes
Bellegarde
Beaujeu 2
Alfalfa
ol
alt
alt ol
salt-rich
salt-rich
sulfate
alt ol
sulfate
alt ol
ol
sand + dust
dusty rock
coating
alt ol
pl-2
pl-1
1 mm
B: RGB decorrelation stretch
No MCC color stack
C: FeO, Al2O3, CaO
FeO (wt%) 86 0
Al2O3 (wt%) 28 0
CaO (wt%) 29 0
D: TiO2, K2O, P2O5
TiO2 (wt%) 22 0
K2O (wt%) 6 0
P2O5 (wt%) 24 0
E: FeO, SO3, Cl
FeO (wt%) 75 0
SO3 (wt%) 20 0
Cl (wt%) 10 0
F: Diffraction profile
+higher energy peaks
4.7 3.2 1.7 all 12.2 10.7 9.2 7.7 6.2

**Fig. 2. Maaz fm proximity science target microscopic images and PIXL element and diffraction similarity maps.** A: Microscopic images of PIXL map scan areas outlined in blue for Máaz fm targets. *Montpezat 2* (merged SHERLOC WATSON I1_0347_0697764632_210FDR_N0092982SRLC00003_000095J01.IMG and PIXL MCC PCW_0349_0697957868_000RCM_N00929821235358790003OLUJ04.png), *Guillaumes* (merged SHERLOC WATSON SI1_0161_0681260800_941FDR_N0060000SRLC00056_000095J01.IMG and PIXLMCC PCW_0166_0681701844_000RCM_N00600000631116810003075J07.png), *Bellegarde* (merged SHERLOC WATSON SI1_0186_0683473384_832FDR_N0070000SRLC00005_000095J02.IMG and PIXL MCC PCW_0187_0683484439_000RCM_N00700000699274310005075J06.png), *Beaujeu 2* (merged SHERLOC WATSON SI1_0142_0679525747_140FDR_N0051812SRLC00003_000095J02.IMG and PIXL MCC PCW_0139_0679308360_000RCM_N00518120532812810005075J11.png Origin Scan: 053281281), and *Alfalfa* (merged SHERLOC WATSON SI1_0370_0699810950_417FDR_N0110108SRLC00036_000095J01.IMG and PIXL MCC PCW_0369_0699719117_000RCM_N01101081307448340003075J01.png). Labeled fields in A point to phases or regions that are discussed in the text and for correlation between images. B: Decorrelation stretched images of MCC multispectral channels NIR-Green-Blue (723 nm, 535 nm, 447 nm). C: PIXL Red-Green-Blue (RGB) maps for the Máaz fm targets, corrected for effects of topography and diffraction (Table S6; Supplementary Materials). Red is FeO, green is $Al_2O_3$, and blue is CaO. D: Red is $TiO_2$, green is $K_2O$, and blue is $P_2O_5$. E: Red is FeO, green is $SO_3$, and blue is Cl. For scans where some PMCs are greater than the color scale, these are represented by the brightest regions. F: X-ray diffraction profiles. In these maps, diffraction patterns for each PMC are represented by hues on the color wheel where the overall magnitude of diffraction (in natural log units from 0-3 relative to a non-diffracting baseline) is represented by color intensity (black = no diffraction, bright colors = strong diffraction), and the different colors represent combinations of diffraction peaks observed in eight energy bins from 0.8-12.8 keV. Black areas on the maps where no diffraction peaks are identified indicate that these regions are either amorphous or micro-crystalline below the resolution of PIXL (<30-50 μm). Because diffraction patterns reflect a combination of mineral identity and crystallographic orientation, detection of the same pattern (color) over multiple contiguous PIXL spots generally indicates a large monomineralic crystalline domain. Thus, in these maps, single-color grains correspond to monocrystalline minerals. See text for more details.

**Bulk igneous compositions**

To find bulk igneous compositions, we focus on regions containing low concentrations of S and Cl (i.e., "low salt"; Fig. 3; Table S4). Also, regions of FeSi-rich alteration that are interpreted to be altered olivine (Fig. 3; Tables S4, S5; next section describes identification of olivine and other minerals) are included in the bulk sum, where alteration is likely largely isochemical and any excess Cl is subtracted because it is thought to have been imparted late in the sequence. The total regions considered "low salt" make up 55% (*Guillaumes*) to 95% (*Montpezat*) of the PMCs for the different Máaz targets. A final correction on the initial bulk sum, removing remaining NaCl

and $CaSO_4$, is then performed to generate corrected igneous bulk compositions for the abraded Máaz fm targets (Table 1).

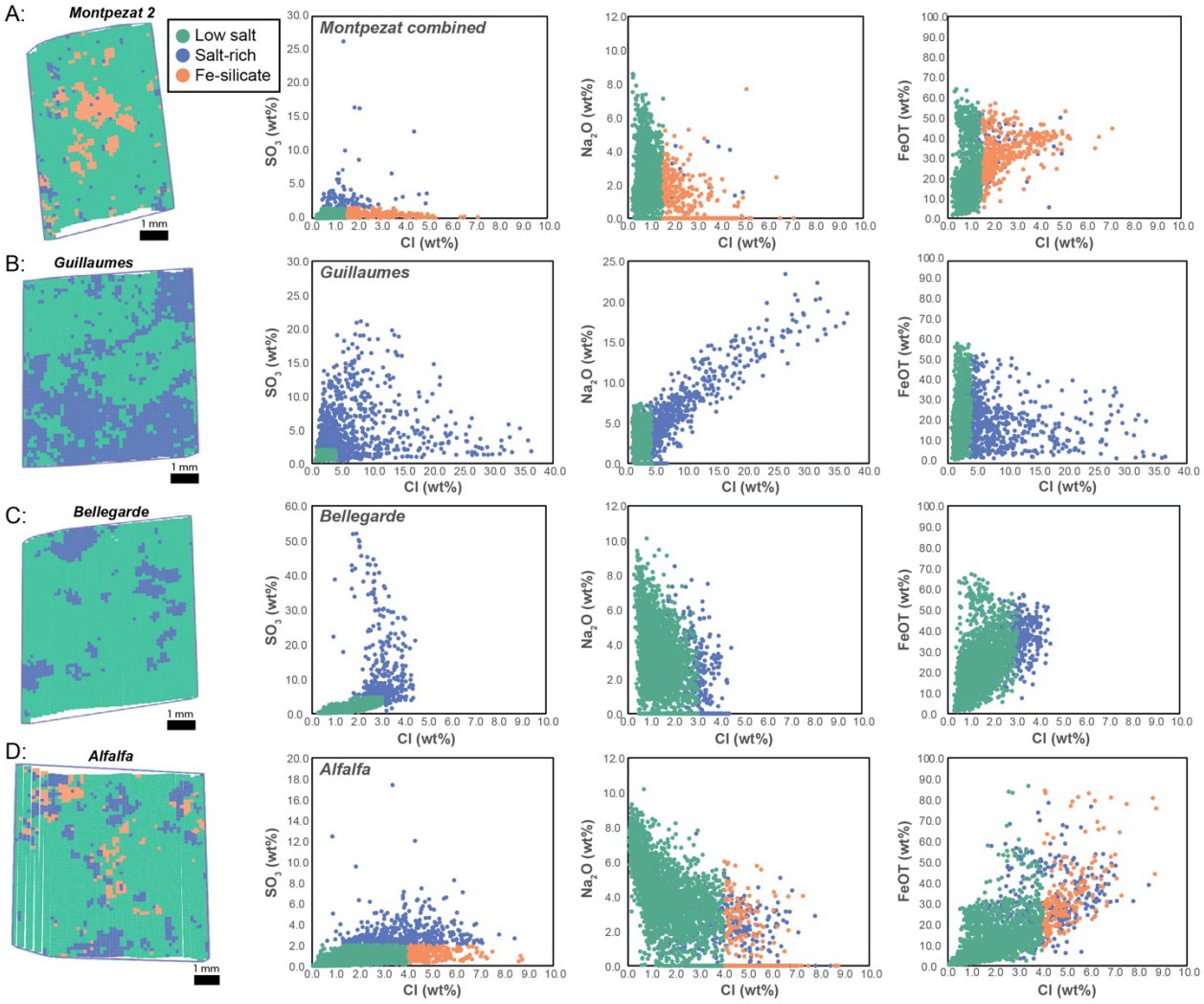


**Fig. 3. Summary of regions of interest (ROI) used for determining corrected bulk compositions in Máaz fm abrasion target scans.** ROIs include low salt, salt-rich, and Fe-silicate alteration that is also enriched in Cl and are defined in Table S4 caption. Targets are listed in order of decreasing Mg#. For each of the four abraded Máaz fm Targets, the ROI map and binary plots of $SO_3$ vs. Cl, $Na_2O$ vs. Cl, and $FeO_T$ vs. Cl are shown. A: *Montpezat 2*, binary plots also include points from *Montpezat 1* line scan; B: *Guillaumes*; C: *Bellegarde*; and D: *Alfalfa*.

Corrected igneous bulk compositions range in composition from basaltic/trachybasaltic to trachyandesitic, plotting on a total alkali versus silica diagram (Fig. 4A) within fields of other Mars magma compositions from landed and meteorite datasets. Corrected PIXL bulk sum compositions of Séitah fm wehrlites (*41*) are also plotted for comparison, although these include accumulated olivine and likely do not represent igneous melts. The Máaz corrected igneous

compositions are similar and within error of SuperCam average igneous compositions determined by laser induced breakdown spectroscopy (*36*) for the holocrystalline abraded targets (*Guillaumes* and *Bellgarde*), but with slightly higher total alkalis (Fig. 4A-D). For coarser grained *Alfalfa*, SuperCam yields lower average $K_2O$ and $Al_2O_3$ concentrations (Figure S10E-F), likely reflecting its heterogeneous porphyritic texture.

**Table 1. Corrected igneous bulk compositions of the Máaz fm abraded target**

| | ***Montpezat*** | | ***Guillaumes*** | | ***Bellegarde*** | | ***Alfalfa*** | |
|---|---|---|---|---|---|---|---|---|
| *Sol* | *347-342** | | *167* | | *187* | | *369* | |
| *Máaz mb* | *Artuby* | | *Roubion* | | *Rochette* | | *Ch'al* | |
| *Outcrop* | *Rimplas* | | *Roubion* | | *Rochette* | | *Sid* | |
| | wt% | +/- | wt% | +/- | wt% | +/- | wt% | +/- |
| $Na_2O$ | 3.3 | 0.8 | 3.7 | 0.7 | 3.9 | 0.3 | 5.7 | 0.6 |
| MgO | 6.2 | 0.3 | 2.7 | 0.7 | 2.0 | 0.6 | 0.7 | 0.3 |
| $Al_2O_3$ | 6.6 | 0.3 | 9.4 | 0.4 | 7.9 | 0.4 | 13.2 | 0.6 |
| $SiO_2$ | 48.9 | 2.4 | 48.3 | 2.3 | 48.5 | 2.3 | 61.7 | 3.0 |
| $P_2O_5$ | 1.4 | 0.5 | 2.1 | 0.6 | 3.1 | 0.6 | 1.4 | 0.5 |
| $K_2O$ | 0.8 | 0.3 | 0.9 | 0.3 | 1.2 | 0.4 | 2.1 | 0.5 |
| CaO | 10.0 | 0.5 | 8.0 | 0.4 | 7.2 | 0.4 | 4.6 | 0.3 |
| $TiO_2$ | 1.8 | 0.6 | 2.0 | 0.5 | 2.8 | 0.7 | 0.9 | 0.4 |
| $Cr_2O_3$ | 0.1 | 0.1 | 0.0 | 0.0 | 0.0 | 0.0 | 0.0 | 0.0 |
| MnO | 0.5 | 0.2 | 0.5 | 0.2 | 0.4 | 0.2 | 0.2 | 0.2 |
| $FeO_T$ | 20.3 | 1.0 | 22.3 | 1.1 | 22.9 | 1.1 | 9.4 | 0.5 |
| Sr | 0.04 | 0.03 | 0.08 | 0.03 | 0.04 | 0.03 | 0.08 | 0.03 |
| SUM | 100 | | 100 | | 100 | | 100 | |
| Mg# | 35.2 | | 17.7 | | 13.6 | | 11.2 | |
| CIPW† | | | | | | | | |
| *Qz* | 0 | | 0 | | 1.7 | | 8.6 | |
| *Pl* | 28.8 | | 37.7 | | 33.5 | | 51.3 | |
| *Or* | 4.7 | | 5.3 | | 7.1 | | 12.1 | |
| *Ne* | 0 | | 0 | | 0 | | 0 | |
| *Di* | 34.1 | | 17.0 | | 13.0 | | 8.4 | |
| *Hy* | 9.8 | | 22.4 | | 26.9 | | 12.2 | |
| *Ol* | 11.4 | | 4.3 | | 0 | | 0 | |
| *Il* | 3.4 | | 3.0 | | 5.3 | | 1.7 | |
| *Mt* | 4.9 | | 5.6 | | 5.54 | | 2.7 | |
| *Ap* | 3.0 | | 4.9 | | 7.2 | | 3.1 | |
| *Ch* | 0.2 | | 0 | | 0 | | 0 | |
| *Total* | *100.2* | | *99.9* | | *99.9* | | *100.1* | |

Corrected compositions calculated for low salt regions of PIXL scan areas (Fig. 3), defined in Table S4 caption, correcting for remaining Cl and $SO_3$ (subtracting $SO_3$ as $CaSO_4$ and Cl as NaCl, except for *Alfalfa* where Cl=0), and renormalizing to 100%. Raw bulk chemistry of each abraded patch is listed in Table S4. Abraded rock targets are listed in order of decreasing Mg#, defined as molar Mg/(Mg+Fe)*100.

**Montpezat* is the combined bulk sum of sol 347 line and sol 348 map scans.

†Cross Iddings Pirsson and Washington (CIPW; (*65*)) normative mineralogy in wt% was calculated assuming $Fe^3/Fe_T$=0.15, which is consistent with differentiated shergottites (*66*) and alkali-rich Gusev basalts (*10*). *Qz* quartz, *Pl* plagioclase, *Or* orthoclase, *Ne* nepheline, *Di* diopside, *Hy* hypersthene, *Ol* olivine, *Il* ilmenite, *Mt* magnetite, *Ap* apatite, *Ch* chromite.

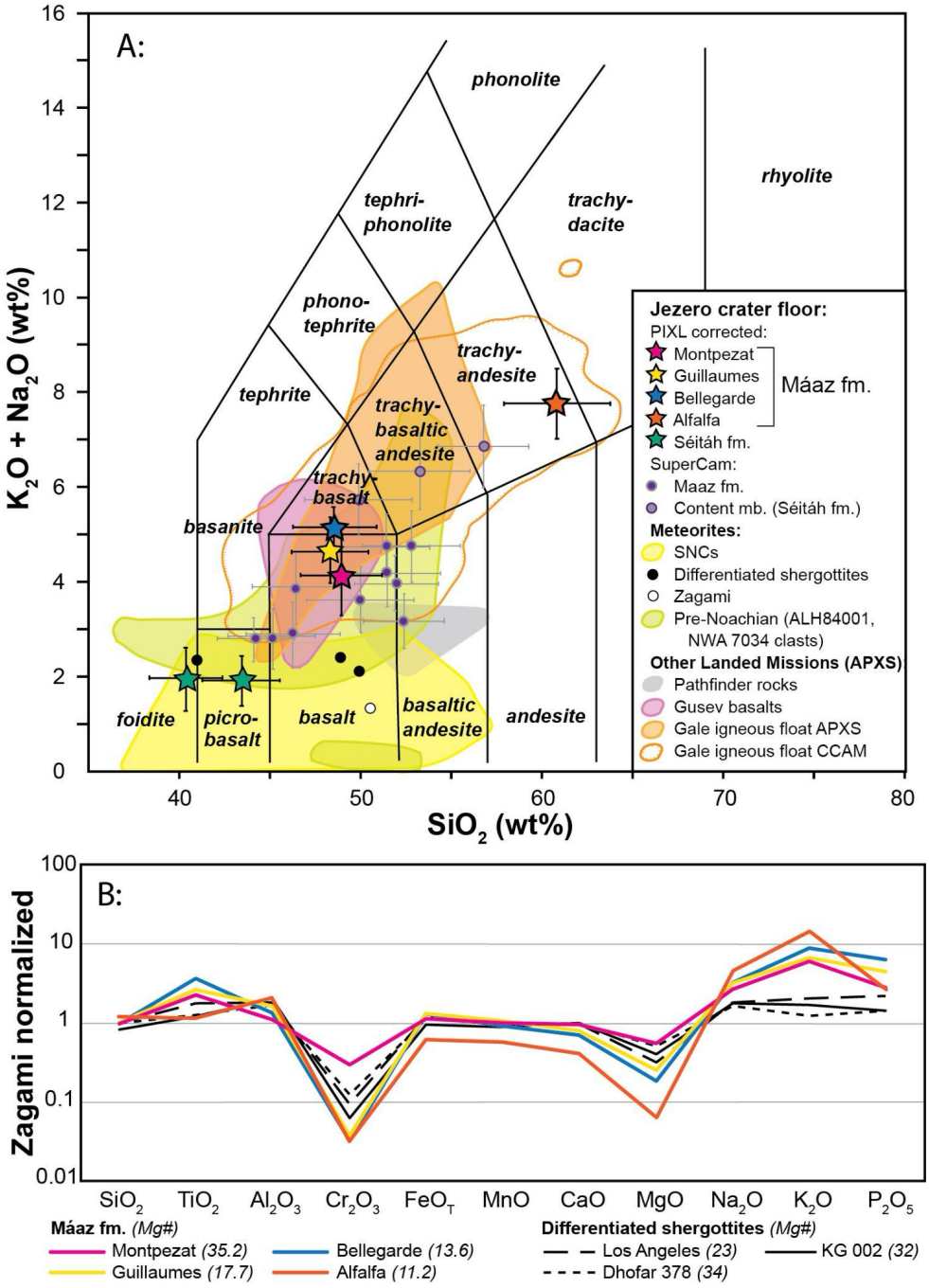


**Fig. 4. Diagrams comparing PIXL corrected igneous bulk compositions and Mars igneous compositions.** A: Total alkali vs. silica diagram for Mars igneous compositions, including Jezero crater Máaz and Séitáh fm PIXL abraded targets raw and corrected igneous bulk compositions and SuperCam natural surface and abrasion patch average compositions (Table 1; (*36*, *41*, *67–70*)). Basaltic shergottite Zagami and differentiated shergottites are also plotted (*27*, *43*, *64*, *71*, *72*). B: Basaltic shergottite Zagami-normalized element abundance diagram with Máaz fm abraded targets and select evolved martian meteorites (*27*, *43*, *64*, *72*).

Low abundances of igneous compatible elements (MgO as low as 0.7 wt% for *Alfalfa*, Ni below detection) and relatively high $Al_2O_3$ relative to a martian basalt (Zagami shergottite meteorite; (*64*); Fig. 4B) are consistent with an origin by crystallization of basaltic magma. A high degree of fractional crystallization is indicated by very low Mg# (molar $MgO/(MgO+FeO_{Total})\times100$) values; Mg#'s range from 35.2 for the most primitive basaltic target *Montpezat* to 13.6 for trachybasaltic *Bellegarde* and 11.2 for trachyandesitic *Alfalfa*. These Mg#'s overlap with and are lower than the most differentiated of the Fe-rich shergottite meteorites (e.g., Los Angeles Mg#=23; (*27*)) and evolved regolith breccia clasts (NWA 7034 basaltic andesite and trachyandesite Mg#=28-57; (*7*)).

CIPW norm calculations (assuming $Fe^{3+}/Fe_{tot}$=0.15 and 100% crystallization at 1 kbar) found reasonable, hypersthene-normative mineral assemblages (Table 1) that are consistent with igneous compositions. Calculated normative mineralogy represents an equilibrium mineral assemblage and is consistent with but differs in detail from the observed modes and mineral compositions (Tables 2, 3, S5) as is expected. The two more primitive, higher-Mg# Máaz analyses, *Montpezat* and *Guillaumes,* are olivine normative (11.4 and 4.3 wt% olivine, respectively), while *Bellegarde* and *Alfalfa* with lower Mg#'s are slightly and moderately quartz normative (1.7 and 8.6 wt% quartz), respectively. These variations in normative mineralogy suggest the Máaz magmas, if related, evolved from being undersaturated with respect to $SiO_2$ toward having excess $SiO_2$ with increasing differentiation.

Among the Máaz basaltic targets (*Montpezat*, *Guillaumes*, and *Bellegarde*), systematically increasing $TiO_2$, $FeO_T$, $Na_2O$, $K_2O$, and $P_2O_5$ and decreasing CaO and Mg# over a narrow range in $SiO_2$ likely reflect removal of an augite-dominated assemblage (Fig. 2C). Trachyandesitic *Alfalfa* has even lower MgO and CaO, but higher $SiO_2$ and lower $TiO_2$, FeO, and $P_2O_5$, which may suggest fractional crystallization of FeTi oxide (titanomagnetite and/or ulvospinel) and Ca-phosphate (apatite) also occurred, or that its parent magma was depleted in Ti and P.

**Mineral compositions and modes**

Mineral compositions (Tables 2, S5) identified among the Máaz targets further support a magmatic origin involving a high degree of fractional crystallization. Igneous minerals identified and quantified include feldspar, pyroxene, olivine, Fe-oxides, and Ca-phosphates. Grain sizes and modal abundances are compiled in Table 3. The major rock-forming minerals (feldspar, pyroxene, and olivine) compositions were determined using stoichiometric constraints summarized in Table S7. All PIXL analyses of Fe-oxides and Ca-phosphates are mixtures with other minerals due to their small grain sizes. As such, their compositions were inferred by examining mixing trends with surrounding phases, and correlations between major cations (Ca:P, and P:Cl ratios for phosphates, and Fe:Ti:Cr ratios for spinels; see Supplementary Materials for more details).

**Table 2. Máaz formation pyroxene, olivine, and feldspar compositions**

| | *Beaujeu* | | | *Montpezat* | | | *Guillaumes* | | | *Bellegarde* | | | *Alfalfa* | | |
|---|---|---|---|---|---|---|---|---|---|---|---|---|---|---|---|
| *Olivine* | | | | | | | | | | | | | | | |
| Fo | 45.2* | ± | 2.6 | 20.3 | ± | 1.4 | 8.4 | ± | 1.5 | 4.3 | ± | 1.3 | 3.1 | ± | 1.0 |
| *Pyroxene* | | | | | | | | | | | | | | | |
| Wo | 31.8 | ± | 0.9 | 35.2 | ± | 1.4 | 28.8 | ± | 1.2 | 25.8 | ± | 1.0 | 29.6 | ± | 1.3 |
| Fs | 51.7 | ± | 2.2 | 39.0 | ± | 1.8 | 59.6 | ± | 3.0 | 66.5 | ± | 3.3 | 64.8 | ± | 3.2 |
| En | 16.5 | ± | 1.6 | 25.7 | ± | 1.7 | 11.6 | ± | 1.9 | 7.7 | ± | 1.8 | 5.6 | ± | 1.4 |
| *Feldspar* | | | | | | | | | | | | | | | |
| An | 31.8 | ± | 3.7 | 26.7 | ± | 3.8 | 38.2 | ± | 6.1 | 18.6 | ± | 2.4 | 31.6 | ± | 3.4 |
| Or | 4.8 | ± | 1.4 | 14.5 | ± | 3.5 | 10.3 | ± | 2.9 | 10.8 | ± | 2.4 | 5.1 | ± | 1.4 |
| Ab | 63.4 | ± | 13.9 | 58.8 | ± | 14.8 | 51.5 | ± | 16.4 | 70.5 | ± | 12.6 | 63.4 | ± | 12.1 |

Full mineral endmember oxide compositions and elemental ratios are in Table S5. Abbreviations are Fo forsterite, Wo wollastonite, Fs ferrosilite, En enstatite, An anorthite, Or orthoclase, Ab albite. Reported endmember mineral compositions are further corrected for minor amounts of Ca-S and Na-Cl phases. Propagated error uncertainty for each average is reported as ±.
*Higher Fo in olivine of the natural surface target Beaujeu olivine suggests it is not likely in place.

**Table 3. Micro-textures, modes, and grain sizes for Maaz fm targets**

| | *Beaujeu* | *Montpezat* | *Guillaumes* | *Bellegarde* | *Alfalfa* |
|---|---|---|---|---|---|
| Texture: | natural surface (porphyritic) | Micro-gabbroic | Micro-gabbroic | Micro-porphyritic | porphyritic |
| Other descriptors | Coating and soil+dust present | | Vuggy/ vesicular | Sulfate amygdules | |
| Grain size*: | | | | | |
| *Plagioclase* | 1.3 mm | 0.5 mm | 0.4 mm | 0.3–1 mm | 0.6 to >3 mm |
| *Augite* | 0.6 mm | 0.9 mm | 0.5–2 mm | 0.4 mm | 0.3–2 mm |
| *Olivine* | 1 mm | 1.1 mm | 1–2 mm | 1 mm | 2 mm |
| *Fe-Ti oxide* | 0.2 mm | 0.3 mm | 0.3 mm | 0.3 mm | 0.3 mm |
| Normalized modal proportions (area%)†: | | | | | |
| *Plagioclase* | 35 | 33 | 41 | 5 | 34 |
| *Augite* | 5 | 44 | 29 | 25 | 3 |
| *Olivine* | 17 | 10 | 8 | 5 | 3 |
| *Oxides* | 5 | 7 | 18[3] | 31‡ | 3 |
| *KAl-rich meso/gmass* | 38 | 6 | 3 | 34 | 59 |

* The grain sizes reported here are based on the size of 3-10 randomly selected monocrystalline grains determined by diffraction mapping (See Materials and Methods and Figure 2F). In cases where few grains with widely varying sizes were present or where sizes appeared multimodal, size ranges are reported instead of averages.
† Modal proportions are renormalized to 100% after excluding amorphous, high salt, and grain boundary regions. See Methods and Materials section (the pristine areas in Figure S9) and Table S7.
‡ Oxide abundances in the relatively fine-grained targets *Guillaumes* and *Bellegarde* are likely overestimated due to significant mixing with surrounding phases.

## *Pyroxene*

Ca-rich pyroxene endmembers identified in PIXL scans are Fe-rich augites, that contain higher Fe than pyroxenes analyzed by PIXL in the Séitah fm (*41*) and overlap pyroxene rim compositions in shergottites (Fig. 5A). Four of the five targets contain pyroxenes that plot well within the "forbidden zone" of the pyroxene quadrilateral, where pyroxene is not stable at low

pressures <1 kbar (*28*) but could be metastably present at low oxygen fugacities (as in lunar basalts; (*73*, *74*)), related to melt chemistry, or a product of late-stage to subsolidus cooling rates (*75*).

PIXL augite compositions are consistent with those analyzed by SuperCam in the Máaz fm (Fig 5; (*36*)). Compositional differences in detail between the high-Ca pyroxenes in abrasion patches examined by both instruments are a product of the different techniques, natural variability within the rocks, and PIXL's higher sensitivity for S, which allows a correction for $CaSO_4$. Decreasing bulk chemical Mg# variations of the Máaz suite are reflected in decreasing Mg contents in augite (Table 2) as well as in decreasing modal pyroxene abundances (44 to 3 area%; Table 3) and are consistent with increasing degrees of fractional crystallization.

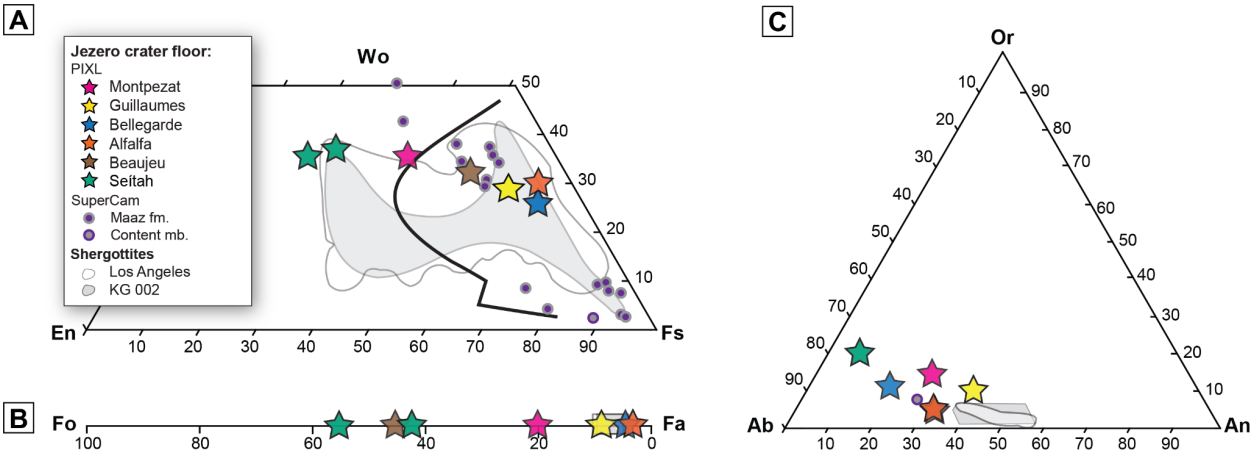


**Fig. 5. Jezero crater floor PIXL mineral endmember compositions.** PIXL data are compiled in Table 2, S5 and (41). Mineral compositions determined from Máaz natural surfaces and abrasion patches by SuperCam (36) as well as compositional fields for early to late-stage minerals found in select evolved martian meteorites are also plotted (43, 44). A: Pyroxene enstatite (En)-wollastonite (Wo)-ferrosilite (Fs) ternary diagram with "1-kbar forbidden zone" (28) indicated by thick black line; B: Olivine forsterite (Fo)-fayalite (Fa) binary plot; C: Feldspar albite (Ab)-orthoclase (Or)-anorthite (An) ternary diagram.

### *Olivine*

Máaz PIXL scans include regions of Fe-silicate phase that are identified as fayalitic olivine ($Fo_{3-20}$; Figure 5B, Table 2) on the basis of stoichiometry (Fe:Mg:Si ratio; M site (Fe+Mg) is often underfilled). The olivine and pyroxene compositions have similar Mg:Fe ratios in the *Guillaumes*, *Bellegarde*, and *Alfalfa* scans (Table S5), consistent with the mafic minerals having formed contemporaneously at near equilibrium. In *Montpezat*, the olivines have significantly lower Mg:Fe than the pyroxenes ($Fo_{20}$ in olivine vs. Mg#=40 in the pyroxenes). The natural surface *Beaujeu* map scan contains a relatively large (0.5 mm) olivine grain that is more magnesian ($Fo_{45}$) than seen in the Máaz abraded scans and is more like those in the Séítah fm ($Fo_{43-55}$; (*41*)), likely representing a sand grain on the outcrop surface derived from one of the nearby olivine-rich lithologies.

The olivine regions are partially to entirely altered to Fe-rich serpentine minerals (±magnetite, ±silica) in all Máaz scans. Contiguous diffraction regions where corresponding X-ray spectra

share similar diffraction characteristics (i.e., peak position and intensity) indicate relict crystalline olivine grains are up to 2 mm in size (Table 3). The relatively large olivine grain size indicates they are not fine-grained breakdown products of metastable Fe-rich pyroxene ferrosilite or pyroxenoid pyroxferroite, which occurs in the mesostases of ferroan shergottite meteorites as complex or aligned intergrowths of fayalitic olivine and silica ± hedenbergite (i.e., symplectite; (*45*, *75*, *76*)) in association with other late-stage minerals (e.g., oxides and phosphates). Ferrosilite and pyroxferroite can also form at relatively high pressures, but the Máaz lavas appear undeformed, with no other textural or mineralogical evidence of high pressure conditions (*77*, *78*).

The altered olivine phase identified by PIXL in Máaz rocks makes up ~3-10 area% in scanned areas (Table 3) and may correspond to the Fe-rich, low-Ca pyroxene suggested by SuperCam LIBS (*36*). Mastcam-Z multispectral observations are consistent with the presence of low-Ca pyroxene in the Máaz fm (*35*, *60*), however they may also be consistent with ferric alteration minerals, such as are likely present in the *Alfalfa* groundmass, or in association with altered olivine. Low-Ca pyroxene has not been definitively detected by SuperCam reflectance spectroscopy in Máaz rocks (*79*). Orbital observations by CRISM (Compact Reconnaissance Imaging Spectrometer for Mars) indicate a patchy distribution of low-Ca pyroxene within the Máaz fm (*80*). The Fe-rich compositions of this phase are challenging to analyze with SHERLOC Raman because of absorption of the instruments UV radiation by ferric and ferrous iron (*42*, *61*). Discrepancies between the various instruments are likely a result of the differences in resolution and sensitivity to different minerals. For example, compared to SHERLOC, PIXL can discriminate among Fe-rich compositions, allowing individual Fe-rich silicate phases to be characterized by their elemental concentrations.

***Feldspar***

Light-toned, alumino-silicates in Máaz PIXL scans are interpreted to be alkaline plagioclase feldspar ($An_{19\text{-}38}$ $Ab_{59\text{-}71}$ $Or_{5\text{-}15}$) based on element ratios (Tables 2, S5, S7). Similar sodic feldspar compositions have been identified among the martian meteorites, including the Fe-rich shergottites (Fig. 5C) and basaltic clasts in regolith breccia NWA 7034 (*7*). Intercumulus feldspars analyzed by PIXL in the Séitah fm are more potassic than in Máaz (*41*). PIXL diffraction analysis indicates Máaz feldspars are crystalline, but total oxide abundances are generally low (77-94 total wt%), possibly reflecting the presence of incipient clay or other poorly crystalline hydrated secondary phases.

While altered plagioclase feldspar was identified in all Máaz targets analyzed by PIXL, only one plagioclase grain was identified by SuperCam LIBS ($An_{33}Ab_{28}Or_6$ within the Content member *Amignon* target; (*36*)). Numerous other high-Al SuperCam analyses are reported in Máaz that are inferred to be mixtures of plagioclase with other phases (*36*) and are consistent with the PIXL feldspar compositions. PIXL feldspar regions also appear consistent with regions inferred to be amorphous or non-olivine silicate (identified as possible feldspar) on the basis of SHERLOC Raman observations (*61*).

For most Máaz targets, modal feldspar proportions (33-41 area%; Table 3) agree reasonably well with CIPW normative plagioclase abundances (29-51 area%; Table 1). A notable exception is

*Bellegarde*, where low modal feldspar (5%) compared to its norm (34% plagioclase) is likely a product of its feldspars' fine grain size relative to the PIXL spot size.

*Alfalfa'*s distinct porphyritic texture is characterized by large plagioclase lath crystals (pl-1 and pl-2 in Fig. 2) surrounded by a fine-grained groundmass. Feldspar regions in *Alfalfa* are similar in composition (ROI bulk sum $An_{32}$ $Ab_{63}$ $Or_{05}$) to those analyzed in other Máaz rocks (Table 2). The lath crystals contain evidence for thermal resorption, including relatively large holes (~1 mm) and an embayment (>1 mm; Fig. 6A). Chemical variations within the larger plagioclase grains reveal reverse (pl-1 and pl-2) to oscillatory (pl-1) zonation with respect to Anorthite (An) content (Fig. 6B) that is not resolvable at the PIXL scale in other targets. The feldspars in Alfalfa appear enriched in Sr, which is relevant for Rb-Sr dating, but is not quantified in Table S5 due to challenges associated with its quantification (*81*). Numerous diffraction peaks in individual x-ray spectra within the feldspar regions are broadly contiguous in peak position and intensity and indicate that they make up highly ordered, single crystals. The larger lath crystals in *Alfalfa* yielded SHERLOC Raman spectra with peak centers at 1030-1110 $cm^{-1}$, consistent with crystalline plagioclase feldspar (Supplementary Materials, Fig. S11). A low-$K_2O$ rim that is up to ~0.5-mm wide and fine-grained (lesser-diffracting) surrounds the larger feldspar grains (Fig. 6A) and is interpreted to be the result of thermal and(or) chemical disequilibrium with the K-rich groundmass (Fig. 6C). Variations in CaO, FeO, and $Al_2O_3$ suggest the rim comprises a mixture of finely crystalline feldspar, augite, and Fe-silicate (Fig. 6D) that is distinct from the more homogeneous, non-diffracting KSi-rich groundmass.

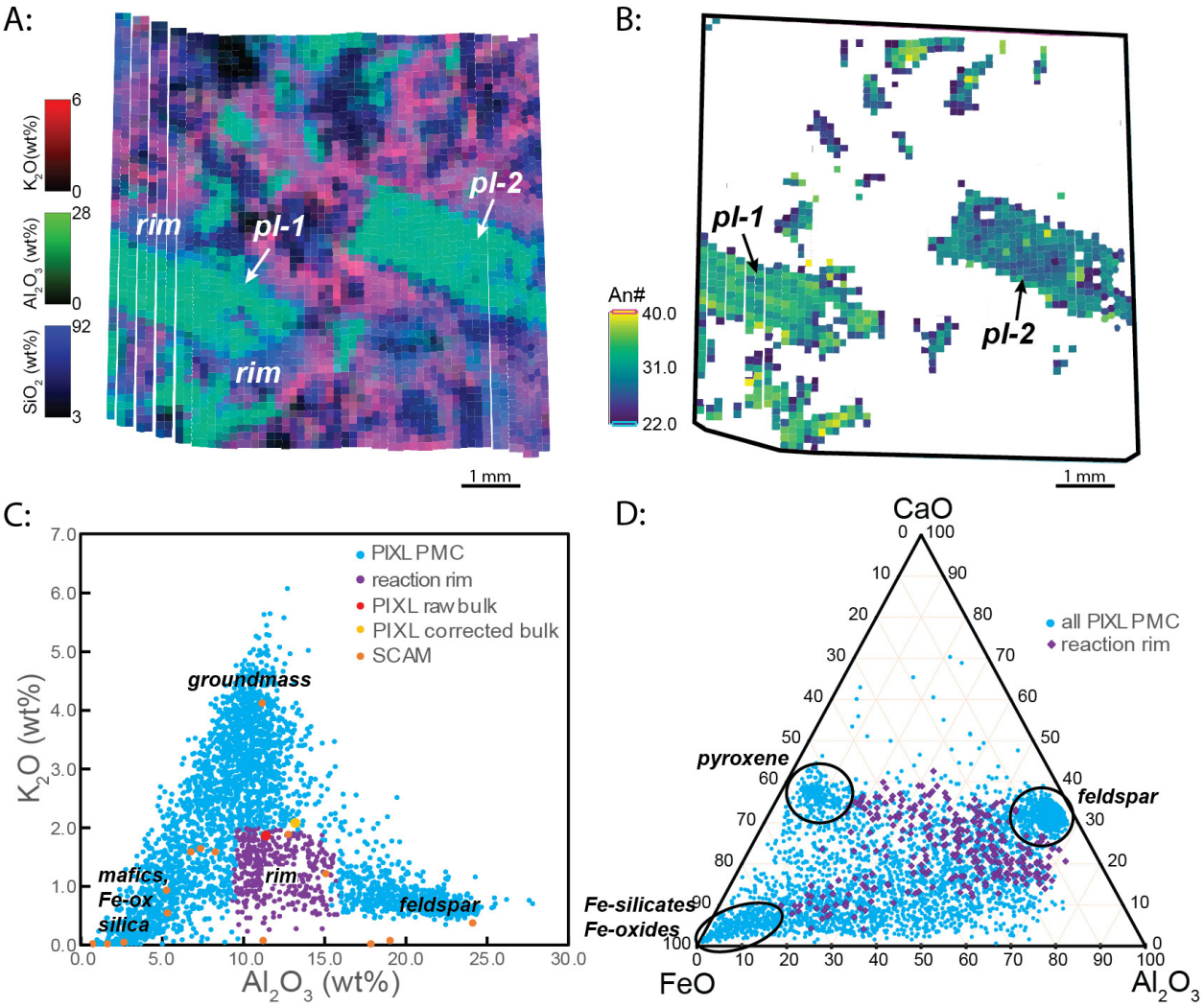


**Fig 6. *Alfalfa* PIXL maps and diagrams demonstrating feldspar textures and compositions.** A: PIXL Red-Green-Blue (RGB) maps for the *Alfalfa* abraded target, where red is $K_2O$, green is $Al_2O_3$, and blue is $SiO_2$, corrected for effects of topography and diffraction. Corroded pl-1 feldspar is partially resorbed with an embayment, indicating thermal disequilibrium. A low-K reaction rim (bluish purple) surrounds larger feldspars and is distinct from K-rich groundmass (pink). B: Map of plagioclase anorthite content (An#) determined for feldspar phenocrysts in *Alfalfa*. Both pl-1 and pl-2 display reverse zonation and pl-1 also exhibits oscillatory zonation. C: Plot of $K_2O$ vs $Al_2O_3$ presents the PIXL data as a 3-component mixture of high-Al feldspar, high-K groundmass, and low K, Al phases, including mafic minerals, Fe-oxides, and silica that are identified on the basis of PIXL XRF compositions. SCAM points are from (36). D: CaO-FeO-$Al_2O_3$ (mole%) ternary plot with endmember mineral fields and feldspar reaction rim highlighted to demonstrate that the rim is composed of a fine-grained mixture of feldspar (identified by high Al and Ca with low Fe), pyroxene (identified with high Ca and Fe with low Al), Fe-silicates, and Fe-oxides (identified with high Fe relative to Ca and Al).

***Minor and trace phases***

Oxide phases in Máaz PIXL scans occur as discrete regions with high concentrations of Fe, Ti, and/or Cr, with low Si. Their small grain size (0.3 mm) and occurrence at interstices, rather than as inclusions suggest the oxides crystallized late in the sequence and are not accumulates, although some oxide regions may include secondary oxides such as those that formed as products of olivine alteration. The oxides can be broadly separated into 3 groups based on composition: Fe-Ti-oxides including ulvöspinel and/or titanomagnetite (most common), chromite (rare), and magnetite (rare; Supplementary Materials; Fig. S12). Fe-Ti oxides occur in all Máaz targets analyzed by PIXL, often in association with other late-stage igneous phases such as Ca-phosphates (apatite and merrillite) and KSi-rich groundmass (Fig. 2D). Only one chromite was identified in Máaz, within the *Montpezat* abrasion at the interstices between altered olivine, pyroxene, and feldspar. Ti-free Fe-oxide is identified in the *Alfalfa* abrasion associated with altered Fe-silicate and is interpreted to be likely magnetite. Modal abundances of Fe-Ti-oxides are relatively high in *Guillaumes* and *Bellegarde* (18 and 33 area%, respectively, Table 3) and are likely overestimates due to the small size of the spinels (smaller than the PIXL beam size) and relative fine-grained nature of these targets.

Discrete regions with high concentrations of P and relatively low Si in Máaz PIXL scans are identified as phosphate phases. Positive correlations between P and Ca contents are indicative of Ca-phosphates with Ca:P ratios predominantly consistent with apatite and merrillite. A slight positive correlation between Cl and P in the *Bellegarde* and *Alfalfa* scans suggests magmatic Cl may have been incorporated into Cl-bearing apatites (Fig. S13). It is possible that OH and F-rich apatites in the Máaz targets are present, but these light elements are not detected by PIXL.

Zr-bearing phases are of particular interest for MSR for their potential to provide high resolution dates (*82*), but have not been definitively identified in the crater floor. PIXL scans did however yield individual analysis spots enriched in Zr distributed in the *Alfalfa* KSi-rich groundmass (Fig. S14; detection limit 1040 ppm; (*83*)) in higher numbers than observed in other crater floor rocks. The Zr-rich spots in *Alfalfa* may hint that Zr-bearing phases are present at a scale smaller than the PIXL analytical spot size for Zr excitation energy (FWHM ≈70 μm; (*84*)).

## Discussion

The PIXL instrument provides rich textural, geochemical, and mineralogical data that are critical for establishing geologic context, and for the Máaz fm, demonstrating an igneous origin and composition that is both in family with, but with significant differences from martian magmas described to date (Fig. 4, 5, S20). The interlocking pyroxene and feldspar fabric seen in basaltic *Montpezat*, *Guillaumes*, and *Bellegarde* demonstrate crystallization of these minerals at high (magmatic) temperatures. The porphyritic texture of *Alfalfa*, comprising relatively large, blocky plagioclase laths surrounded by fine-grained, K-rich groundmass, indicates a multi-stage cooling history and is most consistent with emplacement as a lava flow. The *in-situ* observations support volcanic interpretations for the Máaz fm made on the basis of orbital- and outcrop-scale observations, including lobate margins, possible vesicles, flow structures, and layering (*35*, *36*, *85*).

Moreover, the PIXL data make clear a genetic relationship; rocks within the Máaz fm share similar mineral phases and display systematic trends in both bulk elemental and mineral chemistry (Fig. 2, 4B) that suggest a shared liquid line of descent. These trends include decreasing modal pyroxene and bulk CaO and Mg# with increasing $K_2O$ contents (Fig. 2, Table 3). The following discussion examines textural and chemical evidence that differentiation of the Máaz magmas occurred in the crust. In addition, thermodynamic crystallization models demonstrate fractional crystallization is insufficient to generate the Máaz suite's very high Fe contents. We propose the Máaz magmas may have assimilated Fe-rich material located in the Mars crust to acquire their distinct Fe-rich compositions. Together, the PIXL and modeling results speak to a detailed and complex magmatic history for the Máaz fm and provide a framework for understanding samples for MSR. A genetic relationship between the Máaz lavas and Séítah olivine cumulate wehrlites is possible based on the data collected so far and may also be tested when samples are returned to Earth. Regardless of that genetic link, the Máaz compositions imply the existence of a significant reservoir of crystalline material formed as a product of intracrustal magma differentiation. Given the aerial extent of the Máaz fm in Jezero crater, this magmatic counterpart may account for a significant component of the crust within the crater region. The intracrustal magmatic processes responsible for the evolution of the Máaz magmas may be representative of the very processes that built the early martian crust and have significant implications for volatile cycling and secular evolution during the Late Noachian/Early Hesperian transition.

**Evidence for magma evolution in the crust**

Plagioclase-phyric *Alfalfa* contains the clearest mineralogical evidence that crystallization occurred in the crust. The crystallinity and relatively large size of its feldspar laths (pl-1 and pl-2) indicate they formed slowly during a period of magma storage prior. Later rapid cooling, likely during lava flow emplacement led to the formation of its fine-grained KSi-rich groundmass. The *Alfalfa* plagioclase lath compositions are like those in PIXL scans of stratigraphically lower basaltic Máaz targets (Fig. 5C) and are consistent with a genetic link between the magmas. The *Alfalfa* feldspars are not in thermal and chemical equilibrium with their surrounding magmatic environment, however; holes and an embayment in the feldspars, as well as low-K rims surrounding the crystals indicate they partially melted and reacted with the KSi-rich melt that later quenched to form the groundmass (Fig. 6A). In addition, reverse and oscillatory zonation (Fig. 6B) points to late heating of the feldspar crystals, possibly caused by mixing with basaltic magma that triggered magma ascent and eruption at the surface. While it is possible the *Alfalfa* plagioclase feldspars are relict crystals from assimilated country rock, we interpret their unbroken euhedral, albeit resorbed, lath shapes and compositional characteristics to be more consistent with an origin by crystallization of earlier generations of related magmas (i.e., antecrysts; (*86*)). Crustal-level storage and crystallization of the Alfalfa magma is also inferred by feldspar stability in martian basaltic compositions (*87*).

Highly evolved igneous rocks, such as the one represented by the *Alfalfa* scan is of high value for MSR as they typically contain late volatile (e.g., F, Cl, OH in apatite), or trace (e.g., Zr, Rb, Sr, rare earth elements) element-bearing accessory phases that would be ideal for *in-situ* micro-analysis for insight into volatile evolution, isotopic reservoirs, and geochronology. The identification of multiple geochronometers in the *Alfalfa* scan, including micro-phenocryst and antecryst plagioclase feldspar populations, K-rich groundmass, Ca-phosphates, and possible

zircons, indicates that returned samples from *Alfalfa's* outcrop Sid will help resolve the timing and evolution of its magmatic staging area as well as lava emplacement history.

Considering evidence that the *Alfalfa* magma initially staged in the crust, we infer that differentiation of other Máaz magmas likely occurred there as well. "Forbidden zone" Fe-rich augite is prevalent among the Máaz targets but is metastable at the Mars surface. The stability of Fe-rich augite increases with pressure (*28*), possibly indicating crystallization occurred at some depth. As a whole suite, evidence for fractional crystallization includes the very low and systematically decreasing bulk Mg#'s, increasing Fe contents in Fe-rich augite and olivine compositions, along with modal variations of decreasing pyroxene and increasing feldspar. Compared to other Máaz rocks, *Alfalfa* seems an outlier composition, with higher bulk $SiO_2$ and $K_2O$, lower $P_2O_5$ and $TiO_2$, as well lower modal mafic minerals (Fig. 4 and Table 3). Although it is possible *Alfalfa* experienced a separate petrogenesis, its compositional and modal aspects appear more consistent with continued high-degree fractional crystallization processes like those that led to the development of the other Máaz magmas. In particular, a KSi-rich phase, like the *Alfalfa* groundmass is identified in all Máaz targets, but is characterized as mesostasis when found in low modal abundances (e.g., as low as 3 and 6 vol% in *Guillaumes* and *Montpezat*, respectively; Table 3). This KSi-rich phase links the Máaz suite and is interpreted to be residual melt in *Montpezat* and *Guillaumes* that is increasingly concentrated in *Bellegarde* and *Alfalfa* by continued fractional crystallization of pyroxene and olivine. Variations in $P_2O_5$ and $TiO_2$ among the Máaz suite are also consistent with high degrees of crystallization. These elements increase systematically with decreasing Mg# in the basaltic targets (*Montpezat*, *Guillaumes*, and *Bellegarde*), where phosphate and Fe-Ti oxide mineral grains occur at interstices between the feldspar and pyroxene laths (Fig. 2), indicating they form as products of late-stage crystallization. In contrast, lower bulk $P_2O_5$ and $TiO_2$ concentrations in *Alfalfa* (Fig. 4B) suggest phosphate and Fe-Ti oxide minerals were removed by fractional crystallization or that its parent magma was distinct with low abundances of these elements.

**Petrological models constrain relationships between Máaz lavas**

As PIXL results indicate a significant amount of crystallization and removal of a magnesian assemblage occurred during Máaz magma petrogenesis, we conducted petrological models to better understand the amount and type of the crystallization, and the potential role of $H_2O$. These models demonstrate that the Fe and Si variations observed in the Máaz rocks point to involvement of additional components or processes during differentiation.

Among the Máaz fm outcrops analyzed, the most primitive (highest Mg#) target is *Montpezat*, *Montpezat* was analyzed at the stratigraphically lowest Artuby member near the boundary between olivine-rich Séítah and the pyroxene-rich Máaz formations at Artuby Ridge (Fig. 1). A simple and attractive hypothesis is that *Montpezat* represents the parental magma composition from which other Máaz fm targets derive. In this scenario, it is assumed that secondary aqueous alteration processes that have variably affected all Máaz rocks have not significantly changed Mg/Fe ratios in bulk or mafic mineral compositions. This assumption is supported by the observation that olivine and pyroxene have similar Mg#'s and are in apparent equilibrium in the Máaz rocks (Fig. 5).

To provide constraints on redox conditions during crystallization, we estimated the $fO_2$ (*10*) by finding at what $Fe^{3+}/Fe_{total}$ the CIPW norm calculation produces an olivine/oxide ratio that matches the modal mineralogy (Supplementary Materials; Table S8; Fig. S15). The estimated $fO_2$ for *Montpezat* at near solidus conditions is 1.90 log units below the quartz-fayalite-magnetite buffer (ΔQFM = -1.9) and is within range of other martian basaltic magmas, including the basaltic shergottites (*9*). Assuming a *Montpezat*-like parent magma, we use its estimated $fO_2$ in our models going forward. *Guillaumes* yields slightly higher $fO_2$ (ΔQFM = -1.47) and is consistent with increasing $fO_2$ (i.e., auto-oxidation) with increased differentiation. A high proportion of modal oxides and low olivine/oxide ratio in *Bellegarde* led to a significantly lower $fO_2$ estimate of ΔQFM = -3.21, which may reflect secondary or igneous processes, or an overestimate of modal oxides due to its fine-grained nature. We did not find $fO_2$ for *Alfalfa* because normative olivine is not found at any $Fe^{3+}/Fe_{total}$.

Fractional and equilibrium crystallization Perple_X models ((*88*); version 6.9.0) produce an assemblage of pyroxene, olivine, and spinel, where feldspar does not form until ~40% crystallization (Fig. 7, S16, S17). Similar trends are observed for fractional crystallization of a *Montpezat* parent by Magma Chamber Simulator (MCS; (*89*)), but with lower liquidus temperatures and deviations in melt composition at low melt fractions (Fig. S19; Supplementary Materials). Notably, these thermodynamic petrological models (Perple_X and MCS) are calibrated for terrestrial, higher Mg# compositions and may not adequately replicate crystallization of evolved Fe-rich martian basalts (*90*). In particular, these models do not predict metastable, "forbidden zone" Fe-rich augite (*28*) at low pressures, which occur as major phases in the Máaz fm and are also common among late-stage crystallization assemblages in evolved shergottitic meteorites, such as Los Angeles and Ksar Ghilane 002 (*29*, *44*, *45*).

Nevertheless, fractional and equilibrium crystallization models demonstrate that some oxide variations (CaO, $K_2O$, and MgO) are consistent with crystallization of a clinopyroxene-dominated assemblage (Fig. 7C,D, S17). Residual melts approach compositions like *Guillaumes* and *Bellegarde* in those elements at ~50 wt% crystallization (Fig. 7), and hydrous fractional crystallization models produce residual melts with near *Alfalfa*-like compositions at ~75% crystallization. The very low Mg#'s in *Bellegarde* and *Alfalfa* (13.6 and 11.2, respectively) are most consistent with models of fractional crystallization, where mineral phases are removed as soon as they form and residual melts approach Mg#=0 near the solidus. In contrast, equilibrium crystallization models, where the melt continually reacts and equilibrates with its mineral products, do not go below Mg# values of 20 (Fig. S17). This points to the accumulation of a complementary reservoir of crystalline materials during Máaz magma differentiation. Its mineral assemblage includes clinopyroxene, olivine, spinel, and feldspar at final proportions similar to the CIPW norm for *Montpezat* (Table 1; Fig. S17).

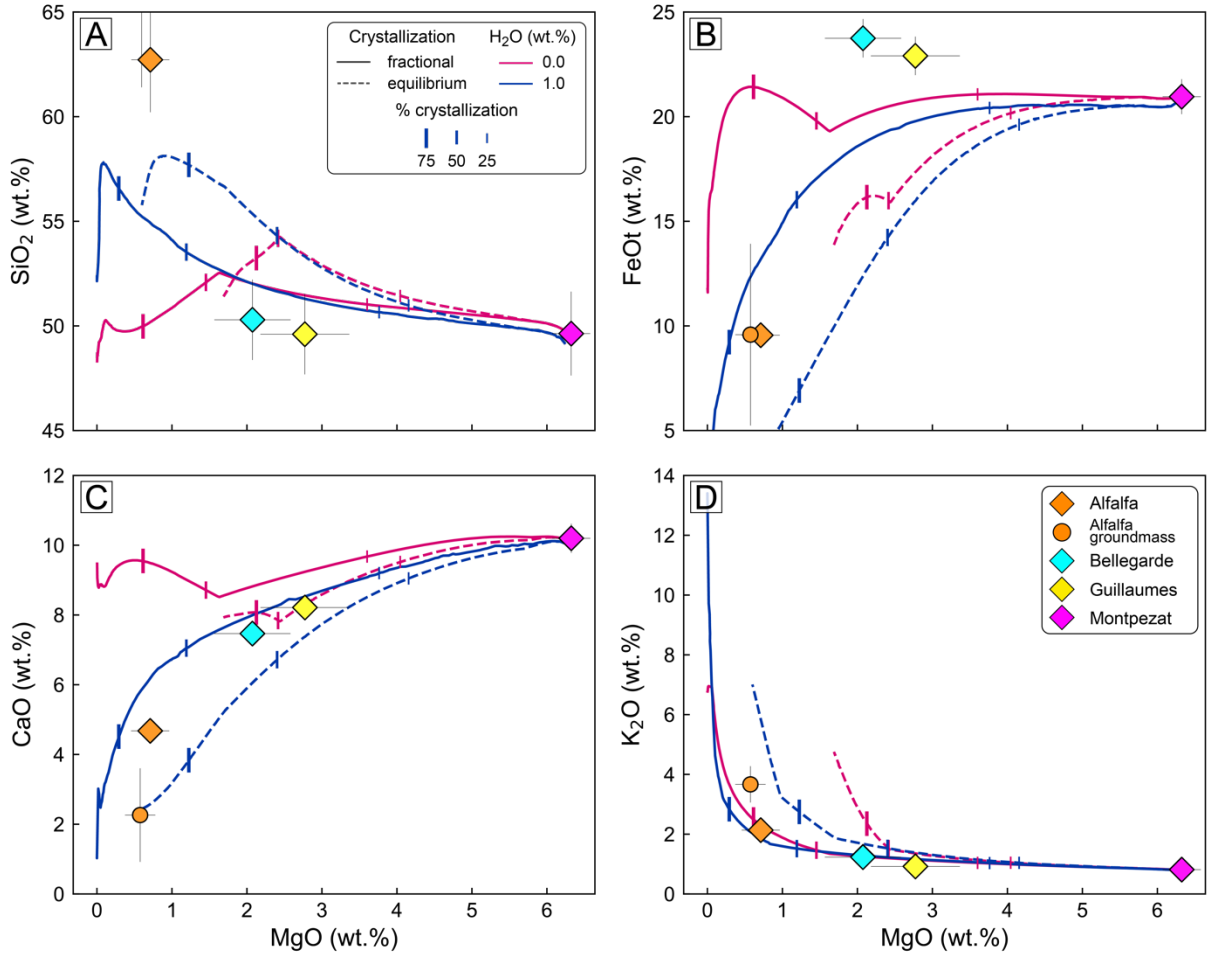


**Fig. 7. Equilibrium and fractional crystallization Perple_X models** (*88*)**; version 6.9.0) of a Montpezat parental magma at 0.1 GPa.** Calculated liquid lines of descent (LLD) and Máaz igneous compositions presented on plots of A: $SiO_2$ vs. MgO, B: FeOt vs. MgO, C: CaO vs MgO, and D: $K_2O$ vs MgO. Máaz igneous compositions are renormalized to 100% without $P_2O_5$ and MnO to be consistent with the calculated LLD since the model does not include $P_2O_5$ and MnO. See Supplementary Online Materials for modeling details.

As $H_2O$ was likely a significant volatile component in Máaz magmas, we also modeled hydrous crystallization of a starting melt with 1 wt% dissolved $H_2O$. Fe-serpentine group minerals and magnetite identified in the Máaz PIXL scans are inferred to have formed via high-temperature aqueous alteration of fayalitic olivine and are consistent with late-stage magmatic $H_2O$ being present. Cl was also likely a magmatic volatile, based on our interpretation that Cl-bearing apatite is present in some scans, but is not considered by the models. The hydrous crystallization models produce an anhydrous mineral assemblage, dominated by augite and feldspar. Hydrous minerals, such as biotite and amphibole are not produced because the calculated magma compositions have relatively low in $SiO_2$ concentrations (Fig. 7A), and determined temperatures are relatively high. Compared to the anhydrous models, the onset of feldspar crystallization is delayed by ~100˚C, allowing $SiO_2$ contents to reach higher values. The solidus is ~120-170˚C is

also lower in the hydrous runs. Final modal mineralogies are similar however, for the anhydrous and hydrous models (Fig. S17). As crystallization progresses, $H_2O$ is concentrated in the residual melt, reaching 4-5 wt% at ~75% crystallization (Fig. S18), when a separate $H_2O$ phase exsolves and the melt is most similar in composition to *Alfalfa*.

Notably, under no conditions do any of the models approach the very Fe-rich (>20 wt% FeO) and low $SiO_2$ compositions (Fig. 7A, B) observed in *Guillaumes* and *Bellegarde*. Hydrous models never produce an increase in FeO concentration relative to the parent melt. The effective liquidus phase is augite and the early predicted oxides cause the FeO content in residual melt to decrease with crystallization (Fig. S17). In contrast, the FeO content in *Alfalfa* is low compared to the other Máaz targets and its bulk and groundmass compositions are also notably enriched in $SiO_2$ compared to modeled liquid lines of descent (Fig. 7A, B). Crystallization of an Fe-oxide (magnetite or Ti-magnetite) could reduce FeO and increase $SiO_2$ in *Alfalfa*, but would require more oxidizing conditions. The significant mismatches in Fe and Si between the crystallization models and the observed Máaz compositions lead us to consider other scenarios for their petrogenesis.

**Mechanisms of variable FeO and $SiO_2$ enrichment in Máaz magmas**

Models for fractional crystallization adequately replicate many (CaO, MgO, $K_2O$), but not all (FeO and $SiO_2$) of the elemental variations observed by PIXL among the Máaz abrasion patches (Fig. 7). Differences in FeO and $SiO_2$ between the Máaz targets and the models may be because the models assume a pure melt, and do not integrate the complexity of natural magma systems, which are likely mixtures of multiple components, such as accumulated mineral phases. High bulk FeO and low $SiO_2$ in *Guillaumes* and *Bellegarde* might indicate accumulation of an Fe-oxide in the Máaz magmas, for example. However, this is not consistent with the fine grain size (Table 3) or occurrence of these minor minerals at interstices between larger pyroxene and feldspar grains (Fig. 2). Also, moderate increases in bulk $TiO_2$ (Fig. 4B) and very low $Cr_2O_3$ concentrations (Table 1) can otherwise be reconciled by fractional crystallization of Fe-rich spinels. On the other hand, anomalously high bulk $SiO_2$ concentrations in *Alfalfa* and in its groundmass compared to the fractional crystallization models do not correspond to an increase in $Al_2O_3$ (Fig. S16A) indicating that feldspar accumulation in *Alfalfa* (evidence of accumulation supported by textural evidence; Fig. 6), would not entirely account for the discrepancy in $SiO_2$. As such, mineral accumulation not captured by the models cannot completely explain the discrepancies in FeO and $SiO_2$.

Another cause of the observed differences in FeO and $SiO_2$ might be the strong dependence of petrological models on initial conditions and parent melt compositions. While *Montpezat* has a higher Mg# (35.2) and is the most primitive, it may not be representative of the Máaz parental magma and instead represent a separate evolved magma, albeit to a lesser degree. The Mg# of a primary mantle melt is constrained by its partitioning behavior with olivine, expressed as the exchange coefficient, or $KD_{ol-melt}^{Fe-Mg} = [(X_{melt}^{Mg}/X_{olivine}^{Mg})/(X_{melt}^{Fe2+}/X_{olivine}^{Fe2+})]$, and is considered constant (~0.35 for Mars magma systems; (*91*)). Although it is not possible to completely rule out an Fe-rich mantle melt on Mars, the very low Mg# and high Fe contents in Máaz would require a mantle source region enriched in distinctly Fe-rich olivine, as variations in melting parameters, such as degree, depth, or extraction rate would not significantly affect primary melt Fe/Mg ratios.

It is also possible that the rocks of the Máaz suite are products of multiple batches of magnesian parent magma(s) that evolved along separate liquid lines of descent by fractional crystallization under varying conditions, such as pressure, dissolved $H_2O$, or redox state. Even so, our models demonstrate there is a limit to how much iron a magma can attain by fractional crystallization alone because eventually, Fe-rich mafic silicate and oxide minerals start to form.

Instead, we hypothesize that assimilation of Fe-rich basement material, driven by heat carried by magmas and released during their crystallization may have contributed to the evolution of the Fe-rich Máaz magmas. Assimilation of a $SiO_2$-rich partial melt is also suggested by *Alfalfa's* bulk and groundmass high $SiO_2$ contents. Assimilation of any Fe-rich lithology has the potential to increase Fe contents, with a ~5 wt% addition of pure FeO necessary to reconcile the differences in $SiO_2$ and FeO. Adding that much Fe to a magma has strong potential to alter magmatic $fO_2$, either up or down, depending on the redox state of the materials being assimilated. Fractional crystallization of ferrous iron-bearing mafic silicates typically leads to increasing magmatic $Fe^{3+}/Fe_{total}$ ratios, which may be enhanced by assimilation of ferric iron from magnetite and(or) other Fe-oxide mineral(s). Very low estimated $fO_2$ in the *Bellegarde* target ($\Delta$QFM = -3.21) likely reflects its fine grain size leading to an over-estimation of modal FeTi-oxides as previously noted; it is also possible that *Bellegarde*'s low $fO_2$ was the result of assimilation of reduced Fe, such as from an Fe-silicate or Fe-carbonate.

Candidate Fe-rich lithologies that may be assimilated by the evolving Máaz magma system likely present in the crust beneath Jezero are varied and include products of aqueous alteration, low temperature metamorphic, and igneous processes. The region surrounding Isidis basin is variably altered and diverse alteration minerals may extend relatively deep (up to 7 km) into the Noachian basement (*92*). The widespread occurrence of Fe-rich, aqueous alteration minerals in the Isidis basin and Nili Fossae region contrasts with regional chemistry, which is not particularly rich in Fe on the basis of Gamma Ray Spectrocscopy (*93*). Breakdown of mafic silicates like olivine concentrates Fe into forms that are more reactive in the presence of high temperature magmas, such as northwest of Jezero crater, in the Nili Fossae region, where olivine-rich lithologies host phyllosilicate, carbonate, serpentine, and other low-temperature metamorphic and hydrothermal minerals (*94*, *95*).

Jezero crater-filling sediments also give insight to the sediment source region and include Fe-rich minerals (Fe-oxides, carbonates, and sulfates), some of which are interpreted to be products of alteration of an olivine-rich igneous protolith. Fe-rich products of aqueous alteration have also been identified in the Jezero crater floor, where serpentinization of olivine has produced a range of hydrated FeMg-silicates and magnetite in the Máaz fm, and FeMg-carbonate occurs along edges of olivine grains in the Séítah fm (*51*). Fe-rich carbonate is identified as a major constituent of sedimentary rocks making up the Jezero delta (*96*) and may also occur in earlier crater-filling sediments. A weathered, paleo-surface that is enriched in Fe-oxides may also be present in the Jezero basement. At greater depths in the crust, the crystalline basement may include Fe-rich ultramafic lithologies or late-stage Fe-rich (also $SiO_2$- and $K_2O$-rich) melts formed by crystallization of earlier generation magmas.

$SiO_2$-rich partial melts may also have contributed to *Alfalfa*, and could form at mid to lower crustal levels, particularly if hydrous or dehydration melting of gabbroic to ultramafic lithologies is involved (*97*). Enrichments in Si to the northeast and K/Th to the southeast of Jezero crater relative to mid-latitudinal crustal averages (*93*) may further support presence of evolved igneous melts. The amount, nature, and timing of crustal assimilation involved in Máaz petrogenesis will be tested once samples from Jezero crater and beyond are brought to Earth for detailed petrographic and isotopic studies.

**Possible link to Seitah**

The high degree of crystallization involved in the petrogenesis of Máaz magmas indicated by the PIXL results implies the existence of a complementary reservoir of accumulated crystalline material, including high-Mg lithologies that are possibly similar to the olivine cumulate rocks observed in the Séítah fm (*41*, *54*). Udry et al. (2023) propose the magmas that crystallized to form the Máaz and Séítah formations are not related to one another because olivine is not observed in Máaz by SuperCam and MELTS models of average SuperCam compositions predict a plagioclase and pyroxene-dominated crystallization assemblage that is unlike Séítah. The PIXL results however, demonstrate that variably altered olivine is present in all Máaz scans. Also, our petrological models for a *Montpezat* parental melt generated up to 17 wt% olivine (Fig. S17; Supplementary Materials). A petrogenetic link is therfore possible between a *Montpezat*-like parent melt and the olivine-rich cumulate rocks of the Séítah fm; accumulated olivines in Séítah could have potentially crystallized from the initial, *Montpezat*-like, Mg-rich melt, which later differentiated by further fractional crystallization and assimilation of Fe-rich and Si-rich materials.

Because the relative timing and nature of the contact between the Máaz and Séítah formations are unknown, the observed geology does not conclusively reveal the relationship between the two units, although it does provide additional constraints. The Máaz-Séítah contact is covered, and so its exact nature (eruptive sequence or intrusive) is not established, although it appears the highly evolved Máaz lavas formed in close proximity to coarse-grained cumulates of the Séítah formation, or vice-versa. Also, we note that intermediate magma compositions were not observed in place along the rover's traverse. Thus, a continuous magmatic lineage between the two units is not probable and may indicate intracrustal igneous processes, and(or) erosion between their respective emplacements.

**Crustal magmatism during Late Noachian to Early Hesperian**

Textural, mineralogical and bulk chemical characteristics made clear by PIXL link the Máaz magmatic suite and provide constraints for models demonstrating their petrogenesis in the Mars crust. Their petrogenesis likely involved a high degree of fractional crystallization (Fig. 7), which possibly provided heat for the assimilation of Fe-rich and Si-rich partial melts of basement lithologies. Fractional crystallization of a *Montpezat* parental melt composition produces a gabbroic assemblage of augite, olivine, spinel, and feldspar. Larger feldspar crystals in the *Alfalfa* target contain evidence of chemical or thermal disequilibria (Fig. 6) and are consistent with a period of magma storage within the crust. Because the Máaz fm is interpreted to be Late Noachian to Early Hesperian in age (*55*), these rocks may provide insight to magmatic processes during this critical period of Mars' tectonic history, when magmatism is thought to have become dominated by localized convective upwelling and plume activity (*18*).

The significance of the igneous crater floor units will come into focus as *Perseverance* continues its geologic traverse of the crater rim and beyond and new igneous and sedimentary units are encountered. It is presently unknown whether the igneous units exposed within Jezero extend beyond the crater (*39*, *80*, *98*). If Fe-rich, clinopyroxene-bearing igneous rocks are not found outside the crater, then the Máaz lavas likely represent a relatively minor episode of igneous activity localized within the crater. In which case, differentiation of Máaz magmas was restricted to small crustal-level chambers that contributed minor heterogeneities to the Mars crust. Spectral and morphological correlations however, between the Máaz fm and the Circum-Isidis mafic capping unit (*39*) and the Séítah fm and the widespread olivine-carbonate unit of Nilli Fossae (*99*), suggest similar magmatic units may well be encountered outside Jezero crater. If Máaz-like igneous rocks are identified beyond Jezero, evolved Fe-rich magmatism is important to this region of Mars; crystalline materials formed by fractional crystallization potentially contribute a volumetrically significant component of the crust and possibly represent a period of waning crustal growth driven by the migration of water-rich silicate melts during the Late Noachian/Earth Hesperian.

**The utility of PIXL**

The breadth of textural, mineralogical, and geochemical data provided by the PIXL instrument for the Máaz fm, a coherent evolved magmatic suite in Jezero crater is significant. PIXL provides a detailed first look at samples proposed to return to Earth, as well as context important for their interpretation. Return of a diverse suite of igneous rocks, including the Máaz samples, will allow a fuller picture of the Jezero magma system and allow hypotheses of relative timing and petrogenetic links between the units to be tested.

Despite considerable potential for PIXL to play an active role in geologic interpretation, it was never designed or deployed as a triage instrument (*40*, *100*). For the Jezero crater floor, evaluation of multiple working hypotheses derived from orbital observations (*55*), outcrops generally lacking well-preserved morphological features, as well as relatively late deployment of PIXL and SHERLOC on an abraded rock surface at Sol 166, significantly delayed consensus on an igneous origin, notably until well after the first core samples had been collected. The Máaz PIXL results represent a reminder that models and interpretations based on remote imaging observations are most useful after they are tested and refined by *in-situ* textural and chemical observations.

The Máaz igneous suite, including cached samples, is made significantly more valuable by having multiple PIXL analyses, which allow *in-situ* characterization of rock textures and geochemical trends that link to igneous, alteration, and geological processes. Some of these processes may constrain preservation and potential for biosignatures, an important motivator for the ambitiousness of MSR. The added value of geologic context, such as is provided by PIXL notably differentiates the Jezero samples from meteorites and exemplifies a key justification for their return. Deployment of proximity science instruments will be increasingly crucial as *Perseverance* encounters and samples new lithologies beyond Jezero crater.

## Materials and Methods

### The PIXL instrument

The Planetary Instrument for X-ray Lithochemistry (PIXL) includes a sensor assembly connected via a hexapod located on the turret at the end of the *Perseverance* rover's robotic arm (*40*). The hexapod includes actuated struts that can adjust its position, enabling movement and focusing of the sensor head. The PIXL sensor head's X-ray source generates X-rays that are focused via fiber optics to a beam of ~120 μm diameter (at 8 keV) on a target of interest. Typical duration of each spot analysis is 10 seconds, but can be extended via adaptive sampling (*101*). Autonomous navigation of the PIXL sensor head, including its initial approach, movement and focusing is enabled by imaging analysis by the optical fiducial system (OFS) that consists of the Micro Context Camera (MCC) supported by an active Floodlight Illuminator (FLI) and two Structured Light Illuminators (SLI) with built-in algorithm in its electronics (*102*, *103*). The MCC captures the textural context at ~52 μm pixel surface resolution and with a field of view covering 31 x 39 mm at nominal operating distance (*40*, *104*) and slightly lower pixel resolution and larger field of view at a higher distance from the target (*41*).

Individual X-ray spectra of a full scan or identified regions of interest (ROI) may be summed to produce a less noisy bulk spectra, yielding a bulk chemical analysis with typically lower error and lower detection limits for some trace elements. Individual point analyses (each with a unique PMC) are also considered in this study, but are more susceptible to variations in target surface topography and effects of X-ray diffraction when analyzing coarsely crystalline materials. The theory behind how we mitigate surface topography and diffraction peak overlap is presented in the Supplementary Online Materials.

### PIXLISE

PIXLISE is a data visualization software package for analyzing PIXL data, which allows viewing multiple sets of different data types for fast, interactive interpretation (*105*). Raw X-ray spectral data downlinked from Mars is quantified by PIQUANT (*81*) to generate spatial and elemental abundance data, which is parsed through the PIXLISE client. PIXLISE presents MCC microscopic multispectral imaging and scan location information alongside X-ray spectra, tables, binary and ternary plots, chord diagrams. PIXLISE fully incorporates the geometric calibration (*104*) of the flight instrument, taking into account topographic effects or underlying terrain and relative positional drift of the instrument effectuated by the large diurnal thermal environment (*106*). Regions of interest (ROI) can be identified by selecting specific scan points and/or data points in binary and ternary plots. A built-in programming language enables quantitative expressions for such purposes as correcting for elemental abundances for diffraction and topographic effects and specifying parameters for the identification of mineral endmembers.

### MCC color stack

The MCC captures a stack of four raw images, using the individual color channels of the FLI (near-infrared 735 nm, green 530 nm, blue 450 nm, ultraviolet 385 nm) enabling multispectral analysis at high spatial resolution (*107*). The raw grayscale images for the individual color channels of the FLI are radiometrically corrected based on the optical calibration and characterization of the MCC (*104*) together with in-situ measured surface topography using the SLIs. Each raw channel is individually flat-fielded and compensated for temperature driven dark

current that enables multispectral analysis at high resolution and correlation with individual XRF points (*107*) based on the four available color bands (near-infared, blue, green, ultra-violet), de-correlation stretched images, channel ratio images, and histograms/plots that help reveal underlying texture.

**Máaz PIXL analyses and context**

Details of the Maaz PIXL analyses, including scan parameters (Table S1), context images (Fig. S1, S2, S3), and outcrop and sample names (Table S2) are in the Supplementary Materials. Stratigraphic context and outcrop descriptions are also provided in the Supplementary text.

**XRF bulk sum analysis**

Bulk sum concentrations are derived from the analysis of a "bulk sum spectrum" (BSS). A BSS is produced from two or more individual spectra from one or both detectors, such as a region of interest (ROI) within a PIXL scan, defined by a common lithology and/or composition. Individual spectra to be contained within a BSS are energy corrected before inclusion. The resolution (i.e., FWHM) of a PIXL spectrum is consistent within a given activity, maintaining peak shape integrity during the generation of a BSS. The ultimate analysis of a BSS is conducted by PIQUANT (*81*), in an identical fashion to the analysis of individual PIXL spectra. The improved statistics of a BSS cf. an individual spectrum enables lower detection limits (*83*) and improved quantification, in particular for trace elements. The reported BSS concentrations are those output from PIQUANT. The reported uncertainties are a convolution of accuracy errors from PIQUANT and residuals from the spectral fit. The initial analysis does not correct for the effects of X-ray diffraction within PIXL spectra. To address X-ray diffraction within PIXL spectra for bulk analysis, the lower concentration of each oxide found for each of the two detectors is reported (Tables S3 and S4; (*108*)).

In addition to the raw bulk sums for each of the abraded Máaz targets, separate bulk analyses were determined for “low salt,” “salt-rich,” and “FeCl-rich” regions of interest (ROI) as defined in the Table S4 caption and mapped in Fig. 3. The parameters to identify these ROI are different for each scan because they contain differing amounts of salt enrichment and Fe-Cl alteration. Low salt bulk analyses are reported in Table S4 and are a weighted average (ratio of the number of PMC’s) for the low salt ROI and regions of Fe-Cl-rich alteration, where Cl was set to 1 wt%. This correction for the FeCl-rich regions is meant to be consistent with these being altered (serpentinized) olivine where Cl does not stoichiometrically correlate with other elements. Corrected igneous compositions in Table 1 were corrected for remaining Cl and $SO_3$ (subtracting $SO_3$ as $CaSO_4$ and Cl as NaCl, except for *Alfalfa* where Cl=0), and renormalized to 100%.

**Diffraction Profiles**

For mapping regions with similar diffraction patterns (Fig. 2F), eight X-ray spectral regions (each 1.5 keV wide) between 0.8-12.8 keV were checked for diffraction peaks by the same method used for diffraction peak correction. In each case, the magnitude of diffraction peaks observed in each of PIXL’s two detectors was quantified as the natural log intensity ratio to the other detector, corrected for orientation. This resulted in a diffraction peak profile expressed as a 16-vector (eight energy bins for each of two detectors) for each PMC. Diffraction pattern variations were visualized by mapping these vectors to HV (hue and value) color space. The chosen mapping codes unique combinations of peak locations to unique hues. In particular, the

location of the lowest-energy peak determines the first-order color: diffraction profiles containing lowest-energy peaks near 1 keV appear more red, those with lowest-energy peaks around 5 keV appear more green, and those with only high-energy peaks near 8 keV appear more blue. Inclusion of additional higher-energy peaks shifts the resultant color around the color wheel from blue to blue-green or from green to yellow-green. The Cartesian length of the diffraction 16-vector determines the mapped value, with 0-length vectors (no diffraction) mapped as black and spectra with increasingly intense diffraction peaks mapped as increasingly bright colors. Resultant maps enable identification of regions with similar or disparate combinations of diffraction peaks resulting from juxtapositions of monocrystalline grains of various sizes, orientations, and mineral identities.

**Grain size**

Mineral grain sizes were estimated by measuring the dimensions of 3-10 randomly selected monocrystalline representatives per map scan, depending on the abundance of each mineral. In cases where the range of observed sizes was small relative to the average size, only the mean size was reported.

**Modal analysis**

Phases considered for modal analysis include pyroxene, olivine, feldspar, Fe-Ti-Cr oxides, and K-rich groundmass. Mineral modes were determined using "Best v.3.2" expressions in PIXLISE to correct for diffraction and roughness (Supplementary Materials). PMCs representing each phase were identified using a combination of stoichiometric ratios and element thresholds (Table S7; Fig. S9). These parameters identify stoichiometrically ideal PMCs and use S and Cl thresholds to avoid the selection of scan areas that have undergone significant alteration. Expressions for identifying olivine and feldspar included Ti, Cr, and Fe (feldspar only) thresholds to avoid including grain boundaries and mixing with other phases. Parameters were varied across different scans to overcome the effects of variables such as scan area topography and XRF spectral mixing. PMCs not assigned to any of the five phases correspond mostly to stoichiometrically imperfect grain boundaries and alteration. For fine grained samples, grain boundaries and mineral interiors are harder to discern since the X-ray beam can easily excite both interior and rim. This presents a challenge for *Guillaumes* and *Bellegarde*, where grain sizes are relatively small. As such, there may be over-removal of igneous minerals at grain boundaries leading to overestimates of minor mineral modal percentages.

**Ideal mineral compositions**

The chemical compositions of the major rock forming minerals (olivine, pyroxene, and feldspar) were determined using stoichiometric ratios and element thresholds, similar to the method used for modal analysis described above. However, in order to avoid spectral mixing effects with surrounding minerals, stricter thresholds were used to identify PMCs with compositions closest to each minerals' stoichiometry (i.e., Modal Ol = $\frac{Fe + Mg}{Si} = 2 \pm 1$ mol, Ideal Ol = $\frac{Fe + Mg}{Si} = 2 \pm 0.4$ mol; Table S7). The olivine, pyroxene, and feldspar compositions for each scan (Table S5) are average compositions of these stoichiometrically ideal PMC's. In order to account for secondary alteration, only PMCs with low S and Cl were included in the averages. Any remaining S and Cl in the average compositions was then stoichiometrically "stripped" using the same corrections as the low salt bulk sums (subtracting $SO_3$ as $CaSO_4$ and Cl=0 for all scans, except for *Guillaumes* where Cl was subtracted as NaCl).

## References


1. M. Wilson, Magmatic differentiation. *JGS* **150**, 611–624 (1993).

2. A. L. Grunder, Material and thermal roles of basalt in crustal magmatism: Case study from eastern Nevada. *Geol* **23**, 952 (1995).

3. S. M. White, J. A. Crisp, F. J. Spera, Long-term volumetric eruption rates and magma budgets. *Geochem Geophys Geosyst* **7**, 2005GC001002 (2006).

4. A. Udry, E. Gazel, H. Y. McSween, Formation of Evolved Rocks at Gale Crater by Crystal Fractionation and Implications for Mars Crustal Composition. *JGR Planets* **123**, 1525–1540 (2018).

5. A. Cousin, V. Sautter, V. Payré, O. Forni, N. Mangold, O. Gasnault, L. Le Deit, J. Johnson, S. Maurice, M. Salvatore, R. C. Wiens, P. Gasda, W. Rapin, Classification of igneous rocks analyzed by ChemCam at Gale crater, Mars. *Icarus* **288**, 265–283 (2017).

6. A. D. Rogers, H. Nekvasil, Feldspathic rocks on Mars: Compositional constraints from infrared spectroscopy and possible formation mechanisms. *Geophysical Research Letters* **42**, 2619–2626 (2015).

7. A. R. Santos, C. B. Agee, F. M. McCubbin, C. K. Shearer, P. V. Burger, R. Tartèse, M. Anand, Petrology of igneous clasts in Northwest Africa 7034: Implications for the petrologic diversity of the martian crust. *Geochimica et Cosmochimica Acta* **157**, 56–85 (2015).

8. S. R. Taylor, S. M. McLennan, *Planetary Crusts: Their Composition, Origin and Evolution* (Cambridge University Press, Cambridge, UK ; New York, 2009)*Cambridge planetary science*.

9. C. D. K. Herd, L. E. Borg, J. H. Jones, J. J. Papike, Oxygen fugacity and geochemical variations in the martian basalts: implications for martian basalt petrogenesis and the oxidation state of the upper mantle of Mars. *Geochimica et Cosmochimica Acta* **66**, 2025–2036 (2002).

10. M. E. Schmidt, C. M. Schrader, T. J. McCoy, The primary fO2 of basalts examined by the Spirit rover in Gusev Crater, Mars: Evidence for multiple redox states in the martian interior. *Earth and Planetary Science Letters* **384**, 198–208 (2013).

11. F. M. McCubbin, J. W. Boyce, P. Srinivasan, A. R. Santos, S. M. Elardo, J. Filiberto, A. Steele, C. K. Shearer, Heterogeneous distribution of $H_2O$ in the Martian interior: Implications for the abundance of $H_2O$ in depleted and enriched mantle sources. *Meteorit & Planetary Scien* **51**, 2036–2060 (2016).

12. D. Baratoux, H. Samuel, C. Michaut, M. J. Toplis, M. Monnereau, M. Wieczorek, R. Garcia, K. Kurita, Petrological constraints on the density of the Martian crust. *J. Geophys. Res. Planets* **119**, 1707–1727 (2014).

13. H. Y. McSween, G. J. Taylor, M. B. Wyatt, Elemental Composition of the Martian Crust. *Science* **324**, 736–739 (2009).

14. W. B. Moore, J. I. Simon, A. A. G. Webb, Heat-pipe planets. *Earth and Planetary Science Letters* **474**, 13–19 (2017).

15. S. A. Hauck, R. J. Phillips, Thermal and crustal evolution of Mars. *J. Geophys. Res.* **107** (2002).

16. M. Grott, A. Morschhauser, D. Breuer, E. Hauber, Volcanic outgassing of CO2 and H2O on Mars. *Earth and Planetary Science Letters* **308**, 391–400 (2011).

17. A. A. Fraeman, J. Korenaga, The influence of mantle melting on the evolution of Mars. *Icarus* **210**, 43–57 (2010).

18. A. Morschhauser, M. Grott, D. Breuer, Crustal recycling, mantle dehydration, and the thermal evolution of Mars. *Icarus* **212**, 541–558 (2011).

19. A. D. Rogers, V. E. Hamilton, Compositional provinces of Mars from statistical analyses of TES, GRS, OMEGA and CRISM data. *JGR Planets* **120**, 62–91 (2015).

20. J. M. D. Day, M. Paquet, A. Udry, F. Moynier, A heterogeneous mantle and crustal structure formed during the early differentiation of Mars. *Sci. Adv.* **10**, eadn9830 (2024).

21. D. Baratoux, M. J. Toplis, M. Monnereau, O. Gasnault, Thermal history of Mars inferred from orbital geochemistry of volcanic provinces. *Nature* **472**, 338–341 (2011).

22. T. Usui, C. M. O. Alexander, J. Wang, J. I. Simon, J. H. Jones, Origin of water and mantle–crust interactions on Mars inferred from hydrogen isotopes and volatile element abundances of olivine-hosted melt inclusions of primitive shergottites. *Earth and Planetary Science Letters* **357–358**, 119–129 (2012).

23. J. Ferdous, A. D. Brandon, A. H. Peslier, Z. Pirotte, Evaluating crustal contributions to enriched shergottites from the petrology, trace elements, and Rb-Sr and Sm-Nd isotope systematics of Northwest Africa 856. *Geochimica et Cosmochimica Acta* **211**, 280–306 (2017).

24. S. J. K. Symes, L. E. Borg, C. K. Shearer, A. J. Irving, The age of the martian meteorite Northwest Africa 1195 and the differentiation history of the shergottites. *Geochimica et Cosmochimica Acta* **72**, 1696–1710 (2008).

25. L. E. Borg, L. E. Nyquist, L. A. Taylor, H. Wiesmann, C.-Y. Shih, Constraints on Martian differentiation processes from Rb□Sr and Sm□Nd isotopic analyses of the basaltic shergottite QUE 94201. *Geochimica et Cosmochimica Acta* **61**, 4915–4931 (1997).

26. T. J. Peters, J. I. Simon, J. H. Jones, T. Usui, R. Moriwaki, R. C. Economos, A. K. Schmitt, K. D. McKeegan, Tracking the source of the enriched martian meteorites in

olivine-hosted melt inclusions of two depleted shergottites, Yamato 980459 and Tissint. *Earth and Planetary Science Letters* **418**, 91–102 (2015).

27. A. E. Rubin, P. H. Warren, J. P. Greenwood, R. S. Verish, L. A. Leshin, R. L. Hervig, R. N. Clayton, T. K. Mayeda, Los Angeles: The most differentiated basaltic martian meteorite. *Geology* **28**, 1011–1014 (2000).

28. D. H. Lindsley, Pyroxene thermometry. *American Mineralogist* **68**, 477–493 (1983).

29. A. I. Sheen, C. D. K. Herd, J. Hamilton, E. L. Walton, C. Goodrich, Petrographic controls on baddeleyite occurrence in a suite of eight basaltic shergottites. *Meteorit Planet Sci* **56**, 1502–1530 (2021).

30. L. Nyquist, D. Bogard, C.-Y. Shih, A. Greshake, D. Stöffler, O. Eugster, "Ages and geologic histories of Martian meteorites" (Springer, 2001), pp. 105–164.

31. T. J. Lapen, M. Righter, A. D. Brandon, V. Debaille, B. L. Beard, J. T. Shafer, A. H. Peslier, A Younger Age for ALH84001 and Its Geochemical Link to Shergottite Sources in Mars. *Science* **328**, 347–351 (2010).

32. F. M. McCubbin, J. W. Boyce, T. Novák-Szabó, A. R. Santos, R. Tartèse, N. Muttik, G. Domokos, J. Vazquez, L. P. Keller, D. E. Moser, D. J. Jerolmack, C. K. Shearer, A. Steele, S. M. Elardo, Z. Rahman, M. Anand, T. Delhaye, C. B. Agee, Geologic history of Martian regolith breccia Northwest Africa 7034: Evidence for hydrothermal activity and lithologic diversity in the Martian crust. *JGR Planets* **121**, 2120–2149 (2016).

33. K. A. Farley, K. M. Stack, D. L. Shuster, B. H. N. Horgan, J. A. Hurowitz, J. D. Tarnas, J. I. Simon, V. Z. Sun, E. L. Scheller, K. R. Moore, S. M. McLennan, P. M. Vasconcelos, R. C. Wiens, A. H. Treiman, L. E. Mayhew, O. Beyssac, T. V. Kizovski, N. J. Tosca, K. H. Williford, L. S. Crumpler, L. W. Beegle, J. F. Bell, B. L. Ehlmann, Y. Liu, J. N. Maki, M. E. Schmidt, A. C. Allwood, H. E. F. Amundsen, R. Bhartia, T. Bosak, A. J. Brown, B. C. Clark, A. Cousin, O. Forni, T. S. J. Gabriel, Y. Goreva, S. Gupta, S.-E. Hamran, C. D. K. Herd, K. Hickman-Lewis, J. R. Johnson, L. C. Kah, P. B. Kelemen, K. B. Kinch, L. Mandon, N. Mangold, C. Quantin-Nataf, M. S. Rice, P. S. Russell, S. Sharma, S. Siljeström, A. Steele, R. Sullivan, M. Wadhwa, B. P. Weiss, A. J. Williams, B. V. Wogsland, P. A. Willis, T. A. Acosta-Maeda, P. Beck, K. Benzerara, S. Bernard, A. S. Burton, E. L. Cardarelli, B. Chide, E. Clavé, E. A. Cloutis, B. A. Cohen, A. D. Czaja, V. Debaille, E. Dehouck, A. G. Fairén, D. T. Flannery, S. Z. Fleron, T. Fouchet, J. Frydenvang, B. J. Garczynski, E. F. Gibbons, E. M. Hausrath, A. G. Hayes, J. Henneke, J. L. Jørgensen, E. M. Kelly, J. Lasue, S. Le Mouélic, J. M. Madariaga, S. Maurice, M. Merusi, P.-Y. Meslin, S. M. Milkovich, C. C. Million, R. C. Moeller, J. I. Núñez, A. M. Ollila, G. Paar, D. A. Paige, D. A. K. Pedersen, P. Pilleri, C. Pilorget, P. C. Pinet, J. W. Rice, C. Royer, V. Sautter, M. Schulte, M. A. Sephton, S. K. Sharma, S. F. Sholes, N. Spanovich, M. St. Clair, C. D. Tate, K. Uckert, S. J. VanBommel, A. G. Yanchilina, M.-P. Zorzano, Aqueously altered igneous rocks sampled on the floor of Jezero crater, Mars. *Science* **377**, eabo2196 (2022).

34. E. L. Scheller, B. L. Ehlmann, Composition, Stratigraphy, and Geological History of the Noachian Basement Surrounding the Isidis Impact Basin. *JGR Planets* **125**, e2019JE006190 (2020).

35. B. Horgan, A. Udry, M. Rice, S. Alwmark, H. E. F. Amundsen, J. F. Bell, L. Crumpler, B. Garczynski, J. Johnson, K. Kinch, L. Mandon, M. Merusi, C. Million, J. I. Núñez, P. Russell, J. I. Simon, M. St. Clair, K. M. Stack, A. Vaughan, B. Wogsland, A. Annex, A. Bechtold, T. Berger, O. Beyssac, A. Brown, E. Cloutis, B. A. Cohen, S. Fagents, L. Kah, K. Farley, D. Flannery, S. Gupta, S. Hamran, Y. Liu, G. Paar, C. Quantin-Nataf, N. Randazzo, E. Ravanis, S. Sholes, D. Shuster, V. Sun, C. Tate, N. Tosca, M. Wadhwa, R. C. Wiens, Mineralogy, Morphology, and Emplacement History of the Maaz Formation on the Jezero Crater Floor From Orbital and Rover Observations. *JGR Planets* **128**, e2022JE007612 (2023).

36. A. Udry, A. Ostwald, V. Sautter, A. Cousin, O. Beyssac, O. Forni, G. Dromart, K. Benzerara, M. Nachon, B. Horgan, L. Mandon, E. Clavé, E. Dehouck, E. Gibbons, S. Alwmark, E. Ravanis, R. C. Wiens, C. Legett, R. Anderson, P. Pilleri, N. Mangold, M. Schmidt, Y. Liu, J. I. Núñez, K. Castro, J. M. Madariaga, T. Kizovski, P. Beck, S. Bernard, T. Bosak, A. Brown, S. Clegg, E. Cloutis, B. Cohen, S. Connell, L. Crumpler, V. Debaille, D. Flannery, T. Fouchet, T. S. J. Gabriel, O. Gasnault, C. D. K. Herd, J. Johnson, J. A. Manrique, S. Maurice, F. M. McCubbin, S. McLennan, A. Ollila, P. Pinet, C. Quantin-Nataf, C. Royer, S. Sharma, J. I. Simon, A. Steele, N. Tosca, A. Treiman, the SuperCam team, A Mars 2020 *Perseverance* SuperCam Perspective on the Igneous Nature of the Máaz Formation at Jezero Crater and Link With Séítah, Mars. *JGR Planets* **128**, e2022JE007440 (2023).

37. L. Rubanenko, T. M. Powell, J.-P. Williams, I. Daubar, K. S. Edgett, D. A. Paige, "Challenges in crater chronology on Mars as reflected in Jezero crater" in *Mars Geological Enigmas* (Elsevier, 2021; https://linkinghub.elsevier.com/retrieve/pii/B9780128202456000057), pp. 97–122.

38. C. Quantin-Nataf, S. Alwmark, F. J. Calef, J. Lasue, K. Kinch, K. M. Stack, V. Sun, N. R. Williams, E. Dehouck, L. Mandon, N. Mangold, O. Beyssac, E. Clave, S. H. G. Walter, J. I. Simon, A. M. Annex, B. Horgan, J. W. Rice, D. Shuster, B. Cohen, L. Kah, S. Sholes, B. P. Weiss, The Complex Exhumation History of Jezero Crater Floor Unit and Its Implication for Mars Sample Return. *JGR Planets* **128**, e2022JE007628 (2023).

39. C. B. Hundal, J. F. Mustard, C. H. Kremer, J. D. Tarnas, A. C. Pascuzzo, The Circum-Isidis Capping Unit: An Extensive Regional Ashfall Deposit Exposed in Jezero Crater. *Geophysical Research Letters* **49**, e2021GL096920 (2022).

40. A. C. Allwood, L. A. Wade, M. C. Foote, W. T. Elam, J. A. Hurowitz, S. Battel, D. E. Dawson, R. W. Denise, E. M. Ek, M. S. Gilbert, M. E. King, C. C. Liebe, T. Parker, D. A. K. Pedersen, D. P. Randall, R. F. Sharrow, M. E. Sondheim, G. Allen, K. Arnett, M. H. Au, C. Basset, M. Benn, J. C. Bousman, D. Braun, R. J. Calvet, B. Clark, L. Cinquini, S. Conaby, H. A. Conley, S. Davidoff, J. Delaney, T. Denver, E. Diaz, G. B. Doran, J. Ervin, M. Evans, D. O. Flannery, N. Gao, J. Gross, J. Grotzinger, B. Hannah, J. T. Harris, C. M.

Harris, Y. He, C. M. Heirwegh, C. Hernandez, E. Hertzberg, R. P. Hodyss, J. R. Holden, C. Hummel, M. A. Jadusingh, J. L. Jørgensen, J. H. Kawamura, A. Kitiyakara, K. Kozaczek, J. L. Lambert, P. R. Lawson, Y. Liu, T. S. Luchik, K. M. Macneal, S. N. Madsen, S. M. McLennan, P. McNally, P. L. Meras, R. E. Muller, J. Napoli, B. J. Naylor, P. Nemere, I. Ponomarev, R. M. Perez, N. Pootrakul, R. A. Romero, R. Rosas, J. Sachs, R. T. Schaefer, M. E. Schein, T. P. Setterfield, V. Singh, E. Song, M. M. Soria, P. C. Stek, N. R. Tallarida, D. R. Thompson, M. M. Tice, L. Timmermann, V. Torossian, A. Treiman, S. Tsai, K. Uckert, J. Villalvazo, M. Wang, D. W. Wilson, S. C. Worel, P. Zamani, M. Zappe, F. Zhong, R. Zimmerman, PIXL: Planetary Instrument for X-Ray Lithochemistry. *Space Sci Rev* **216**, 134 (2020).

41. Y. Liu, M. M. Tice, M. E. Schmidt, A. H. Treiman, T. V. Kizovski, J. A. Hurowitz, A. C. Allwood, J. Henneke, D. A. K. Pedersen, S. J. VanBommel, M. W. M. Jones, A. L. Knight, B. J. Orenstein, B. C. Clark, W. T. Elam, C. M. Heirwegh, T. Barber, L. W. Beegle, K. Benzerara, S. Bernard, O. Beyssac, T. Bosak, A. J. Brown, E. L. Cardarelli, D. C. Catling, J. R. Christian, E. A. Cloutis, B. A. Cohen, S. Davidoff, A. G. Fairén, K. A. Farley, D. T. Flannery, A. Galvin, J. P. Grotzinger, S. Gupta, J. Hall, C. D. K. Herd, K. Hickman-Lewis, R. P. Hodyss, B. H. N. Horgan, J. R. Johnson, J. L. Jørgensen, L. C. Kah, J. N. Maki, L. Mandon, N. Mangold, F. M. McCubbin, S. M. McLennan, K. Moore, M. Nachon, P. Nemere, L. D. Nothdurft, J. I. Núñez, L. O'Neil, C. M. Quantin-Nataf, V. Sautter, D. L. Shuster, K. L. Siebach, J. I. Simon, K. P. Sinclair, K. M. Stack, A. Steele, J. D. Tarnas, N. J. Tosca, K. Uckert, A. Udry, L. A. Wade, B. P. Weiss, R. C. Wiens, K. H. Williford, M.-P. Zorzano, An olivine cumulate outcrop on the floor of Jezero crater, Mars. *Science* **377**, 1513–1519 (2022).

42. R. Bhartia, L. W. Beegle, L. DeFlores, W. Abbey, J. Razzell Hollis, K. Uckert, B. Monacelli, K. S. Edgett, M. R. Kennedy, M. Sylvia, Perseverance's scanning habitable environments with Raman and luminescence for organics and chemicals (SHERLOC) investigation. *Space Science Reviews* **217**, 58 (2021).

43. J. Llorca, J. Roszjar, J. A. Cartwright, A. Bischoff, U. Ott, A. Pack, S. Merchel, G. Rugel, L. Fimiani, P. Ludwig, J. V. Casado, D. Allepuz, The Ksar Ghilane 002 shergottite-The 100th registered Martian meteorite fragment. *Meteorit Planet Sci* **48**, 493–513 (2013).

44. T. Mikouchi, Mineralogical similarities and differences between the Los Angeles basaltic shergottite and the Asuka-881757 lunar mare meteorite. *Antarctic Meteorite Research* **14**, 1 (2001).

45. P. H. Warren, J. P. Greenwood, A. E. Rubin, Los Angeles: A tale of two stones. *Meteoritics & Planetary Science* **39**, 137–156 (2004).

46. E. L. Scheller, J. Razzell Hollis, E. L. Cardarelli, A. Steele, L. W. Beegle, R. Bhartia, P. Conrad, K. Uckert, S. Sharma, B. L. Ehlmann, W. J. Abbey, S. A. Asher, K. C. Benison, E. L. Berger, O. Beyssac, B. L. Bleefeld, T. Bosak, A. J. Brown, A. S. Burton, S. V. Bykov, E. Cloutis, A. G. Fairén, L. DeFlores, K. A. Farley, D. M. Fey, T. Fornaro, A. C. Fox, M. Fries, K. Hickman-Lewis, W. F. Hug, J. E. Huggett, S. Imbeah, R. S. Jakubek, L. C. Kah, P. Kelemen, M. R. Kennedy, T. Kizovski, C. Lee, Y. Liu, L. Mandon, F. M.

McCubbin, K. R. Moore, B. E. Nixon, J. I. Núñez, C. Rodriguez Sanchez-Vahamonde, R. D. Roppel, M. Schulte, M. A. Sephton, S. K. Sharma, S. Siljeström, S. Shkolyar, D. L. Shuster, J. I. Simon, R. J. Smith, K. M. Stack, K. Steadman, B. P. Weiss, A. Werynski, A. J. Williams, R. C. Wiens, K. H. Williford, K. Winchell, B. Wogsland, A. Yanchilina, R. Yingling, M.-P. Zorzano, Aqueous alteration processes in Jezero crater, Mars—implications for organic geochemistry. *Science* **378**, 1105–1110 (2022).

47. S. Sharma, R. D. Roppel, A. E. Murphy, L. W. Beegle, R. Bhartia, A. Steele, J. R. Hollis, S. Siljeström, F. M. McCubbin, S. A. Asher, W. J. Abbey, A. C. Allwood, E. L. Berger, B. L. Bleefeld, A. S. Burton, S. V. Bykov, E. L. Cardarelli, P. G. Conrad, A. Corpolongo, A. D. Czaja, L. P. DeFlores, K. Edgett, K. A. Farley, T. Fornaro, A. C. Fox, M. D. Fries, D. Harker, K. Hickman-Lewis, J. Huggett, S. Imbeah, R. S. Jakubek, L. C. Kah, C. Lee, Y. Liu, A. Magee, M. Minitti, K. R. Moore, A. Pascuzzo, C. Rodriguez Sanchez-Vahamonde, E. L. Scheller, S. Shkolyar, K. M. Stack, K. Steadman, M. Tuite, K. Uckert, A. Werynski, R. C. Wiens, A. J. Williams, K. Winchell, M. R. Kennedy, A. Yanchilina, Diverse organic-mineral associations in Jezero crater, Mars. *Nature* **619**, 724–732 (2023).

48. T. Haltigin, E. Hauber, G. Kminek, M. A. Meyer, C. B. Agee, H. Busemann, B. L. Carrier, D. P. Glavin, L. E. Hays, B. Marty, L. M. Pratt, A. Udry, M.-P. Zorzano, D. W. Beaty, B. Cavalazzi, C. S. Cockell, V. Debaille, M. M. Grady, A. Hutzler, F. M. McCubbin, A. B. Regberg, A. L. Smith, C. L. Smith, R. E. Summons, T. D. Swindle, K. T. Tait, N. J. Tosca, T. Usui, M. A. Velbel, M. Wadhwa, F. Westall, Rationale and Proposed Design for a Mars Sample Return (MSR) Science Program. *Astrobiology* **22**, S-27-S-56 (2022).

49. J. I. Simon, K. Hickman-Lewis, B. A. Cohen, L. E. Mayhew, D. L. Shuster, V. Debaille, E. M. Hausrath, B. P. Weiss, T. Bosak, M. -P. Zorzano, H. E. F. Amundsen, L. W. Beegle, J. F. Bell, K. C. Benison, E. L. Berger, O. Beyssac, A. J. Brown, F. Calef, T. M. Casademont, B. Clark, E. Clavé, L. Crumpler, A. D. Czaja, A. G. Fairén, K. A. Farley, D. T. Flannery, T. Fornaro, O. Forni, F. Gómez, Y. Goreva, A. Gorin, K. P. Hand, S. -E. Hamran, J. Henneke, C. D. K. Herd, B. H. N. Horgan, J. R. Johnson, J. Joseph, R. E. Kronyak, J. M. Madariaga, J. N. Maki, L. Mandon, F. M. McCubbin, S. M. McLennan, R. C. Moeller, C. E. Newman, J. I. Núñez, A. C. Pascuzzo, D. A. Pedersen, G. Poggiali, P. Pinet, C. Quantin-Nataf, M. Rice, J. W. Rice, C. Royer, M. Schmidt, M. Sephton, S. Sharma, S. Siljeström, K. M. Stack, A. Steele, V. Z. Sun, A. Udry, S. VanBommel, M. Wadhwa, R. C. Wiens, A. J. Williams, K. H. Williford, Samples Collected From the Floor of Jezero Crater With the Mars 2020 Perseverance Rover. *JGR Planets* **128**, e2022JE007474 (2023).

50. E. Clavé, K. Benzerara, P. -Y. Meslin, O. Forni, C. Royer, L. Mandon, P. Beck, C. Quantin-Nataf, O. Beyssac, A. Cousin, B. Bousquet, R. C. Wiens, S. Maurice, E. Dehouck, S. Schröder, O. Gasnault, N. Mangold, G. Dromart, T. Bosak, S. Bernard, A. Udry, R. B. Anderson, G. Arana, A. J. Brown, K. Castro, S. M. Clegg, E. Cloutis, A. G. Fairén, D. T. Flannery, P. J. Gasda, J. R. Johnson, J. Lasue, G. Lopez-Reyes, J. M. Madariaga, J. A. Manrique, S. Le Mouélic, J. I. Núñez, A. M. Ollila, P. Pilleri, C. Pilorget, P. Pinet, F. Poulet, M. Veneranda, Z. U. Wolf, the SuperCam team, Carbonate Detection With SuperCam in Igneous Rocks on the Floor of Jezero Crater, Mars. *JGR Planets* **128**, e2022JE007463 (2023).

51. M. M. Tice, J. A. Hurowitz, A. C. Allwood, M. W. M. Jones, B. J. Orenstein, S. Davidoff, A. P. Wright, D. A. K. Pedersen, J. Henneke, N. J. Tosca, K. R. Moore, B. C. Clark, S. M. McLennan, D. T. Flannery, A. Steele, A. J. Brown, M.-P. Zorzano, K. Hickman-Lewis, Y. Liu, S. J. VanBommel, M. E. Schmidt, T. V. Kizovski, A. H. Treiman, L. O'Neil, A. G. Fairén, D. L. Shuster, S. Gupta, The PIXL Team, Alteration history of Séítah formation rocks inferred by PIXL x-ray fluorescence, x-ray diffraction, and multispectral imaging on Mars. *Sci. Adv.* **8**, eabp9084 (2022).

52. B. J. Orenstein, D. T. Flannery, L. W. Casey, W. T. Elam, C. M. Heirwegh, M. W. M. Jones, A statistical approach to removing diffraction from X-ray fluorescence spectra. *Spectrochimica Acta Part B: Atomic Spectroscopy* **200**, 106603 (2023).

53. L. S. Crumpler, B. Horgan, J. Simon, K. Stack, S. Alwmark, D. Gilles, R. Wiens, A. Udry, A. Brown, P. Russell, H. Amundson, S. Hamran, J. Bell, D. Shuster, F. Calef, J. Núñez, B. Cohen, D. Flannery, C. D. K. Herd, K. Hand, J. Maki, M. Schmidt, M. Golombek, N. Williams, In Situ Geologic Context Mapping Transect on the Floor of Jezero Crater from Mars 2020 Perseverance Rover Observations. *JGR Planets*, e2022JE007444 (2023).

54. O. Beyssac, O. Forni, A. Cousin, A. Udry, L. C. Kah, L. Mandon, O. E. Clavé, Y. Liu, F. Poulet, C. Quantin Nataf, O. Gasnault, J. R. Johnson, K. Benzerara, P. Beck, E. Dehouck, N. Mangold, C. Alvarez Llamas, R. B. Anderson, G. Arana, R. Barnes, S. Bernard, T. Bosak, A. J. Brown, K. Castro, B. Chide, S. M. Clegg, E. Cloutis, T. Fouchet, T. Gabriel, S. Gupta, G. Lacombe, J. Lasue, S. Le Mouelic, G. Lopez-Reyes, J. M. Madariaga, F. M. McCubbin, S. M. McLennan, J. A. Manrique, P. Y. Meslin, F. Montmessin, J. Núñez, A. M. Ollila, A. Ostwald, P. Pilleri, P. Pinet, C. Royer, S. K. Sharma, S. Schröder, J. I. Simon, M. J. Toplis, M. Veneranda, P. A. Willis, S. Maurice, R. C. Wiens, The SuperCam Team, Petrological Traverse of the Olivine Cumulate Séítah Formation at Jezero Crater, Mars: A Perspective From SuperCam Onboard Perseverance. *JGR Planets* **128**, e2022JE007638 (2023).

55. V. Z. Sun, K. M. Stack, "Geologic map of Jezero crater and the Nili Planum region, Mars" (U.S. Geological Survey Scientific Investigations Map Scientific Investigations Map, 2020); https://pubs.usgs.gov/sim/3464/sim3464_pamphlet.pdf.

56. N. Mangold, S. Gupta, O. Gasnault, G. Dromart, J. D. Tarnas, S. F. Sholes, B. Horgan, C. Quantin-Nataf, A. J. Brown, S. Le Mouélic, R. A. Yingst, J. F. Bell, O. Beyssac, T. Bosak, F. Calef, B. L. Ehlmann, K. A. Farley, J. P. Grotzinger, K. Hickman-Lewis, S. Holm-Alwmark, L. C. Kah, J. Martinez-Frias, S. M. McLennan, S. Maurice, J. I. Nuñez, A. M. Ollila, P. Pilleri, J. W. Rice, M. Rice, J. I. Simon, D. L. Shuster, K. M. Stack, V. Z. Sun, A. H. Treiman, B. P. Weiss, R. C. Wiens, A. J. Williams, N. R. Williams, K. H. Williford, Perseverance rover reveals an ancient delta-lake system and flood deposits at Jezero crater, Mars. *Science* **374**, 711–717 (2021).

57. D. A. Paige, S.-E. Hamran, H. E. F. Amundsen, T. Berger, P. Russell, R. Kakaria, M. T. Mellon, S. Eide, L. M. Carter, T. M. Casademont, D. C. Nunes, E. S. Shoemaker, D. Plettemeier, H. Dypvik, S. Holm-Alwmark, B. H. N. Horgan, Ground penetrating radar

observations of the contact between the western delta and the crater floor of Jezero crater, Mars. *Sci. Adv.* **10**, eadi8339 (2024).

58. S. Alwmark, B. Horgan, A. Udry, A. Bechtold, S. Fagents, E. Ravanis, L. Crumpler, N. Schmitz, E. Cloutis, A. Brown, D. Flannery, O. Gasnault, J. Grotzinger, S. Gupta, L. Kah, P. Kelemen, K. Kinch, J. Núñez, Diverse Lava Flow Morphologies in the Stratigraphy of the Jezero Crater Floor. *JGR Planets* **128**, e2022JE007446 (2023).

59. S.-E. Hamran, D. A. Paige, A. Allwood, H. E. F. Amundsen, T. Berger, S. Brovoll, L. Carter, T. M. Casademont, L. Damsgård, H. Dypvik, S. Eide, A. G. Fairén, R. Ghent, J. Kohler, M. T. Mellon, D. C. Nunes, D. Plettemeier, P. Russell, M. Siegler, M. J. Øyan, Ground penetrating radar observations of subsurface structures in the floor of Jezero crater, Mars. *Sci. Adv.* **8**, eabp8564 (2022).

60. M. S. Rice, J. R. Johnson, C. C. Million, M. St. Clair, B. N. Horgan, A. Vaughan, J. I. Núñez, B. Garczynski, S. Curtis, K. B. Kinch, M. Merusi, A. Hayes, J. F. Bell, L. Duflot, K. Lapo, A. A. Evans, A. Eng, E. Cloutis, A. Brown, A. M. Annex, Spectral variability of rocks and soils on the Jezero crater floor: A summary of multispectral observations from *Perseverance's* Mastcam-Z instrument. *JGR Planets*, e2022JE007548 (2023).

61. A. Corpolongo, R. S. Jakubek, A. S. Burton, A. J. Brown, A. Yanchilina, A. D. Czaja, A. Steele, B. V. Wogsland, C. Lee, D. Flannery, D. Baker, E. A. Cloutis, E. Cardarelli, E. L. Scheller, E. L. Berger, F. M. McCubbin, J. R. Hollis, K. Hickman-Lewis, K. Steadman, K. Uckert, L. DeFlores, L. Kah, L. W. Beegle, M. Fries, M. Minitti, N. C. Haney, P. Conrad, R. V. Morris, R. Bhartia, R. Roppel, S. Siljeström, S. A. Asher, S. V. Bykov, S. Sharma, S. Shkolyar, T. Fornaro, W. Abbey, SHERLOC Raman Mineral Class Detections of the Mars 2020 Crater Floor Campaign. *JGR Planets* **128**, e2022JE007455 (2023).

62. S. Siljeström, A. D. Czaja, A. Corpolongo, E. L. Berger, A. Y. Li, E. Cardarelli, W. Abbey, S. A. Asher, L. W. Beegle, K. C. Benison, R. Bhartia, B. L. Bleefeld, A. S. Burton, S. V. Bykov, B. Clark, L. DeFlores, B. L. Ehlmann, T. Fornaro, A. Fox, F. Gómez, K. Hand, N. C. Haney, K. Hickman-Lewis, W. F. Hug, S. Imbeah, R. S. Jakubek, L. C. Kah, L. Kivrak, C. Lee, Y. Liu, J. Martínez-Frías, F. M. McCubbin, M. Minitti, K. Moore, R. V. Morris, J. I. Núñez, J. T. Osterhout, Y. Y. Phua, N. Randazzo, J. R. Hollis, C. Rodriguez, R. Roppel, E. L. Scheller, M. Sephton, S. K. Sharma, S. Sharma, K. Steadman, A. Steele, M. Tice, K. Uckert, S. VanBommel, A. J. Williams, K. H. Williford, K. Winchell, M. K. Wu, A. Yanchilina, M. Zorzano, Evidence of Sulfate-Rich Fluid Alteration in Jezero Crater Floor, Mars. *JGR Planets* **129**, e2023JE007989 (2024).

63. R. C. Wiens, A. Udry, O. Beyssac, C. Quantin-Nataf, N. Mangold, A. Cousin, L. Mandon, T. Bosak, O. Forni, S. M. McLennan, V. Sautter, A. Brown, K. Benzerara, J. R. Johnson, L. Mayhew, S. Maurice, R. B. Anderson, S. M. Clegg, L. Crumpler, T. S. J. Gabriel, P. Gasda, J. Hall, B. H. N. Horgan, L. Kah, C. Legett, J. M. Madariaga, P.-Y. Meslin, A. M. Ollila, F. Poulet, C. Royer, S. K. Sharma, S. Siljeström, J. I. Simon, T. E. Acosta-Maeda, C. Alvarez-Llamas, S. M. Angel, G. Arana, P. Beck, S. Bernard, T. Bertrand, B. Bousquet, K. Castro, B. Chide, E. Clavé, E. Cloutis, S. Connell, E. Dehouck, G. Dromart, W. Fischer, T. Fouchet, R. Francis, J. Frydenvang, O. Gasnault, E. Gibbons, S. Gupta, E. M.

Hausrath, X. Jacob, H. Kalucha, E. Kelly, E. Knutsen, N. Lanza, J. Laserna, J. Lasue, S. Le Mouélic, R. Leveille, G. Lopez Reyes, R. Lorenz, J. A. Manrique, J. Martinez-Frias, T. McConnochie, N. Melikechi, D. Mimoun, F. Montmessin, J. Moros, N. Murdoch, P. Pilleri, C. Pilorget, P. Pinet, W. Rapin, F. Rull, S. Schröder, D. L. Shuster, R. J. Smith, A. E. Stott, J. Tarnas, N. Turenne, M. Veneranda, D. S. Vogt, B. P. Weiss, P. Willis, K. M. Stack, K. H. Williford, K. A. Farley, The SuperCam Team, Compositionally and density stratified igneous terrain in Jezero crater, Mars. *Sci. Adv.* **8**, eabo3399 (2022).

64. K. Lodders, A survey of shergottite, nakhlite and chassigny meteorites whole-rock compositions. *Meteoritics & Planetary Science* **33**, A183–A190 (1998).

65. W. Cross, J. P. Iddings, L. V. Pirsson, H. S. Washington, A Quantitative Chemico-Mineralogical Classification and Nomenclature of Igneous Rocks. *The Journal of Geology* **10**, 555–690 (1902).

66. C. D. K. Herd, J. J. Papike, A. J. Brearley, Oxygen fugacity of martian basalts from electron microprobe oxygen and TEM-EELS analyses of Fe-Ti oxides. *American Mineralogist* **86**, 1015–1024 (2001).

67. J. A. Berger, R. Gellert, N. I. Boyd, P. L. King, M. A. McCraig, C. D. O'Connell-Cooper, M. E. Schmidt, J. G. Spray, L. M. Thompson, S. J. V. VanBommel, A. S. Yen, Elemental Composition and Chemical Evolution of Geologic Materials in Gale Crater, Mars: APXS Results From Bradbury Landing to the Vera Rubin Ridge. *J. Geophys. Res. Planets* **125** (2020).

68. J. Brückner, G. Dreibus, R. Rieder, H. Wänke, Refined data of Alpha Proton X-ray Spectrometer analyses of soils and rocks at the Mars Pathfinder site: Implications for surface chemistry: SURFACE CHEMISTRY BY MARS PATHFINDER APXS. *J.-Geophys.-Res.* **108** (2003).

69. P. H. Edwards, J. C. Bridges, R. Wiens, R. Anderson, D. Dyar, M. Fisk, L. Thompson, P. Gasda, J. Filiberto, S. P. Schwenzer, D. Blaney, I. Hutchinson, Basalt–trachybasalt samples in Gale Crater, Mars. *Meteorit & Planetary Scien* **52**, 2931–2410 (2017).

70. D. W. Ming, R. Gellert, R. V. Morris, R. E. Arvidson, J. Brückner, B. C. Clark, B. A. Cohen, C. d'Uston, T. Economou, I. Fleischer, G. Klingelhöfer, T. J. McCoy, D. W. Mittlefehldt, M. E. Schmidt, C. Schröder, S. W. Squyres, E. Tréguier, A. S. Yen, J. Zipfel, Geochemical properties of rocks and soils in Gusev Crater, Mars: Results of the Alpha Particle X-Ray Spectrometer from Cumberland Ridge to Home Plate. *J. Geophys. Res.* **113**, E12S39 (2008).

71. G. Dreibus, F. Wlotzka, W. Huisl, E. Jagoutz, A. Kubny, B. Spettel, Chemistry and Petrology of the Most Feldspatic Shergottite: Dhofar 378. *Meteoritics and Planetary Science Supplement* **37**, A43 (2002).

72. Y. Ikeda, H. Takeda, M. Kimura, A. Suzuki, A New Shergottite from Oman, Dhofar 378. 1434 (2002).

73. A. E. Bence, J. J. Papike, Pyroxenes as recorders of lunar basalt petrogenesis: Chemical trends due to crystal-liquid interaction. *Lunar and Planetary Science Conference Proceedings* **3**, 431 (1972).

74. T. L. Grove, A. E. Bence, Experimental study of pyroxene-liquid interaction in quartz-normative basalt 15597. *Lunar and Planetary Science Conference Proceedings* **2**, 1549–1579 (1977).

75. A. Udry, G. H. Howarth, T. J. Lapen, M. Righter, Petrogenesis of the NWA 7320 enriched martian gabbroic shergottite: Insight into the martian crust. *Geochimica et Cosmochimica Acta* **204**, 1–18 (2017).

76. C. J. Aramovich, C. D. K. Herd, J. J. Papike, Symplectites derived from metastable phases in martian basaltic meteorites. *American Mineralogist* **87**, 1351–1359 (2002).

77. D. H. Lindsley, B. T. C. Davis, I. D. Macgregor, Ferrosilite ($FeSiO_3$): Synthesis at High Pressures and Temperatures. *Science* **144**, 73–74 (1964).

78. D. H. Lindsley, C. W. Burnham, Pyroxferroite: Stability and X-ray Crystallography of Synthetic $Ca_{0.15}Fe_{0.85}SiO_3$ Pyroxenoid. *Science* **168**, 364–367 (1970).

79. L. Mandon, C. Quantin-Nataf, C. Royer, P. Beck, T. Fouchet, J. R. Johnson, E. Dehouck, S. Le Mouélic, F. Poulet, F. Montmessin, C. Pilorget, O. Gasnault, O. Forni, L. E. Mayhew, O. Beyssac, T. Bertrand, E. Clavé, P. Pinet, A. J. Brown, C. Legett, J. Tarnas, E. A. Cloutis, G. Poggiali, T. Fornaro, S. Maurice, R. C. Wiens, The SuperCam Team, Reflectance of Jezero Crater Floor: 2. Mineralogical Interpretation. *JGR Planets* **128**, e2022JE007450 (2023).

80. B. H. N. Horgan, R. B. Anderson, G. Dromart, E. S. Amador, M. S. Rice, The mineral diversity of Jezero crater: Evidence for possible lacustrine carbonates on Mars. *Icarus* **339**, 113526 (2020).

81. C. M. Heirwegh, W. T. Elam, L. P. O'Neil, K. P. Sinclair, A. Das, The focused beam X-ray fluorescence elemental quantification software package PIQUANT. *Spectrochimica Acta Part B: Atomic Spectroscopy* **196**, 106520 (2022).

82. D. W. Beaty, M. M. Grady, H. Y. McSween, E. Sefton-Nash, B. L. Carrier, F. Altieri, Y. Amelin, E. Ammannito, M. Anand, L. G. Benning, J. L. Bishop, L. E. Borg, D. Boucher, J. R. Brucato, H. Busemann, K. A. Campbell, A. D. Czaja, V. Debaille, D. J. Des Marais, M. Dixon, B. L. Ehlmann, J. D. Farmer, D. C. Fernandez-Remolar, J. Filiberto, J. Fogarty, D. P. Glavin, Y. S. Goreva, L. J. Hallis, A. D. Harrington, E. M. Hausrath, C. D. K. Herd, B. Horgan, M. Humayun, T. Kleine, J. Kleinhenz, R. Mackelprang, N. Mangold, L. E. Mayhew, J. T. McCoy, F. M. McCubbin, S. M. McLennan, D. E. Moser, F. Moynier, J. F. Mustard, P. B. Niles, G. G. Ori, F. Raulin, P. Rettberg, M. A. Rucker, N. Schmitz, S. P. Schwenzer, M. A. Sephton, R. Shaheen, Z. D. Sharp, D. L. Shuster, S. Siljeström, C. L. Smith, J. A. Spry, A. Steele, T. D. Swindle, I. L. Ten Kate, N. J. Tosca, T. Usui, M. J. Van Kranendonk, M. Wadhwa, B. P. Weiss, S. C. Werner, F. Westall, R. M. Wheeler, J. Zipfel, M. P. Zorzano, The potential science and engineering value of samples delivered to

Earth by Mars sample return: International MSR Objectives and Samples Team (iMOST). *Meteorit & Planetary Scien* **54** (2019).

83. J. R. Christian, S. J. VanBommel, W. T. Elam, B. Ganly, J. A. Hurowitz, C. M. Heirwegh, A. C. Allwood, B. C. Clark, T. V. Kizovski, A. L. Knight, Statistical characterization of PIXL trace element detection limits. *Acta Astronautica* **212**, 534–540 (2023).

84. A. Das, C. M. Heirwegh, N. Gao, B. C. Clark, W. T. Elam, L. A. Wade, A. C. Allwood, J. A. Hurowitz, Energy Dependence of X-ray Beam size Produced by Polycapillary X-Ray Optics. *X-Ray Spectrometry* (2024).

85. T. A. Goudge, J. F. Mustard, J. W. Head, C. I. Fassett, S. M. Wiseman, Assessing the mineralogy of the watershed and fan deposits of the Jezero crater paleolake system, Mars. *JGR Planets* **120**, 775–808 (2015).

86. G. F. Zellmer, Gaining acuity on crystal terminology in volcanic rocks. *Bull Volcanol* **83**, 78 (2021).

87. J. Semprich, J. Filiberto, High-pressure metamorphic mineralogy of the Martian crust with implications for density and seismic profiles. *Meteorit & Planetary Scien* **55**, 1600–1614 (2020).

88. J. A. D. Connolly, K. Petrini, An automated strategy for calculation of phase diagram sections and retrieval of rock properties as a function of physical conditions. *Journal Metamorphic Geology* **20**, 697–708 (2002).

89. W. A. Bohrson, F. J. Spera, M. S. Ghiorso, G. A. Brown, J. B. Creamer, A. Mayfield, Thermodynamic Model for Energy-Constrained Open-System Evolution of Crustal Magma Bodies Undergoing Simultaneous Recharge, Assimilation and Crystallization: the Magma Chamber Simulator. *Journal of Petrology* **55**, 1685–1717 (2014).

90. J. B. Balta, H. Y. McSween, Application of the MELTS algorithm to Martian compositions and implications for magma crystallization. *JGR Planets* **118**, 2502–2519 (2013).

91. J. Filiberto, R. Dasgupta, Fe2+–Mg partitioning between olivine and basaltic melts: Applications to genesis of olivine-phyric shergottites and conditions of melting in the Martian interior. *Earth and Planetary Science Letters* **304**, 527–537 (2011).

92. B. Bultel, C. Quantin-Nataf, M. Andréani, H. Clénet, L. Lozac'h, Deep alteration between Hellas and Isidis Basins. *Icarus* **260**, 141–160 (2015).

93. A. Rani, A. Basu Sarbadhikari, D. R. Hood, O. Gasnault, S. Nambiar, S. Karunatillake, Consolidated Chemical Provinces on Mars: Implications for Geologic Interpretations. *Geophysical Research Letters* **49**, e2022GL099235 (2022).

94. B. L. Ehlmann, J. F. Mustard, G. A. Swayze, R. N. Clark, J. L. Bishop, F. Poulet, D. J. Des Marais, L. H. Roach, R. E. Milliken, J. J. Wray, O. Barnouin-Jha, S. L. Murchie,

Identification of hydrated silicate minerals on Mars using MRO-CRISM: Geologic context near Nili Fossae and implications for aqueous alteration. *J. Geophys. Res.* **114**, 2009JE003339 (2009).

95. L. Mandon, C. Quantin-Nataf, P. Thollot, N. Mangold, L. Lozac'h, G. Dromart, P. Beck, E. Dehouck, S. Breton, C. Millot, M. Volat, Refining the age, emplacement and alteration scenarios of the olivine-rich unit in the Nili Fossae region, Mars. *Icarus* **336**, 113436 (2020).

96. K. M. Stack, L. R. W. Ives, S. Gupta, M. P. Lamb, M. Tebolt, G. Caravaca, J. P. Grotzinger, P. Russell, D. L. Shuster, A. J. Williams, H. Amundsen, S. Alwmark, A. M. Annex, R. Barnes, J. Bell, O. Beyssac, T. Bosak, L. S. Crumpler, E. Dehouck, S. J. Gwizd, K. Hickman-Lewis, B. H. N. Horgan, J. Hurowitz, H. Kalucha, O. Kanine, C. Lesh, J. Maki, N. Mangold, N. Randazzo, C. Seeger, R. M. E. Williams, A. Brown, E. Cardarelli, H. Dypvik, D. Flannery, J. Frydenvang, S. -E. Hamran, J. I. Núñez, D. Paige, J. I. Simon, M. Tice, C. Tate, R. C. Wiens, Sedimentology and Stratigraphy of the Shenandoah Formation, Western Fan, Jezero Crater, Mars. *JGR Planets* **129**, e2023JE008187 (2024).

97. R. P. Rapp, E. B. Watson, Dehydration Melting of Metabasalt at 8-32 kbar: Implications for Continental Growth and Crust-Mantle Recycling. *Journal of Petrology* **36**, 891–931 (1995).

98. J. D. Tarnas, K. M. Stack, M. Parente, A. H. D. Koeppel, J. F. Mustard, K. R. Moore, B. H. N. Horgan, F. P. Seelos, E. A. Cloutis, P. B. Kelemen, D. Flannery, A. J. Brown, K. R. Frizzell, P. Pinet, Characteristics, Origins, and Biosignature Preservation Potential of Carbonate-Bearing Rocks Within and Outside of Jezero Crater. *JGR Planets* **126**, e2021JE006898 (2021).

99. A. J. Brown, L. Kah, L. Mandon, R. Wiens, P. Pinet, E. Clavé, S. L. Mouélic, A. Udry, P. J. Gasda, C. Royer, K. Hickman-Lewis11, A. Cousin, J. I. Simon, J. Comellas14, E. Cloutis, T. Fouchet, A. G. Fairén, S. Connell, D. Flannery, B. Horgan, L. Mayhew, A. Treiman, J. I. Núñez, B. Wogsland, K. Benzerara, H. E. F. Amundsen, C. Quantin-Nataf, K. P. Hand, V. Debaille, A. Essunfeld, P. Beck, N. J. Tosca, J. M. Madariaga, E. Ravanis, Properties of the Nili Fossae Olivine-clay-carbonate lithology: orbital and in situ at S\'e\'itah. arXiv arXiv:2206.13380 [Preprint] (2022). http://arxiv.org/abs/2206.13380.

100. K. A. Farley, K. H. Williford, K. M. Stack, R. Bhartia, A. Chen, M. de la Torre, K. Hand, Y. Goreva, C. D. K. Herd, R. Hueso, Y. Liu, J. N. Maki, G. Martinez, R. C. Moeller, A. Nelessen, C. E. Newman, D. Nunes, A. Ponce, N. Spanovich, P. A. Willis, L. W. Beegle, J. F. Bell, A. J. Brown, S.-E. Hamran, J. A. Hurowitz, S. Maurice, D. A. Paige, J. A. Rodriguez-Manfredi, M. Schulte, R. C. Wiens, Mars 2020 Mission Overview. *Space Science Reviews* **216**, 142 (2020).

101. P. R. Lawson, T. V. Kizovski, M. M. Tice, B. C. Clark, S. J. VanBommel, D. R. Thompson, L. A. Wade, R. W. Denise, C. M. Heirwegh, W. T. Elam, M. E. Schmidt, Y. Liu, A. C. Allwood, M. S. Gilbert, B. J. Bornstein, Adaptive sampling with PIXL on the Mars Perseverance rover. *Icarus*, doi: http://arxiv.org/abs/2405.14471 (2024).

102. C. C. Liebe, D. A. K. Pedersen, A. Allwood, A. Bang, S. Bartman, M. Benn, T. Denver, G. Doran, M. C. Foote, A. Jorgensen, J. L. Jorgensen, P. Meras, T. P. Setterfield, R. Sharrow, M. E. Sondheim, L. Timmermann, S. Tsai, L. A. Wade, D. W. Wilson, Autonomous Sensor System for Determining Instrument Position Relative to Unknown Surfaces Utilized on Mars Rover. *IEEE Sensors J.* **22**, 18933–18943 (2022).

103. D. A. K. Pedersen, C. C. Liebe, J. L. Jorgensen, Structured Light System on Mars Rover Robotic Arm Instrument. *IEEE Trans. Aerosp. Electron. Syst.* **55**, 1612–1623 (2019).

104. D. A. Klevang, C. C. Liebe, J. Henneke, J. L. Jørgensen, R. Sharrow, T. Setterfield, L. Wade, M. Sondheim, M. Foote, W. T. Elam, C. M. Heirwegh, J. Hurowitz, A. Allwood, Pre-flight Geometric and Optical Calibration of the Planetary Instrument for X-ray Lithochemistry (PIXL). *Space Sci Rev* **219**, 11 (2023).

105. T. Barber, S. Davidoff, pixlise/piquant: 3.2.11 Open Source, version v3.2.11, Zenodo (2022); https://doi.org/10.5281/ZENODO.6959225.

106. D. A. Klevang, J. Henneke, M. Benn, T. Denver, P. S. Jørgensen, J. L. Jørgensen, L. A. Wade, R. Denise, W. T. Elam, J. Van Beek, M. Cable, J. Hurowitz, A. Allwood, "Pre- and In-flight Performance of Terrain Relative Navigation on PIXL's Micro Context Camera, M2020" in *2024 IEEE Aerospace Conference* (IEEE, Big Sky, MT, USA, 2024; https://ieeexplore.ieee.org/document/10521246/), pp. 1–14.

107. J. Henneke, D. Klevang, Y. Liu, J. Jørgensen, T. Denver, M. Rice, S. VanBommel, C. Toldbo, J. Hurowitz, M. Tice, N. Tosca, J. Johnson, A. Winhold, A. Allwood, J. Bell, A Radiometric Correction Method and Performance Characteristics for PIXL's Multispectral Analysis Using LEDs. *Space Sci Rev* **219**, 68 (2023).

108. W. Nikonow, D. Rammlmair, Risk and benefit of diffraction in Energy Dispersive X-ray fluorescence mapping. *Spectrochimica Acta Part B: Atomic Spectroscopy* **125**, 120–126 (2016).

109. S. Alwmark, B. Horgan, A. Udry, A. Bechtold, S. Fagents, E. Ravanis, L. Crumpler, N. Schmitz, E. Cloutis, A. Brown, D. Flannery, O. Gasnault, J. Grotzinger, S. Gupta, L. Kah, P. Kelemen, K. Kinch, J. Núñez, Diverse Lava Flow Morphologies in the Stratigraphy of the Jezero Crater Floor. *JGR Planets* **128**, e2022JE007446 (2023).

110. E. M. Hausrath, C. T. Adcock, A. Bechtold, P. Beck, K. Benison, A. Brown, E. L. Cardarelli, N. A. Carman, B. Chide, J. Christian, B. C. Clark, E. Cloutis, A. Cousin, O. Forni, T. S. J. Gabriel, O. Gasnault, M. Golombek, F. Gómez, M. H. Hecht, T. L. J. Henley, J. Huidobro, J. Johnson, M. W. M. Jones, P. Kelemen, A. Knight, J. A. Lasue, S. Le Mouélic, J. M. Madariaga, J. Maki, L. Mandon, G. Martinez, J. Martínez-Frías, T. H. McConnochie, P. -Y. Meslin, M. -P. Zorzano, H. Newsom, G. Paar, N. Randazzo, C. Royer, S. Siljeström, M. E. Schmidt, S. Schröder, M. A. Sephton, R. Sullivan, N. Turenne, A. Udry, S. VanBommel, A. Vaughan, R. C. Wiens, N. Williams, the SuperCam team and the Regolith working group, An Examination of Soil Crusts on the Floor of Jezero Crater, Mars. *JGR Planets* **128**, e2022JE007433 (2023).

111. B. L. Carrier, W. J. Abbey, L. W. Beegle, R. Bhartia, Y. Liu, Attenuation of Ultraviolet Radiation in Rocks and Minerals: Implications for Mars Science. *JGR Planets* **124**, 2599–2612 (2019).

112. R. V. Morris, N. C. Haney, R. S. Jakubek, S. A. Eckley, F. M. McCubbin, M. D. Fries, C. B. Agee, M. E. Schmidt, E. L. Berger, A. Yanchilina, Deep UV Raman and Chemical Analysis of Crystalline Feldspar and Pyroxene in Polymict Martian Meteorite Northwest Africa 10922: An Analog Study for Mars 2020 SHERLOC and PIXL and MSL CheMin Instruments. **2806**, 2748 (2023).

113. J. F. Bell, J. N. Maki, G. L. Mehall, M. A. Ravine, M. A. Caplinger, Z. J. Bailey, S. Brylow, J. A. Schaffner, K. M. Kinch, M. B. Madsen, A. Winhold, A. G. Hayes, P. Corlies, C. Tate, M. Barrington, E. Cisneros, E. Jensen, K. Paris, K. Crawford, C. Rojas, L. Mehall, J. Joseph, J. B. Proton, N. Cluff, R. G. Deen, B. Betts, E. Cloutis, A. J. Coates, A. Colaprete, K. S. Edgett, B. L. Ehlmann, S. Fagents, J. P. Grotzinger, C. Hardgrove, K. E. Herkenhoff, B. Horgan, R. Jaumann, J. R. Johnson, M. Lemmon, G. Paar, M. Caballo-Perucha, S. Gupta, C. Traxler, F. Preusker, M. S. Rice, M. S. Robinson, N. Schmitz, R. Sullivan, M. J. Wolff, The Mars 2020 Perseverance Rover Mast Camera Zoom (Mastcam-Z) Multispectral, Stereoscopic Imaging Investigation. *Space Science Reviews* **217**, 24 (2021).

114. R. L. Klima, C. M. Pieters, J. W. Boardman, R. O. Green, J. W. Head, P. J. Isaacson, J. F. Mustard, J. W. Nettles, N. E. Petro, M. I. Staid, J. M. Sunshine, L. A. Taylor, S. Tompkins, New insights into lunar petrology: Distribution and composition of prominent low-Ca pyroxene exposures as observed by the Moon Mineralogy Mapper ($M^3$). *J. Geophys. Res.* **116**, E00G06 (2011).

115. V. C. Kress, I. S. E. Carmichael, The compressibility of silicate liquids containing Fe2O3 and the effect of composition, temperature, oxygen fugacity and pressure on their redox states. *Contr. Mineral. and Petrol.* **108**, 82–92 (1991).

116. D. R. Wones, M. C. Gilbert, The fayalite-magnetite-quartz assemblage between 600 and 800 C. *American Journal of Science* **267**, 480–488 (1969).

117. T. J. B. Holland, R. Powell, An improved and extended internally consistent thermodynamic dataset for phases of petrological interest, involving a new equation of state for solids. *Journal of Metamorphic Geology* **29**, 333–383 (2011).

118. T. J. B. Holland, E. C. R. Green, R. Powell, Melting of Peridotites through to Granites: A Simple Thermodynamic Model in the System KNCFMASHTOCr. *Journal of Petrology* **59**, 881–900 (2018).

119. R. W. White, R. Powell, G. L. Clarke, The interpretation of reaction textures in Fe-rich metapelitic granulites of the Musgrave Block, central Australia: constraints from mineral equilibria calculations in the system K2O–FeO–MgO–Al2O3–SiO2–H2O–TiO2–Fe2O3. *Journal of metamorphic Geology* **20**, 41–55 (2002).

120. T. Holland, R. Powell, Activity–composition relations for phases in petrological calculations: an asymmetric multicomponent formulation. *Contributions to Mineralogy and Petrology* **145**, 492–501 (2003).

121. E. S. Jennings, T. J. B. Holland, A Simple Thermodynamic Model for Melting of Peridotite in the System NCFMASOCr. *Journal of Petrology* **56**, 869–892 (2015).

122. M. S. Ghiorso, G. A. R. Gualda, An H2O–CO2 mixed fluid saturation model compatible with rhyolite-MELTS. *Contrib Mineral Petrol* **169**, 53 (2015).

123. G. A. R. Gualda, M. S. Ghiorso, R. V. Lemons, T. L. Carley, Rhyolite-MELTS: a Modified Calibration of MELTS Optimized for Silica-rich, Fluid-bearing Magmatic Systems. *Journal of Petrology* **53**, 875–890 (2012).

124. M. S. Ghiorso, M. M. Hirschmann, P. W. Reiners, V. C. Kress, The pMELTS: A revision of MELTS for improved calculation of phase relations and major element partitioning related to partial melting of the mantle to 3 GPa. *Geochem Geophys Geosyst* **3**, 1–35 (2002).

125. D. F. Astudillo Manosalva, S. M. Elardo, Assessing the accuracy of phase equilibrium software in reproducing the liquidus multiple saturation conditions of lunar and Martian basalt compositions. *Meteorit & Planetary Scien*, maps.14117 (2024).

126. A. Jambon, J. A. Barrat, V. Sautter, Ph. Gillet, C. Göpel, M. Javoy, J. L. Joron, M. Lesourd, The basaltic shergottite Northwest Africa 856: Petrology and chemistry. *Meteorit & Planetary Scien* **37**, 1147–1164 (2002).

127. A. Udry, G. H. Howarth, C. D. K. Herd, J. M. D. Day, T. J. Lapen, J. Filiberto, What Martian Meteorites Reveal About the Interior and Surface of Mars. *J. Geophys. Res. Planets* **125** (2020).

128. C. D. K. Herd, E. L. Walton, C. B. Agee, N. Muttik, K. Ziegler, C. K. Shearer, A. S. Bell, A. R. Santos, P. V. Burger, J. I. Simon, M. J. Tappa, F. M. McCubbin, J. Gattacceca, F. Lagroix, M. E. Sanborn, Q.-Z. Yin, W. S. Cassata, L. E. Borg, R. E. Lindvall, T. S. Kruijer, G. A. Brennecka, T. Kleine, K. Nishiizumi, M. W. Caffee, The Northwest Africa 8159 martian meteorite: Expanding the martian sample suite to the early Amazonian. *Geochimica et Cosmochimica Acta* **218**, 1–26 (2017).

129. A. J. Irving, R. Andreasen, M. Righter, T. J. Lapen, H. Busemann, M. Izawa, D. E. Moser, P. P. Sipiera, Northwest Africa 4480 revisited: petrologic, isotopic and noble gas studies of an unshocked, maskelynite-free mafic shergottite with a long cosmic ray exposure age. *47th Lunar and Planetary Science Conference*, (abstract #2330) (2016).

130. A. J. Irving, S. M. Kuehner, R. L. Korotev, G. M. Hupe, Baby basaltic shergottite NWA 4480 : An Eu-anomalous Martian magma related to " lherzolitic " shergottites. *70th Annual Meteoritical Society Meeting* (2007).

131. A. J. Irving, S. M. Kuehner, C. . D. K. Herd, M. Gellissen, R. L. Korotev, I. Putchel, R. J. Walker, T. J. Lapen, D. Rumble III, Petrologic, elemental and multi-isotopic characterization of permafic olivine-phyric shergottite northwest africa 5789: a primitive magma derived from depleted martian mantle (abstract #1547). *41st Lunar and Planetary Science Conference*, doi: 10.1029/2005JE002605 (2010).

After 106 = Supplemental References Only

**Acknowledgments**

We are grateful to the Mars 2020 Science and Engineering team members who participated in tactical and strategic science operations. We also thank Suniti Karunatillake and two anonymous reviewers who provided constructive feedback that improved the quality of the final manuscript.

**Funding:**

Canadian Space Agency (CSA) M2020 Participating Scientist Program grant 21EXPMAPS CSA 2021 (MES, TVK, JL, TLJH)
NASA, Jet Propulsion laboratory, California Institute of Technology 80NMOO18D0004 (ACA, YL, AHT, JAH, MMT, MLC, BCC, CMH, AY)
NASA's Mars 2020 Project via a subcontract from the California Institute of Technology/Jet Propulsion to Arizona State University for the Mastcam-Z science team, JPL subcontract 1511125 (BHNH)
NASA Participating Scientist Program 80NMOO18D0004 (SJV, ALK, JRC) and 80NSSC21K0327 (LSC)
Mars 2020 Return Sample Science Participating Scientist supported by NASA Mars Exploration Program (JIS)
Canadian Space Agency (CSA) M2020 Returned Sample Participating Scientist Program grant 21EXPMAPS CSA 2021 (CDKH, SB, NR)
ISFM Mission Enabling Work Package at the Johnson Space Center (RVM)

**Author contributions:**

MES led the writing of the manuscript.
MES, TVK, YL, JDHM, MMT, LSC, prepared the original draft with input from JAH, D.A.K.P., AHT, SB, NJT, SJV, BHNH.
All authors provided input to the manuscript through discussion, editing, or reviewing. MES, TVK, YL, MMT, DAKP, SJV, ALK, JL, JRC contributed to the design, execution, and analysis of PIXL observations.
All authors contributed to the selection and geologic interpretation of the rocks discussed here.
MES, TVK, MMT, SJV, ALK, JL, YL, CMH performed data processing and analysis.
MES, TVK, LSC, YL, JL, DAKP, MMT, TLJH, RVM prepared visualizations.
Project management of the PIXL investigation was by ACA, JAH, MLC.

**Competing interests:** The authors declare that they have no competing interests.

**Data and materials availability:** All data needed to evaluate the conclusions in the paper are present in the paper and/or the Supplementary Materials. PIXL images and data used in this paper are available on the Planetary Data System (PDS; doi:10.17189/1522645; https://pds.nasa.gov/ds-view/pds/viewBundle.jsp?identifier=urn%3Anasa%3Apds%3Amars2020_pixl&version=1.0)

## Supplementary Materials

Supplementary Materials (separate document) include:

Supplementary Text
Figs. S1 to S20
Tables S1 to S2, S4, S7
References (107 to 125)

Supplementary Tables S3, S5, S6 are separate Excel Spreadsheets

Science Advances
AAAS

# Supplementary Materials for

# Diverse and highly differentiated lava suite in Jezero crater, Mars: Constraints on intracrustal magmatism revealed by Mars 2020 PIXL

Mariek E. Schmidt *et al.*

*Corresponding author. Email: mschmidt2@brocku.ca

**This PDF file includes:**

Supplementary Text
Figs. S1 to S20
Tables S1 to S2, S4, S7
References (107 to 128)

**Other Supplementary Materials for this manuscript include the following:**
Data files Tables S3, S5, S6

# Supplementary Text

PIXL scan parameters

PIXL analysis parameters for the Máaz fm targets are presented in Table S1. Parameters include the type and size of PIXL scan that was conducted (line, grid, or map), the number of individual X-ray points , whether MCC color stack imaging was captured, the quantification, and list of elements. PIXL scan footprints on MCC grayscale context images are in Figure S1.

**Table S1. PIXL scan parameters for Máaz targets**

| Target | Type | Sol | RTT[1] | MCC[2] color stack | Surface Resolution | MCC FOV[3] | X-ray Scan (size) | Number PMC[4] |
|---|---|---|---|---|---|---|---|---|
| *Naltsos* | Rock-natural | 125 | 048300551 | N | | | Line (30 mm) | 121 |
| *Beaujeu 1* | Rock-natural | 138 | 052822532 | Y | 65 µm | 49x38 mm | Grid (20 $mm^2$, 1 mm spacing) | 225 |
| *Beaujeu 2* | Rock natural | 139 | 053281281 | Y | 65 µm | 49x38 mm | Map (7x4 $mm^2$) | 1653 |
| *Beaujeu 3* | Rock-natural | 141 | 053871108 | Y | 65 µm | 49x38 mm | Grid (20 $mm^2$, 1 mm spacing) | 225 |
| *Guillaumes* | Rock-abrasion | 167 | 063111681 | N | | | Map (6x6 $mm^2$) | 2809 |
| *Bellegarde* | Rock-abrasion | 187 | 069927431 | Y | 65 µm | 49x38 mm | Map (6x6 mm) | 2809 |
| *Montpezat 1* | Rock-abrasion | 347 | 122552837 | Y | 50 µm | 38x29 | 3 Line scan (30 mm) | 363 |
| *Montpezat 2* | Rock-abrasion | 348 | 123535879 | Y | 50 µm | 38x29 | Map (4x6 mm) | 2337 |
| *Alfalfa* | Rock-abrasion | 369 | 130744834 | Y | 50 µm | 38x29 mm | Map (7x7 mm) | 3249 |

[1] RTT is a 32-bit token (8 hexadecimal digits in human-readable form) generated by the rover command software, and is unique to each PIXL scan. [2]MCC is Micro-Context Camera. Y indicates color stack imaging was collected, and N indicates it was not. [3]FOV represents field of view. [4]The number of X-ray spots collected per scan.

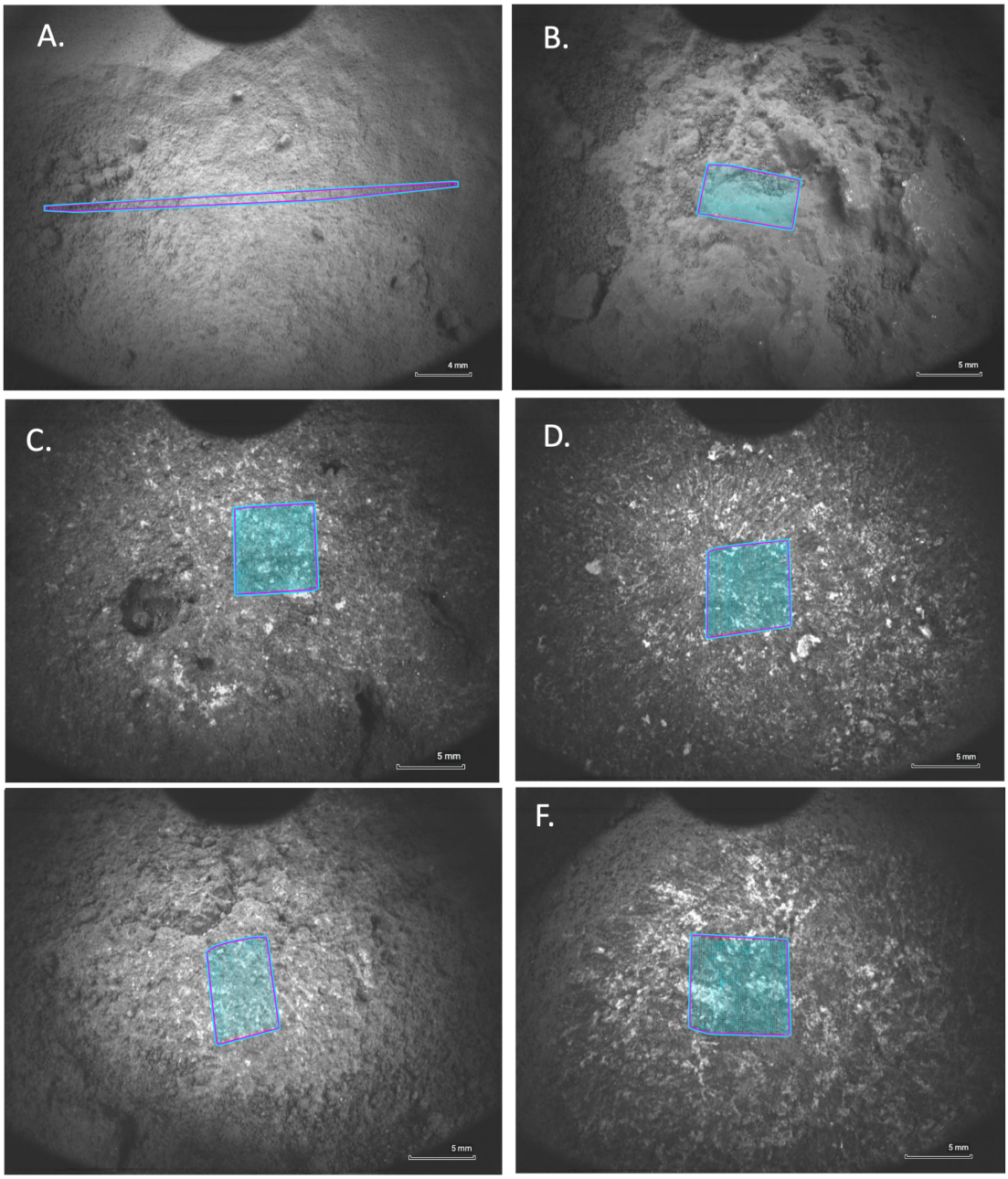


**Figure S1.** Grayscale PIXL MCC images of Máaz fm. targets with scan locations (Table S1); scan boundaries are in magenta and scan points are in cyan. A. *Naltsos* natural surface (PCW_0125_0678035034_000RCM_N004171204830055102180 75J02); B. *Beaujeu 2* natural surface (PCW_0140_0679334282_000RCM_N005181205328128116870 75J10); C. *Guillaumes* abrasion (PCW_0167_0681742883_000RCM_N006000006311168128120 75J06); D. *Bellegarde* abrasion (PCW_0187_0683527466_000RCM_N007000006992743128150 75J01); E. *Montpezat 2* abrasion (PCW_0350_0697993677_000RCM_N009298212353587923420 75J03); F. *Alfalfa* abrasion (PCW_0369_0699719117_000RCM_N011010813074483400030 75

**PIXL target information and Geologic Context**

PIXL analyzed four abraded Máaz fm rock targets (*Guillaumes*, *Bellegarde*, *Montpezat*, and *Alfalfa*) and two natural rock surfaces (*Naltsos* and *Beaujeu*) along its crater floor traverse (Figure 1, main text). Four core samples (*49*) for MSR were successfully collected from two of the Máaz outcrops (Rochette and Sid), corresponding with the *Bellegarde* and *Alfalfa* abrasions, respectively (*49*).

See (*53*) and (*35*) for detailed unit descriptions, maps, and links to orbital data; (*36*) for small-scale textural descriptions; and (*109*) for a detailed examination of the Artuby member.

**Table S2. Máaz PIXL target, sample, and formation names**

| PIXL Target | Target type | Sol | Formation | Member | Outcrop | Sample |
|---|---|---|---|---|---|---|
| *Naltsos* | Natural Surface | 125 | Máaz | Nataani | | |
| *Beaujeu* | Natural Surface | 138-141 | Máaz | Roubion | | |
| *Guillaumes* | Abrasion | 167 | Máaz | Roubion | Roubion | Roubion (empty) |
| *Bellegarde* | Abrasion | 187 | Máaz | Rochette | Rochette | Montdenier Montagnac |
| *Montpezat* | Abrasion | 347-348 | Máaz | Artuby | Rimplas | |
| *Alfalfa* | Abrasion | 369 | Máaz | Ch'al | Sid | Hahonih Atsah |

***Members in the Máaz formation***

*Ch'al member* is the highest stratigraphic material identified on the crater floor. It occurs as dark, massive irregularly fractured blocks on the order of one meter frequently bearing pits up to 1 cm, locally well-ventifacted in flute and groove patterns. The pits are interpreted as likely vesicles on the basis of the fundamental igneous nature of the rock and its lava sheet-like occurrence across the crater floor. Orbital data indicates that this rock unit extends east of the landing site across the crater floor for at least several kilometers.

*Nataani member* is one of the most widespread rock types exposed in the crater floor near the landing site. In orbital images it is a distinctive low-lying surface with widespread polygonal fracture patterns, sometimes referred to as appearing similar to flagstones or "pavers." The outcrops are relatively coarse and crystalline appearing at millimeter scales. Some polygonal blocks appear to be concentrically foliated much like the weathering phenomena that results in "corestones" on Earth. Outcrops of Nataani member rocks show a more tabular layered morphology compared to Cha'l. The Nataani member is overlain by rocks of the Ch'al member, separated by a possible disconformity developed during extended weathering of the Nataani member prior to emplacement of the Ch'al member.

*Rochette member* occurs as sub-orthogonally jointed outcrops and locally vesicular exposures that grade downward into dense aphanitic-appearing masses. In the type location, a tabular, prismatic block selected for the first successful core sample, the Rochette lithology is a dark, dense, and pitted pyroxene basalt capping Artuby Ridge. Supercam RMI images of *Rochette* are characterized by ~1 – 2 mm pits interpreted as vesicles, crystalline grains 1 mm and less, and rough sub-parallel linear fabric of rougher grains aligned with local vesicle elongations.

*Artuby member* is a horizontally foliated, or layered, coarse 1-3 mm granular material often expressed as centimeter-scale sheets and fissile layers. Outcrops are commonly exposed immediately underlying Rochette cap rocks. Elsewhere along the slopes of Artuby Ridge the Artuby member grades downward into lens-shaped, grussy outcrops with a concentrically foliated appearance. In RMI data *Artuby member* lithology is granular with elongate tabular and platy grains averaging 3 mm or larger generally arranged in a linear fabric consistent with outcrop foliations typical of *Artuby* exposures described here.

*Roubion member* outcrops are physically similar to *Nataani*, consisting of low-lying, polygonal exposures with granular surfaces, dark protuberances. The dark protuberances are scoriaceous and occupy the central zone within individual polygons. There is uncertainty about the stratigraphic position, as clear outcrops of *Roubion* were never visited in close proximity by *Perseverance*. At Mure, it is overlain by outcrops that were variably identified as *Nataani* member based on texture and multispectral data, or either *Rochette* member or *Ch'al* member based on texture alone. In the former case, *Roubion* underlies *Nataani*, whereas in the latter case it is possible that the exposures identified as *Roubion* are essentially the same member as *Nataani*. Differences in spectral characteristics between *Nataani* member rocks and *Roubion* member rocks however imply that these are different lithologies. More distant outcrops imaged by Mastcam-Z may show other examples of *Roubion* overlain by *Nataani*, and possible Roubion outcrops near the landing site appear to occur stratigraphically between *Rochette* and *Nataani*. However, identifying these different members based on subtle differences in outcrop texture and multispectral data alone is challenging so significant uncertainty remains around the stratigraphic position of the *Roubion* member. RMI data on *Roubion* are similar to *Nataani member*. *Roubion* has a surface that is rough at centimeter scales bearing slightly darker grains in a lighter matrix. The fabric as defined by these "grains" is roughly linear. Dark, circular 1 cm-diameter pits are notable in one WATSON image. No circular mineral phases or clasts are noted that could have been removed during surface exposure and erosion, so the field interpretation is that these are large and widely dispersed vesicles in the otherwise uniform rock mass.

***Geologic Context of Máaz Proximity Science Targets***

Outcrop Mastcam-Z and microscopic SHERLOC WATSON images of the Máaz PIXL scans are in Figures S2 and S3.

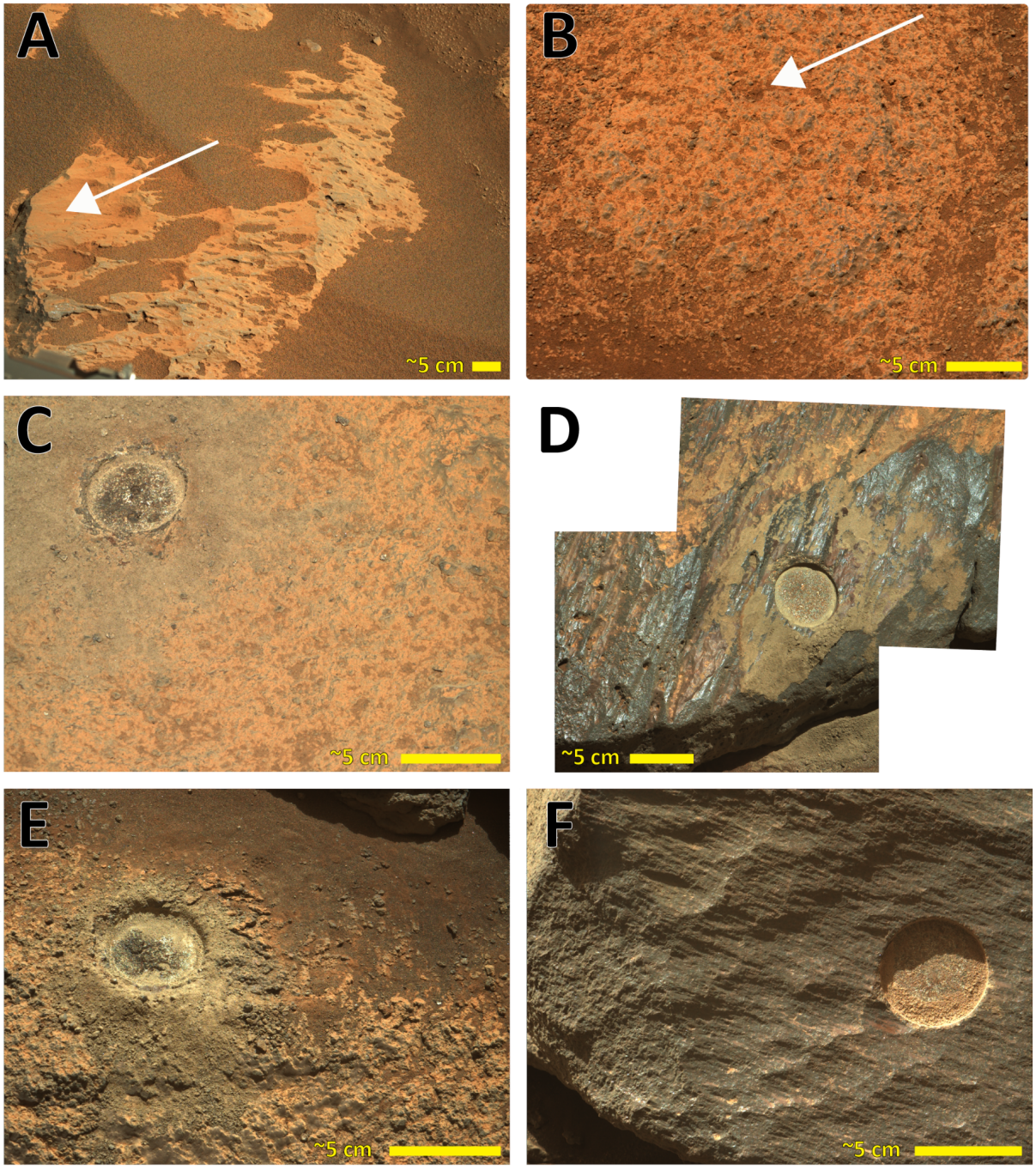


**Figure S2.** Mastcam-Z images of Maaz outcrops examined by PIXL. A: *Naltsos*, ZLF_0124_0677956192_659FDR_N0041712ZCAM08122_0340LMJ01; B: *Beaujeu*, ZLF_0139_0679276614_948FDR_N0051812ZCAM03182_1100LMJ01; C: *Guillaumes*, ZLF_0162_0681324559_774FDR_N0060000ZCAM03197_1100LMJ04 ; D: *Bellegarde*, Top: ZLF_0187_0683543136_911FDR_N0070000ZCAM08207_1100LMJ01 Bottom: ZLF_0187_0683543136_911FDR_N0070000ZCAM08207_1100LMJ01; E: *Montpezat*, ZLF_0347_0697744931_784FDR_N0092982ZCAM08376_1100LMJ01; F: *Alfalfa*. ZLF_0375_0700245124_053FDR_N0110108ZCAM08404_1100LMJ01.IMG.

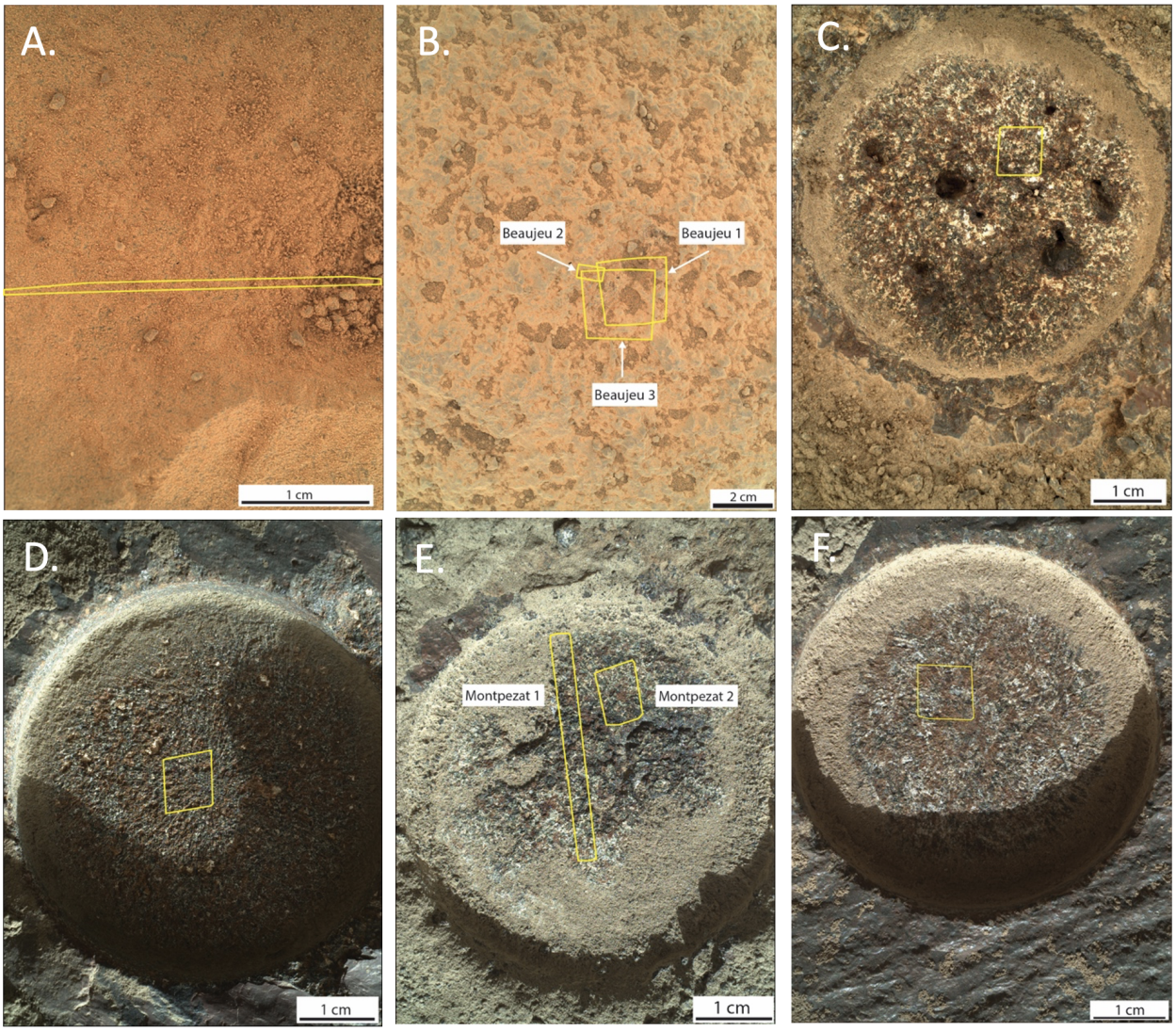


**Figure S3.** SHERLOC WATSON microscopic images of Máaz fm. proximity sciences targets with PIXL scan locations. A. *Naltsos*, SI1_0125_0678052470_660FDR_N0041712SRLC00001_000095J01; B. *Beaujeu*, SIF_0138_0679196077_156FDR_N0051812SRLC02502_0000LMJ02; C. *Guillaumes*, SIF_0160_0681145537_144FDR_N0060000SRLC01048_0000LMJ01; D. *Bellegarde*, SIF_0186_0683466639_699FDR_N0070000SRLC01021_0000LUJ0; E. *Montpezat 2*, SI1_0346_0697669267_585FDR_N0092982SRLC00033_000095J01; F. *Alfalfa*, IF_0367_0699525310_570FDR_N0110108SRLC01052_0000LMJ01.

*Naltsos (Sol 125)* is dust-covered natural surface on a vesicular block approximately 50 cm wide resting on the polygonally jointed and vesicular bedrock exposures of Rochette member. The local exposures are interpreted as the weathered exposures of the upper zones within a coarsely vesicular P type lava.

*Beaujeu (Sols 138-141)* is a natural surface in relatively flat, polygonally-jointed outcrop representative of the Roubion member forming a bench between the interior Máaz formation and the adjacent Seitah. The surface of the exposures are relatively rough at millimeter to centimeter scale and are coarsely crystalline. Because of the similar character of Nataani and Roubion outcrops, and the indeterminate character of the local stratigraphy, Nataani and Roubion outcrops could be the same lithology although there are several spectral results that imply otherwise (*35*).

*Guillaumes (Sol 167)* is an abrasion on a horizontal surface in the interior of a coarsely crystalline polygon of the Roubion member. The expression of much of the local outcrop is similar to that seen at the site of *Beaujeu,* that is, rough expires at centimeter scales and dark, somewhat scoriaceous-appearing protuberances on some surfaces. The associated coring attempt failed due to disintegration of the core. Physical characteristics suggest the presence of a weathered paleosurface and tentative spectral evidence of a weathering rind.

*Bellegarde (Sol 187)* abrasion was done on a prismatic block named Rochette, the first rock successfully cored and sampled (*Montdenier* and *Montagnac*), at the type locality for Rochette member atop Artuby Ridge. Rochette exposures in the vicinity are characterized by orthogonal joints in the surface resulting in a near-regular grid of joint blocks with intervening regolith much like that seen at the locality of *Naltsos*. Where exposed along the top of escarpment of Artuby Ridge, outcrops of this rock are dense, dark, moderately vesicular, and slab-like in form. Small pits within the Rochette target rock are interpreted as vesicles. The slab-like form, the orthogonal jointing (similar to that at *Naltsos*), and moderate to sparse vesicularity are all characteristic of the mid to upper levels within a P-type (vesicle poor/pipe-bearing) pahoehoe lava.

*Montpezat (Sols 347-348)* represents a horizontally laminated or layered outcrop of the Artuby member in the escarpment of Artuby Ridge. The exposure consists of materials that are coarse or granular at 1 to 2 mm scales arranged in horizontal to slightly southwest-dipping layers or planes between 1 cm and 50 cm thick. Vertical joints separated by 25 cm to 1 m together with the horizontal layers and the crumbling disintegration and rounding of edges in the exposures results in a granular, blocky and weathered outcrop expression. The abrasion *Montpezat* was acquired on the upper horizontal surface of a prominent ledge.

*Alfalfa (Sol 369)* abrasion was acquired within the *Ch'al member* on an isolated 50 cm x 80 cm angular block, "Sid", resting directly on a *Nataani member* substrate. Sid is one of many blocks scattered over the surface in the vicinity and lies approximately 60 meters west of the principal exposures of Ch'al member. Because of its isolation from the main occurrence of Ch'al, it may be an erosional outlier, so its orientation and vertical position within the Ch'al member are unconstrained. The interface between Sid and the underlying Nataani member is somewhat laminated and it is possible that the laminations represent evidence for regolith development on Nataani prior to the emplacement of Ch'al.

## Petrologic descriptions

A summary of rock textures, grain size, and modal proportions are presented in Table 3 of the main text. Outcrop and micro-scale context images are presented in Figures S2 and S3.

Additional mineralogical and textural information is provided by multispectral ratio images in Figure S4. The number of diffraction peaks superimposed on the individual X-ray spectra can be mapped across the PIXL scan area to visualize crystal structures (Figure S5).

*Naltsos (Sol 125)*
The first PIXL observation occurred at *Naltsos*, a dust-covered, coated natural surface (*110*). Windows through the dust and coating allow identification of elemental variations that indicate the presence of plagioclase feldspar, Fe-silicate (altered olivine), Fe-rich augite, and K-rich silicate (likely groundmass). This mineral assemblage is similar to what is observed in later Máaz targets, allowing correlation between targets.

*Beaujeu (Sols 138-141)*
Two grid scans and one map scan were acquired on a dust-covered, pitted natural rock surface at *Beaujeu*. Olivine-rich sand and dust accumulations occur within pits. A red coating with a composition similar to dust occurs as patches in the lower third portion of *Beaujeu 2* map scan. Relatively dust-free and coating-free areas of the rock contain plagioclase feldspar, Fe-silicate (altered olivine), Fe-rich augite, KSi-rich phase, and minor Fe-Ti oxide, and Ca phosphate. A ~1 mm olivine grain is identified in the left hand side of the *Beaujeu 2* map that appears to be part of the bedrock, but with high Mg (Fo ~48), more like the Séitáh olivines (*41*) than seen in the Máaz abraded targets. *Beaujeu* is interpreted to have a crystal-rich porphyritic texture because it contains crystalline feldspar that is up to ~1 mm and a relatively high proportion of the KSi-rich phase (32%) that is interpreted to be groundmass.

*Guillaumes (Sol 167)*
The *Guillaumes* abrasion of a pitted, dust-covered, coated surface, revealed a vuggy (likely vesicular) rock with interlocking light and dark-toned mineral grains. Bright white patches were found by PIXL to be rich in Ca sulfate and NaCl (Na-perchlorate identified by SHERLOC; (*46*). In order of decreasing modal abundance, plagioclase feldspar, Fe-rich augite, FeTi-oxide, Fe-silicate (altered olivine), Ca-phosphate, and KSi-rich mesostasis are identified. *Guillaumes* is interpreted to have a holocrystalline texture, likely formed in the interior of a lava flow.

*Bellegarde (Sol 187)*
The *Bellegarde* abrasion at the vesicular, ventifacted Rochette outcrop revealed a dark-toned, fine-grained texture. Blebs of Ca-sulfate occur in rimmed vugs, likely filling vesicles as amygdules. Patchy, reddish alteration also occurs. In order of decreasing modal abundance, KSi-rich groundmass, FeTi-oxide, Fe-rich augite, equivalent proportions of plagioclase feldspar and Fe-silicate (altered olivine), and Ca-phosphate are identified. *Bellegarde* is interpreted to have a micro-porphyritic texture on the basis of its high abundance of KSi-rich groundmass and <1 mm grain size.

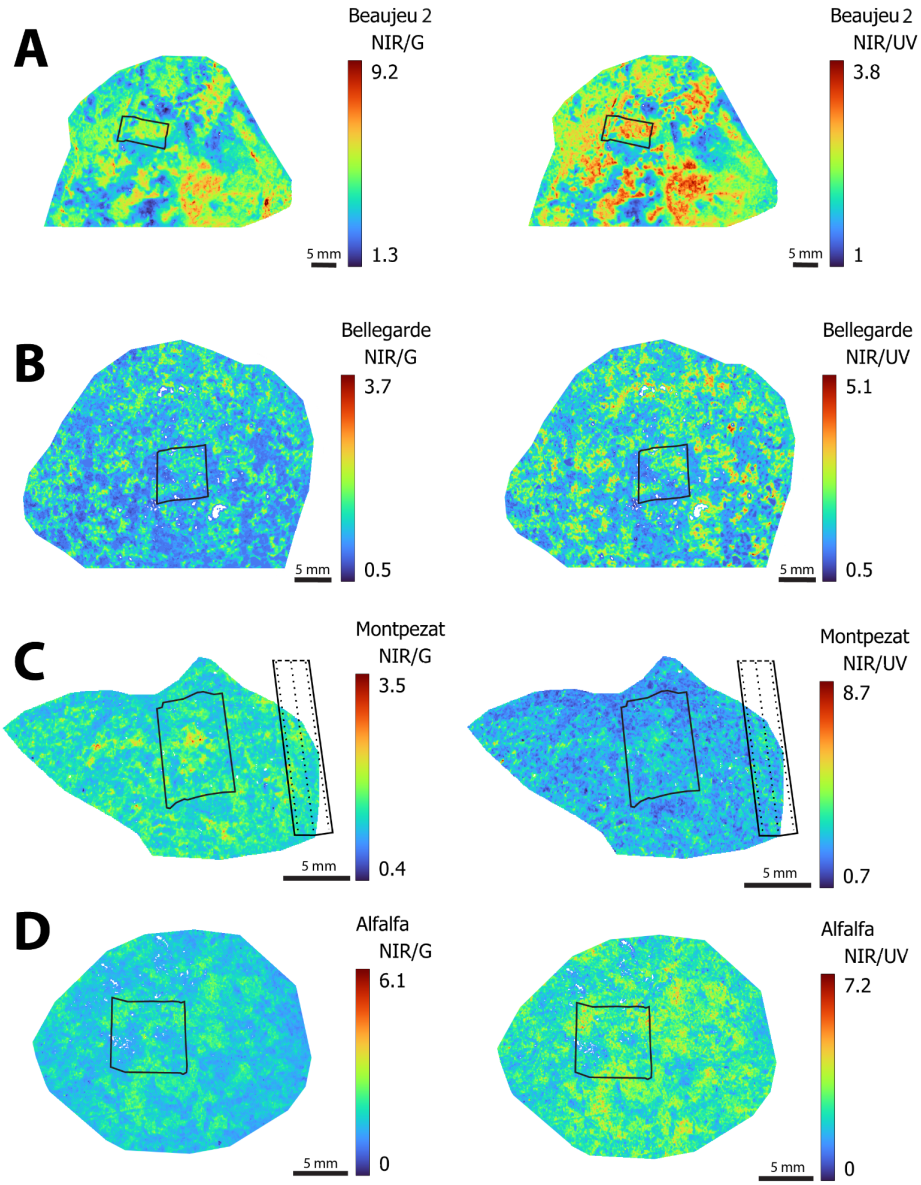


**Figure S4.** PIXL MCC color stack ratio images of Máaz fm targets with scan locations (Table S1). Images were cropped to remove abrasion fines and vignetting. A. Natural surface *Beaujeu 2* ratio images of near infared to green ratio (NIR/G) and near infared to ultraviolet (NIR/UV) (PCCR0138_0679289188_000MSA_N005181205282253200710LUD01). B. Abraded target *Bellegarde* ratio images of NIR/G and NIR/UV (PCCR0187_0683483390_000MSA_N007000006992743100050LUD01). C. Abraded target *Montpezat* ratio images of NIR/G and NIR/UV with 3-line (*Montpezat 1*) and map (*Montpezat 2*) scan locations (PCCR0348_0697993842_000MSA_N009298212353587900030LUD01). The *Montpezat* scan is 30 mm long and extends beyond the image. The D. Abraded target *Alfalfa* ratio images of NIR/G and NIR/UV (PCCR0369_0699769650_000VIS_N000010813074483400030LUD02).

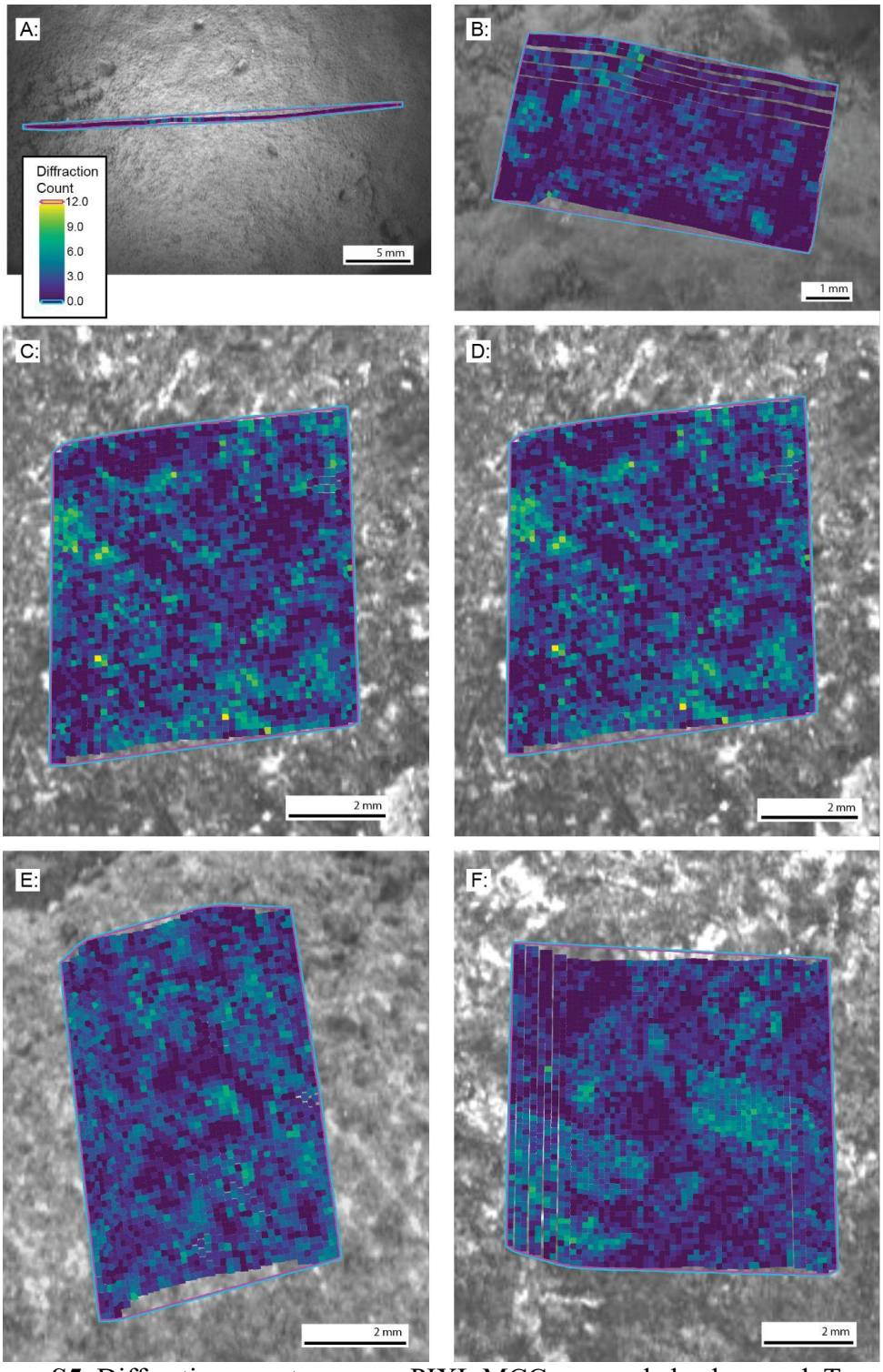


**Figure S5.** Diffraction count maps on PIXL MCC grayscale background. Targets include natural surfaces A: *Naltsos* and B: *Beaujeu 2* and abrasions C: *Guillaumes*; D: *Bellegarde*; E: *Montpezat*; F: *Alfalfa*.

*Montpezat (Sols 347-348)*
The abrasion at the Rimplas outcrop produced an uneven surface with irregular cracks and abundant abrasion fines covering much of the surface. Cleared areas of the abrasion surface are dark gray with red patches. In order of decreasing modal abundance, PIXL scans indicate the presence of augite, plagioclase feldspar, olivine/Fe-silicate, FeTi-oxide, KSi-rich mesostasis, and Ca-phosphate. FeCl-rich alteration surrounds and is clearly replacing olivine in the central part of the map scan*Montpezat* has this highest Mg# (35.2, Table 1) of the Máaz formation PIXL targets with the most magnesian pyroxenes and olivines (Figure 3; Table S6).

*Alfalfa (Sol 369)*
Abrasion of dark-toned ventifacted surface of the Sid outcrop exposed a crystal-rich porphyritic fabric at *Alfalfa*. Relatively large laths (~5 mm) of plagioclase feldspar are surrounded by a KSi-rich groundmass. Other minerals identified include Fe-rich augite, olivine, and FeTi-oxide that are present in equal proportions. Accessory Ca-phosphate (likely apatite) is also identified.

**Tabulated PIXL Results**
***Bulk analyses***
Bulk XRF analyses determined by the separate PIXL detectors are presented in Table S3. Raw bulk sum composition for Maaz PIXL targets that uses the lower concentration of the two detectors are presented in Table S4. Final igneous compositions determined for low salt regions (Figure 3, main text) are presented in Table 1 of the main text.

**Table S3. Máaz Bulk XRF analyses determined by the two PIXL detectors**
**Separate excel spreadsheet*

**Table S4 Máaz fm PIXL bulk sum compositions**

| | ***Guillaumes Bulk*** | | ***Guillaumes Low salt*** | | ***Bellegarde Bulk*** | | ***Bellegarde Low salt[2]*** | | ***Montpezat* Combined *Bulk*** | | ***Montpezat* Combined *Low salt[3]*** | | ***Alfalfa Bulk*** | | ***Alfalfa Low salt*** | |
|---|---|---|---|---|---|---|---|---|---|---|---|---|---|---|---|---|
| *Sol* | *167* | | *167* | | *187* | | *187* | | *347-348* | | *347-348* | | *369* | | *369* | |
| *#PMC* | 2809 | | *1531* | | 2809 | | *2411* | | *2700* | | *2553* | | 3249 | | *2782* | |
| | wt% | +/- | wt% | +/- | wt% | +/- | wt% | +/- | wt% | +/- | wt% | +/- | wt% | +/- | wt% | +/- |
| $Na_2O$ | 5.8 | 0.6 | 4.9 | 0.6 | 4.8 | 0.3 | 4.9 | 0.3 | 3.7 | 0.8 | 3.7 | 0.8 | 5.2 | 0.6 | 5.3 | 0.6 |
| MgO | 2.6 | 0.6 | 2.4 | 0.7 | 2.2 | 0.6 | 1.9 | 0.6 | 5.9 | 0.3 | 5.7 | 0.3 | 0.8 | 0.3 | 0.7 | 0.3 |
| $Al_2O_3$ | 7.7 | 0.4 | 8.2 | 0.4 | 7.0 | 0.4 | 7.6 | 0.4 | 5.8 | 0.3 | 6.1 | 0.3 | 11.4 | 0.6 | 12.1 | 0.6 |
| $SiO_2$ | 38.9 | 2.0 | 42.2 | 2.1 | 44.4 | 2.2 | 46.7 | 2.3 | 44.1 | 2.2 | 45.1 | 2.3 | 55.5 | 2.8 | 57.4 | 2.9 |
| $P_2O_5$ | 1.7 | 0.6 | 1.8 | 0.6 | 2.8 | 0.7 | 3.0 | 0.6 | 1.3 | 0.5 | 1.3 | 0.5 | 1.2 | 0.4 | 1.3 | 0.4 |
| $SO_3$ | 2.8 | 0.6 | 1.2 | 0.4 | 3.3 | 0.6 | 1.5 | 0.4 | 0.8 | 0.3 | 0.7 | 0.2 | 1.1 | 0.3 | 0.7 | 0.2 |
| Cl | 3.5 | 0.5 | 1.9 | 0.5 | 1.5 | 0.4 | 1.3 | 0.4 | 1.0 | 0.3 | 0.8 | 0.3 | 2.1 | 0.5 | 1.5 | 0.4 |
| $K_2O$ | 0.8 | 0.3 | 0.8 | 0.3 | 1.1 | 0.3 | 1.2 | 0.4 | 0.7 | 0.2 | 0.8 | 0.3 | 1.9 | 0.5 | 1.9 | 0.5 |
| CaO | 7.8 | 0.4 | 7.8 | 0.4 | 7.8 | 0.4 | 8.0 | 0.4 | 8.9 | 0.4 | 9.7 | 0.5 | 4.7 | 0.3 | 4.6 | 0.3 |
| $TiO_2$ | 1.5 | 0.5 | 1.7 | 0.5 | 2.5 | 0.7 | 2.7 | 0.7 | 1.4 | 0.5 | 1.7 | 0.5 | 1.0 | 0.4 | 0.9 | 0.4 |
| $Cr_2O_3$ | 0.02 | 0.05 | 0.01 | 0.02 | 0.01 | 0.03 | 0.01 | 0.03 | 0.09 | 0.11 | 0.09 | 0.11 | 0.0 | 0.0 | 0.0 | 0.0 |
| MnO | 0.5 | 0.2 | 0.4 | 0.2 | 0.4 | 0.2 | 0.4 | 0.2 | 0.5 | 0.2 | 0.5 | 0.2 | 0.3 | 0.2 | 0.3 | 0.2 |
| $FeO_T$ | 19.0 | 0.9 | 19.5 | 1.0 | 23.6 | 1.2 | 22.1 | 1.1 | 21.0 | 1.0 | 18.7 | 0.9 | 12.4 | 0.6 | 10.6 | 0.5 |
| Sr | 0.07 | 0.03 | 0.07 | 0.03 | 0.04 | 0.03 | 0.04 | 0.03 | 0.03 | 0.03 | 0.03 | 0.03 | 0.07 | 0.04 | 0.03 | 0.03 |
| **SUM** | 92.6 | | 92.9 | | 101.5 | | 101.2 | | 95.1 | | 94.7 | | 97.4 | | 97.3 | |
| **Mg#** | 19.7 | | 17.7 | | 14.1 | | 13.6 | | 33.3 | | 35.2 | | 9.8 | | 10.4 | |

Bulk sums were determined using the lower of the concentration of each element determined by sum spectra from x-ray detector A or B to limit effects of x-ray diffraction (Table S3). [1] *Guillaumes-Low salt* was calculated for PMCs where <2 wt% $SO_3$, <4 wt% Cl (1531 PMCs). [2] *Bellegarde-Low salt* was calculated for PMCs where <4.85 wt% $SO_3$, <3 wt% Cl (2411 PMCs). [3] *Montpezat Combined Bulk* is the bulk sum of sol 347 line and sol 348 map scans. *Montpezat Combined-Low salt* was determined as the weighted average of (1) low salt regions (<1.5 wt% $SO_3$, <1.5 wt% Cl; 2171 PMCs) and (2) regions of Fe-silicate alteration in spatial association with olivine, where Cl was set to 1 wt% (382 PMCs). [4] *Alfalfa-low salt* was determined as the weighted average of (1) low salt regions <2 wt% $SO_3$, <4 wt% Cl; 2610 PMCs) and (2) regions of Fe-silicate alteration, where Cl was set to 1 wt% (188 PMCs).

Ideal mineral endmember compositions and stoichiometric ratios are presented in Table S5. A summary of the mineral compositions is presented in Table 2 of the main text.

**Table S5. Máaz fm mineral endmember compositions determined by PIXL**

**Separate Excel sheet*

**Mitigating surface topography and diffraction peak overlap**

For mapping oxide abundances, the effects of rock surface roughness and diffraction peak overlaps with elemental fluorescence peaks were individually corrected for every PMC. Corrections were implemented using PIXLISE expressions. The expressions for these corrections and derived oxide values are referred to collectively as "Best v.3.2." Corrected oxide values are presented in Table S6. Anomalous PIXL spots, where differences in livetime durations between the two detectors are greater than 0.2 s are omitted from Table S6.

**Table S6. XRF concentrations for all Máaz fm PIXL spots corrected for topography and diffraction**

**Separate Excel sheet*

PIXL elemental quantifications are calibrated for flat surfaces oriented perpendicularly to X-ray source. PIXL's two X-ray detectors observe equally intense diffraction peaks and peak backgrounds from such surfaces, and resultant spectra can be summed for quantification. However, surfaces that dip toward one of the PIXL detectors and away from the other produce summed spectra less intense than those produced from flat surfaces. Oxide abundances estimated from combined spectra collected from rough targets therefore underestimate actual abundances, on average. In contrast, diffraction peaks from coarsely crystalline minerals that overlap fluorescence peaks produce systematically overestimated abundances for the associated oxide.

Briefly, these effects were estimated and corrected by using oxide abundances estimated from spectra from each detector separately and from comparisons between the raw spectra. The orientation of the local rock surface was first estimated using an approximate method from the difference between spectra collected by the two detectors. From this estimated orientation, the difference in fluorescence peak intensities in each detector was predicted for each quantified oxide and compared with the actual difference observed. If the predicted and observed intensity differences were similar (within a Poisson-distributed detector counting error), then the fluorescence peak was assumed to be free of diffraction overlap. In this case, oxide abundances estimated from each detector were averaged and corrected for the estimated orientation. If the intensity from one detector was greater than predicted by surface orientation, then the oxide abundance was estimated from the detector not affected by diffraction overlap, corrected for the estimated orientation.

The following derivation demonstrates the basis for these corrections as well as the specific relationships used to perform them. Start with the following result (Eq. 1) from Geil and Thorne (2014) describing how the observed spectral intensity of X-rays from energy $E_1$ to $E_2$ varies with target surface orientation relative to the x-ray source measured in the plane of the source-target-detector, $\varphi$, the angular separation between source and detector, $\theta$, (Figure S6) and

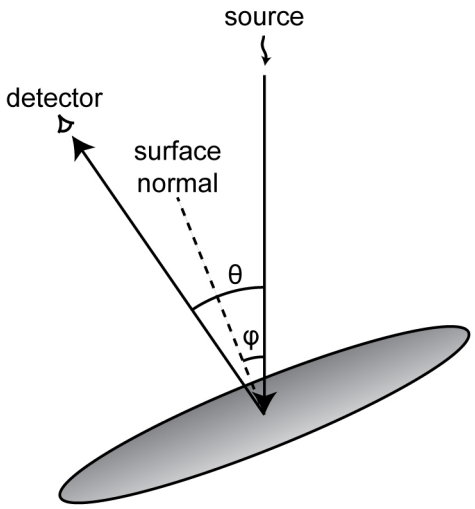


**Figure S6.** Geometric parameters describing source—target surface—detector system. $\theta$ measures the angular separation from the x-ray source to the detector; $\varphi$ measures the angular separation from the source to the target surface normal vector projected onto the plane containing the detector, source, and target point.

the effective ratio of extinction coefficients for characteristic radiation leaving the target to that of the exciting radiation entering the target, $\mu_{out}(E_1, E_2)/\mu_{in}(E_1, E_2)$.

$$I(\varphi, E_1, E_2) = \begin{cases} \frac{K(E_1,E_2)}{1+\frac{\mu_{out}(E_1,E_2)}{\mu_{in}(E_1,E_2)}(\cos\theta+\tan\varphi\,\sin\theta)^{-1}} & |\varphi-\theta|\leq 90° \\ 0 & |\varphi-\theta|>90° \end{cases} \quad (1)$$

Note that $K(E_1, E_2)$, $\mu_{out}(E_1, E_2)$, and $\mu_{in}(E_1, E_2)$ depend on the local target composition and will therefore typically vary from PMC to PMC. However, for an individual measurement spot and a given range of energies observed, they are effectively constants. For readability, we will not write any terms as explicit functions of the energy range observed from this point forward. Also, note that, because exciting X-rays have energy at least equal to that of the outgoing X-rays, $\mu_{out}/\mu_{in} \geq 1$.

PIXL has two detectors arranged symmetrically around the X-ray source in the same plane as the measurement spot, i.e. $\theta = \pm\varphi_0$, with $\varphi_0 = 20°$. Detectors A and B observe intensities described by Eqs. 2 and 3, respectively.

$$I_A = \frac{K}{1+\frac{\mu_{out}}{\mu_{in}}(\cos\varphi_0+\tan\varphi\,\sin\varphi_0)^{-1}} \quad (2)$$

$$I_B = \frac{K}{1+\frac{\mu_{out}}{\mu_{in}}(\cos\varphi_0-\tan\varphi\,\sin\varphi_0)^{-1}} \quad (3)$$

We want to understand how intensities measured at an arbitrary observation angle can be related to the intensities that would be observed on the same target oriented perpendicularly to the X-ray source (i.e., calibration conditions). To do that, we will examine how the difference and sum of

the two detector intensities vary (Eqs. 4, 5) assuming that the surface is visible to both detectors ($-90° + \varphi_0 \leq \varphi \leq 90° - \varphi_0$).

$$I_A - I_B = K\left(\frac{\cos\varphi_0+\tan\varphi\sin\varphi_0}{\cos\varphi_0+\tan\varphi\sin\varphi_0+\frac{\mu_{out}}{\mu_{in}}} - \frac{\cos\varphi_0-\tan\varphi\sin\varphi_0}{\cos\varphi_0-\tan\varphi\sin\varphi_0+\frac{\mu_{out}}{\mu_{in}}}\right) \quad (4)$$

$$I_A + I_B = K\left(\frac{\cos\varphi_0+\tan\varphi\sin\varphi_0}{\cos\varphi_0+\tan\varphi\sin\varphi_0+\frac{\mu_{out}}{\mu_{in}}} + \frac{\cos\varphi_0-\tan\varphi\sin\varphi_0}{\cos\varphi_0-\tan\varphi\sin\varphi_0+\frac{\mu_{out}}{\mu_{in}}}\right) \quad (5)$$

It is useful to define a dimensionless attenuation ratio, $x$, and a dimensionless tilting factor, $\varepsilon_0$, by Equations 6 and 7, respectively.

$$x = \frac{\mu_{out}}{\mu_{in}\cos\varphi_0} \quad (6)$$

$$\varepsilon_0 = \tan\varphi_0\tan\varphi \quad (7)$$

Equations 4 and 5 can be rewritten as Equations 8 and 9 using these new terms.

$$I_A - I_B = 2K\frac{x\varepsilon_0}{x^2+2x+1-\varepsilon_0^2} \quad (8)$$

$$I_A + I_B = 2K\frac{x+1-\varepsilon_0^2}{x^2+2x+1-\varepsilon_0^2} \quad (9)$$

Thus, the relative difference in observed intensities is:

$$\varepsilon = \frac{I_A-I_B}{I_A+I_B} = \frac{x\varepsilon_0}{x+1-\varepsilon_0^2}. \quad (10)$$

This expression is convenient because an observable, $\varepsilon$, is written in terms that depend individually only on target spot properties and the energy range observed ($x$) or on the surface orientation ($\varepsilon_0$).

Finally, note that $\varepsilon_0 = 0$ when $\varphi = 0$, so the sum of intensities observed by detectors A and B from a horizontal surface is described by Equation 9.

$$\hat{I}_A + \hat{I}_B = \frac{2K}{x+1} \quad (11)$$

PIQUANT was calibrated for PIXL measurements on horizontal surfaces, so we would ultimately like to be able to estimate this sum from observed spectra. This requires estimating a correction factor, or the ratio of the summed intensities from a horizontal surface to the actual observed sum. This correction factor can be provisionally written as

$$\beta = \frac{\hat{I}_A+\hat{I}_B}{I_A+I_B} = \frac{(x+1)^2-\varepsilon_0^2}{(x+1)^2-(x+1)\varepsilon_0^2}. \quad (12)$$

Direct use of this form of the correction factor would require knowledge of the surface topography, $\varepsilon_0$, and X-ray attenuation properties of the target, $x$, neither of which are directly observable. However, Equation 12 can be rewritten in terms of Equation 10, leading to the more useful form:

$$\beta = \frac{1-\varepsilon^2}{1-\varepsilon_0\varepsilon}. \quad (13)$$

$\varepsilon$ is calculable from observed intensities (Eq. 10), so if the inclination of the surface can also be estimated from portions of the detector spectra, then Equation 13 can be used to correct for topographic effects.

Equation 10 implies that $|\varepsilon|$ increases to $|\varepsilon_0|$ asymptotically with increasing $x$. Thus, $|\varepsilon| \leq |\varepsilon_0|$, with equality only approached in special cases of matrix composition or highly inclined surfaces. This means that surface inclinations cannot generally be estimated directly from arbitrarily chosen relative intensity differences. Instead, they need to be selected from cases for which $x$ can be estimated reasonably.

We use the special case of backscattered Bremsstrahlung X-rays in the energy range 9.2–12.4 keV. This range was chosen to avoid major fluorescence and pileup peaks commonly observed in PIXL spectra, but subranges can be selected to avoid such features as well as large diffraction peaks. Most of these photons are therefore produced by scattering of incident photons having identical (Rayleigh scattering) or very similar energies (Compton scattering), and nearly all from within the same energy range. In that case, $\mu_{out} \approx \mu_{in}$, so $x' \approx 1/\cos\varphi_0$ (from Eq. 6). $\varepsilon_0$ is therefore related to $\varepsilon' = (I_A' - I_B')/(I_A' + I_B')$ observed for 9.2–12.4 keV by

$$\varepsilon' = \frac{x'\varepsilon_0}{x+1-\varepsilon_0^2} = \frac{\varepsilon_0}{1+(1-\varepsilon_0^2)\cos\varphi_0}. \quad (14)$$

Collecting terms with $\varepsilon_0$ shows that this is equivalent to a quadratic equation in $\varepsilon_0$ (Eq. 15).

$$(\varepsilon'\cos\varphi_0)\varepsilon_0^2 + \varepsilon_0 - \varepsilon'(1+\cos\varphi_0) = 0 \quad (15)$$

The solution allowing estimation of the surface orientation thus follows from the quadratic formula, accounting for the case where $\varepsilon' = 0$:

$$\varepsilon_0 = \begin{cases} \frac{-1+\sqrt{1+4\varepsilon'^2\cos\varphi_0(1+\cos\varphi_0)}}{2\varepsilon'\cos\varphi_0} & \varepsilon' \neq 0 \\ 0 & \varepsilon' = 0 \end{cases}. \quad (16)$$

Finally, from the definition of $\varepsilon_0$ (Eq. 7),

$$\varphi = \begin{cases} \tan^{-1}\left(\frac{-1+\sqrt{1+4\varepsilon'^2\cos\varphi_0(1+\cos\varphi_0)}}{2\varepsilon'\sin\varphi_0}\right) & \varepsilon' \neq 0 \\ 0 & \varepsilon' = 0 \end{cases}. \quad (17)$$

With $\varepsilon_0$ estimated, we can compare the potential range of $\varepsilon$ to those observed for spectral regions that include characteristic fluorescence peaks. If all observed X-rays were generated by fluorescence and isotropic scattering, then $\varepsilon$ will be related to $\varepsilon_0$ by some unknown $x$ (Eq. 10). However, because $\mu_{out}/\mu_{in} \geq 1$, we know that $1/\cos\varphi_0 \leq x < \infty$. Moreover, $\varepsilon \to \varepsilon_0$ as $x \to \infty$; this implies that

$$\frac{\varepsilon_0}{1+(1-\varepsilon_0^2)\cos\varphi_0} \leq \varepsilon < \varepsilon_0 \quad (18)$$

for $\varepsilon_0 \geq 0$, and

$$\varepsilon_0 < \varepsilon \leq \frac{\varepsilon_0}{1+(1-\varepsilon_0^2)\cos\varphi_0} \quad (19)$$

for $\varepsilon < 0$. Thus, if $\varepsilon$ is not in this range for PIXL spectra in any given energy range, we infer that one of the spectra from detectors A and B includes a diffraction peak in that range (Figure S7A).

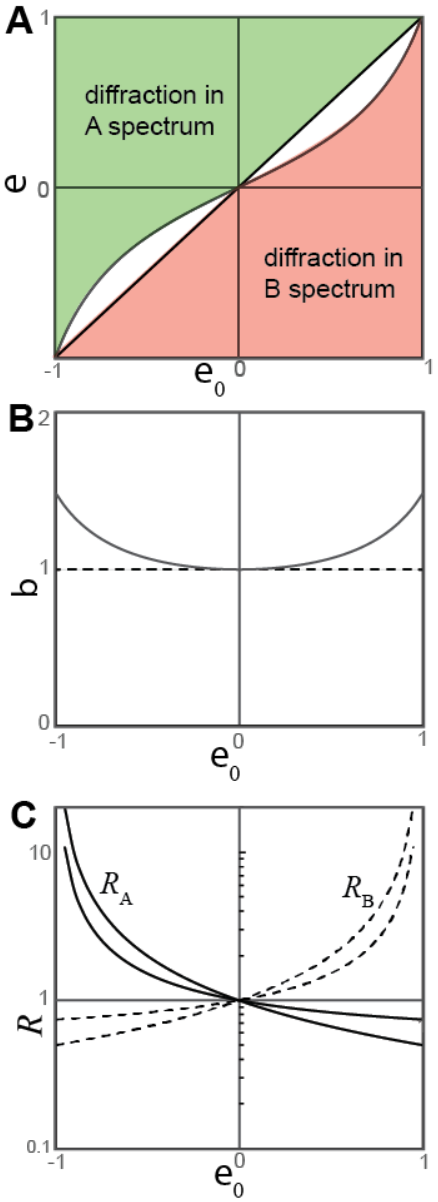


**Figure S7.** Diffraction detection and correction factors for geometric and diffraction effects. A: Diffraction effects are inferred when the relative intensity difference between detectors A and B, $\varepsilon$, is greater than (green) or less than (orange) ranges allowed by the estimated target orientation, $\varepsilon_0$. B: Range of geometric correction factors (Eq. 20) for oxides with no detected overlapping diffraction peaks. Corrected abundances differ most from uncorrected abundances for highly inclined surfaces ($\varepsilon_0$ close to ±1) with $|\varepsilon| < |\varepsilon_0|$ (solid line; curved boundaries in A). There is no correction with $\varepsilon \approx \varepsilon_0$ (dashed line). C: Range of single-detector correction factors for oxides with overlapping diffraction peaks in detector A (dashed lines) or detector B (solid lines). Correction factors differ most from 1 for highly inclined surfaces with with $|\varepsilon| < |\varepsilon_0|$ (curved boundaries in A).

For correcting diffraction effects on estimated elemental abundances, we check for diffraction peaks overlapping the tallest expected characteristic fluorescence peak for each element (e.g., Si $K_\alpha$ for Si, Fe $K_{\alpha 1,2}$ for Fe, etc.). If no diffraction is detected, we estimate the topographically corrected elemental abundance by scaling the average of the PIQUANT estimates from each detector, $C_A$ and $C_B$, by the correction factor, $\beta$ (Eq. 13; Figure S7B):

$$C_{corrected} = \beta \cdot \frac{C_A + C_B}{2}. \quad (20)$$

Alternatively, if diffraction is detected in one spectrum, we use the PIQUANT estimate from the other spectrum and $\varepsilon$ estimated by interpolation from nearby fluorescence peaks to perform the correction (Figure S7C):

$$C_{corrected} = \begin{Bmatrix} R_B C_B & diffraction\ in\ A\ spectrum \\ R_A C_A & diffraction\ in\ B\ spectrum \end{Bmatrix}, \quad (21)$$

where

$$R_B = \frac{1+\varepsilon}{1-\varepsilon_0 \varepsilon} \quad (22)$$

and

$$R_A = \frac{1-\varepsilon}{1-\varepsilon_0 \varepsilon}. \quad (23)$$

These adjustments approximate the relationship between fluorescence peak intensity and elemental abundance as locally linear near the PIQUANT fit. They do not adjust for matrix effects associated with the corrected elements, and are thus likely to be most accurate for corrections involving less abundant elements or relatively small changes to major elements.

An example of the complete analytical workflow applied to NiO abundances in the Beaujeu 2 map scan is provided in Figure S8.

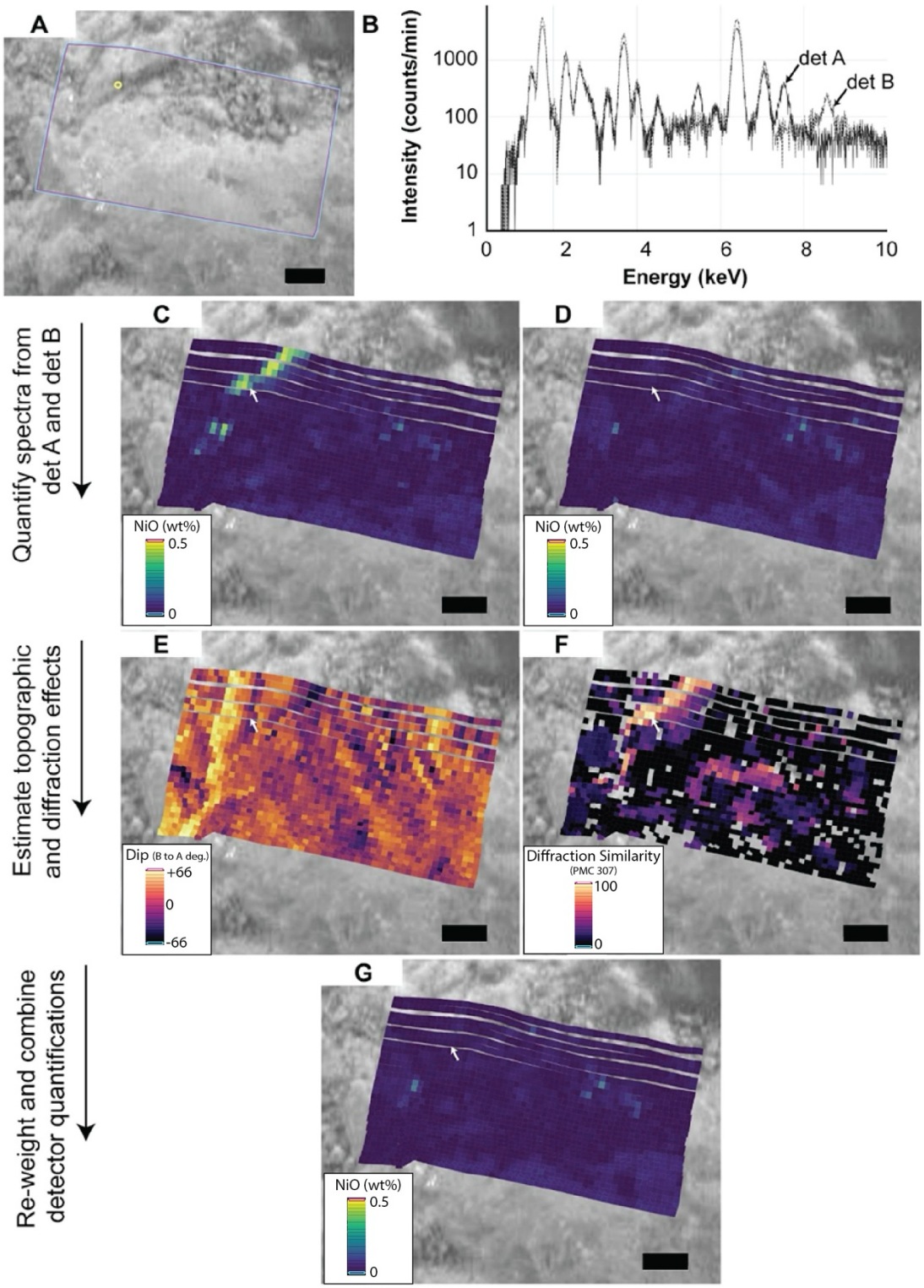


**Figure S8.** Diffraction and topographic corrections applied to NiO abundances in the Beaujeu 2 map scan. A: Map footprint (box) with location of example spectra in (B) shown with yellow circle. Scale bar = 1 mm. B: X-ray spectra from detectors A (solid line) and B (dashed line) from measurement spot indicated in (A). Intensities observed by

det B are systematically greater than those observed by det A indicating that the local target surface dipped toward det B. Anisotropic diffraction peaks appear as peaks observed in only one detector, including one at ~7.5 keV in det A's spectrum which overlaps the locations of the Ni $K_{\alpha 1,2}$ characteristic fluorescence peaks. Here and in following panels, white arrows indicate location of example spectra. C, D: PIQUANT-quantified NiO abundances (wt%) from the det A spectrum and det B spectrum, respectively. Note that the quantification from det A shows a large region contiguous with the sample spot having apparent NiO abundances from 0.2-0.5 wt%. Because det B's spectra were not affected by the diffraction peak shown in (B), its map does not show the same Ni-enriched region. E: Estimated local surface dip (°) from det B to det A (right to left). F: Diffraction similarity (%) with spectra from (B) showing that apparent Ni enrichment is associated with diffraction from one or two large monocrystalline grains. G: NiO abundances (wt%) corrected for geometric and diffraction effects.

**Modal analysis**

Once corrected for the effects of diffraction and topography as described above, minerals were identified according to the stoichiometric ratios and threshold values in Table S7. Mineral phase maps for modal analysis are presented in Figure S9.

**Table S7. Stoichiometric molar ratios and element thresholds to identify igneous minerals for modal analysis**

| PIXL Target | Sol | Pyroxene $\frac{Fe + Mg + Ca}{Si} = 1 \pm 0.1$ | Olivine $\frac{Fe+Mg}{Si} = 2 \pm 0.4$ | Feldspar $\frac{Na + K + Ca}{Si + Al} = 0.25 \pm 0.025$ | Oxides $\frac{Fe}{Si} => 5$ *OR* $TiO_2 > 5$ *OR* $Cr_2O_3 > 5$ *wt%* | K-rich groundmass |
|---|---|---|---|---|---|---|
| | | **Additional parameters** | | | | |
| *Beaujeu 2* | 139 | $SO_3 < 3, Cl < 3$ *wt%* | $SO_3 < 3, Cl < 3$ *wt%* $TiO_2 < 1, Cr_2O_3 < 1$ *wt%* | $SO_3 < 3, Cl < 3$ *wt%* $TiO_2 < 1, Cr_2O_3 < 1$ *wt%* $FeO < 5$ *wt%* | $SO_3 < 5, Cl < 5$ *wt%* | $K_2O > 2$ *wt%*, excluding stoichiometric plagioclase previously defined |
| *Guillaumes* | 167 | $SO_3 < 2, Cl < 4$ *wt%* | $SO_3 < 2, Cl < 4$ *wt%* $TiO_2 < 1, Cr_2O_3 < 1$ *wt%* | $SO_3 < 2, Cl < 4$ *wt%* $TiO_2 < 1, Cr_2O_3 < 1$ *wt%* $FeO < 5$ *wt%* | $SO_3 < 2, Cl < 4$ *wt%* | |
| *Bellegarde* | 187 | $SO_3 < 4.85, Cl < 3$ *wt%* | $SO_3 < 4.85, Cl < 3$ *wt%* $TiO_2 < 1, Cr_2O_3 < 1$ *wt%* | $SO_3 < 4.85, Cl < 3$ *wt%* $TiO_2 < 1, Cr_2O_3 < 1$ *wt%* $FeO < 5$ *wt%* | $SO_3 < 2, Cl < 2$ *wt%* | |
| *Montpezat 2* | 349 | $SO_3 < 1.5, Cl < 1.5$ *wt%* | $SO_3 < 1.5, Cl < 1.5$ *wt%* $TiO_2 < 1, Cr_2O_3 < 1$ *wt%* | $SO_3 < 1.5, Cl < 1.5$ *wt%* $TiO_2 < 1, Cr_2O_3 < 1$ *wt%* $FeO < 5$ *wt%* | $SO_3 < 1, Cl < 1.5$ *wt%* | |
| *Alfalfa* | 369 | $SO_3 < 2, Cl < 4$ *wt%* | $SO_3 < 2, Cl < 4$ *wt%* $TiO_2 < 1, Cr_2O_3 < 1$ *wt%* | $SO_3 < 2, Cl < 4$ *wt%* $TiO_2 < 1, Cr_2O_3 < 1$ *wt%* $FeO < 5$ *wt%* | $SO_3 < 2, Cl < 6$ *wt%* | |

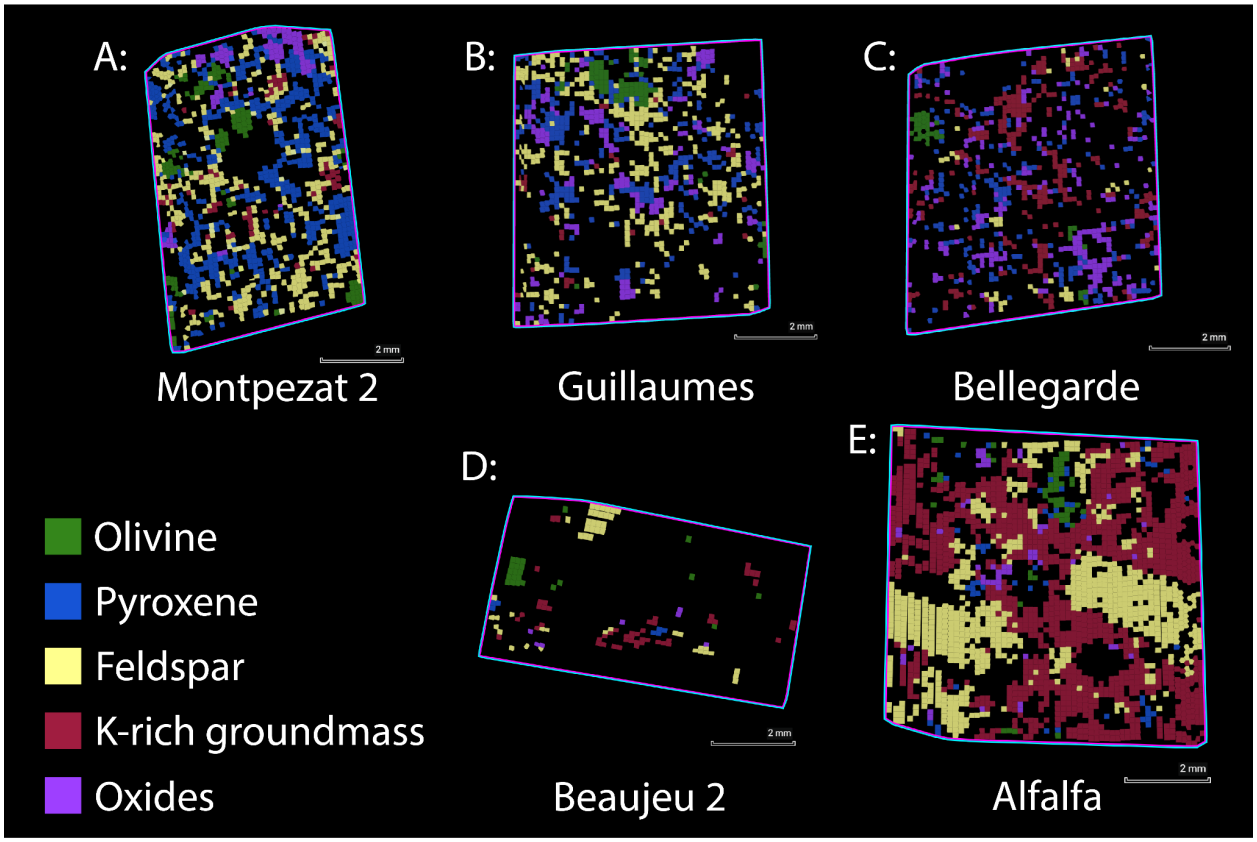


**Figure S9.** Igneous mineral ROI maps for Máaz fm. abraded targets for determining modal proportions (Table 3). ROIs were determined on the basis of stoichiometric ratios and thresholds in Table S6. A: *Montpezat 2*; B: *Guillaumes*; C: *Bellegarde*; D: *Beaujeu 2*; E: *Alfalfa*.

## Comparison with other M2020 instruments

### *Comparison with SuperCam results*

SuperCam performed multiple LIBS point analyses on many outcrops in Máaz formation, among which only three abrasion patches (*Guillaumes*, *Bellegarde*, *Alfalfa*) were (*36*), for a total of 61 points on abraded surfaces. SuperCam performs grid or line scans of LIBS spot analyses; typical SuperCam observations include 3 x 3 grid or 10 x 1 line. Each LIBS spot ranges from 0.17 mm (170 µm) when the rover is at 1.5 m away from the target to 0.37 mm (370 µm) at 5.5 m away from the target. After a rigorous screening process based on stoichiometry, points representing pristine primary minerals are used to estimate the mineral chemistry and averaged to obtain the bulk rock chemistry of individual outcrops (*36*).

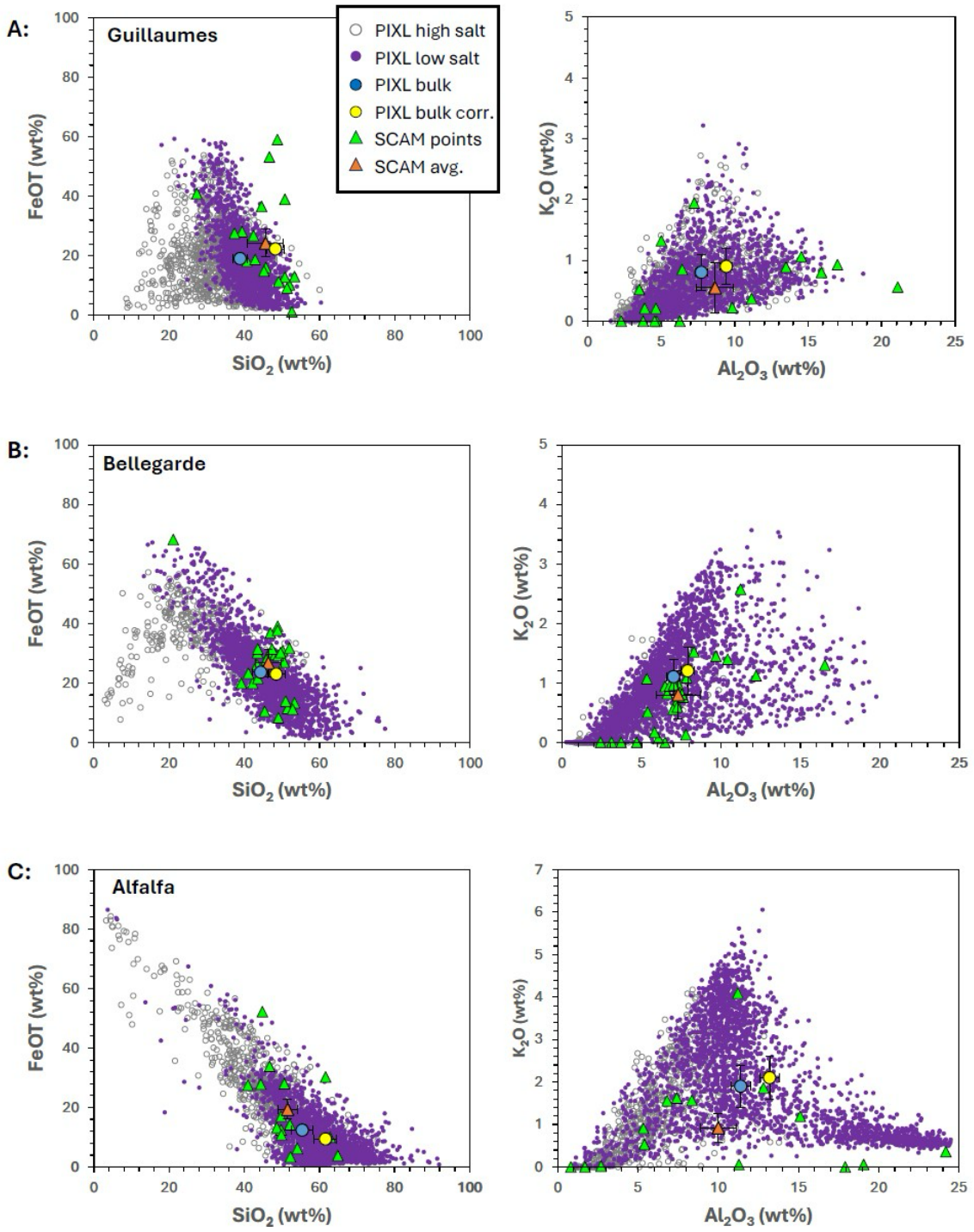


**Figure S10.** Binary plots comparing PIXL and SCAM results (*36*) for the three corresponding Maaz fm. abraded targets, listed in order of decreasing Mg#. The SCAM results only include points that have relatively high total abundances, signifying low concentrations of S, Cl, $CO_3$, or OH. PIXL low salt and high salt (including FeCl-rich) PMCs are defined in Table S4 caption and ROIs are presented in Figure 3, main text. Error bars are visible when they are larger than the symbols. PIXL error bars on the bulk sum are for the PIQUANT fit. SCAM errors are standard deviation of average. *Guillaumes* A: FeO vs. $SiO_2$ and B: $K_2O$ vs. $Al_2O_3$; *Bellegarde* C: FeO vs. $SiO_2$ and D: $K_2O$ vs. $Al_2O_3$; *Alfalfa* E: FeO vs. $SiO_2$ and F: $K_2O$ vs. $Al_2O_3$.

At the closest distance, one SuperCam LIBS spot is comparable to that of one PIXL XRF spot (~125 μm). We compare SuperCam and PIXL results on the same abrasion patches in Figure S10. For *Bellegarde* and *Guillaumes*, bulk rock chemistries by PIXL (low-salt) agree with those by SuperCAM within uncertainties. However, PIXL bulk rock chemistry (low-salt) of *Alfalfa* is noticeably different from that of SuperCam outside uncertainties. This comparison reflects how different instrument measurement schemes (map scan versus grid of points) can yield different results depending on the rock texture. *Alfalfa* exhibits a more heterogeneous texture of large feldspar grains embedded in a fine grained matrix whereas *Guillaumes* and *Bellegarde* are mostly fine grained. The point analyses by SuperCam could have sampled less feldspar in *Alfalfa* than PIXL, an interpretation that is supported as SuperCam bulk chemistry for *Alfalfa* is lower in $K_2O$ and $Al_2O_3$ contents in PIXL bulk chemistry (Figure S10).

***Comparison with SHERLOC results***

SHERLOC (Scanning Habitable Environments with Raman and Lumiscence for Organics and Chemicals) couples microscopic co-boresighted ACI images of high resolution (10.1 microm/pixl) with scans by a deep UV (DUV) laser to obtain spectra of Raman and fluorescence emissions of identified geologic targets of interest for identification of organics, chemicals, hydration features, and minerals (*42*, *61*). The DUV Raman spectral window is energetically separated from the fluorescence window and allows for separation of Raman and fluorescence spectral regions, ~800 to 4000 cm-1(~250-273 nm) and (~274 to 370 nm), respectively. The Raman window is used for identification of minerals, organics, and hydration features whereas the fluorescence window is applied for observations of organics (and in some cases, also REE's) (*47*, *61*). The diameter of the incident beam is ~100 μm and a depth of penetration of 100 - 200 μm (mineral matrix dependent) (*42*, *111*).

Three main types of scans are made: (1) survey scans covering with a resolution of 50, 144, or 200 microm. which include 1296 point array with lower laser power of 10-15 pulses per point (ppp); (2) High Dynamic Range (HDR) scans covering an area of ~7 x 7 $mm^2$, 780 microm. resolution, and which include 100 point arrays with medium power of 100 to 500 ppp; (3) detail scans covering an area of ~1 x 1 $mm^2$, 100 μm resolution, and which include 100 point arrays with a power of 500 ppp.

Initial preprocessing of SHERLOC data is made with open source software, Loupe (Uckert, 2023), which includes subtraction of dark spectrum from active spectrum (both are collected as part of each scan). This is followed by laser normalization and cosmic ray removal. Processed spectra are then compared with spectra from analogue laboratory instruments from Brassboard and MOBIUS of relevant reference materials (*42*, *61*, *62*).

*Alfalfa* relevant scans included a 15 ppp survey and a 500 ppp HDR scans (Figure S11). SHERLOC Raman spectra on the feldspars in *Alfalfa* were of two types similar to those seen in polymict breccia meteorite NWA 10922 (*112*). Those in the matrix with peak centers at 1030-1110 $cm^{-1}$, and a peak center of ~1076 cm-1 consistent with alkali feldspars. This was similar to the ACRONM observations of labradorite spectra, and the large sub-millimeter to ~ 5 mm light and bright, highly reflective, lath-like crystals with peak centers at 1010-1030 $cm^{-1}$ and a peak center of ~1030 cm-1 consistent with crystalline feldspar, and complementary to those observed with PIXL.

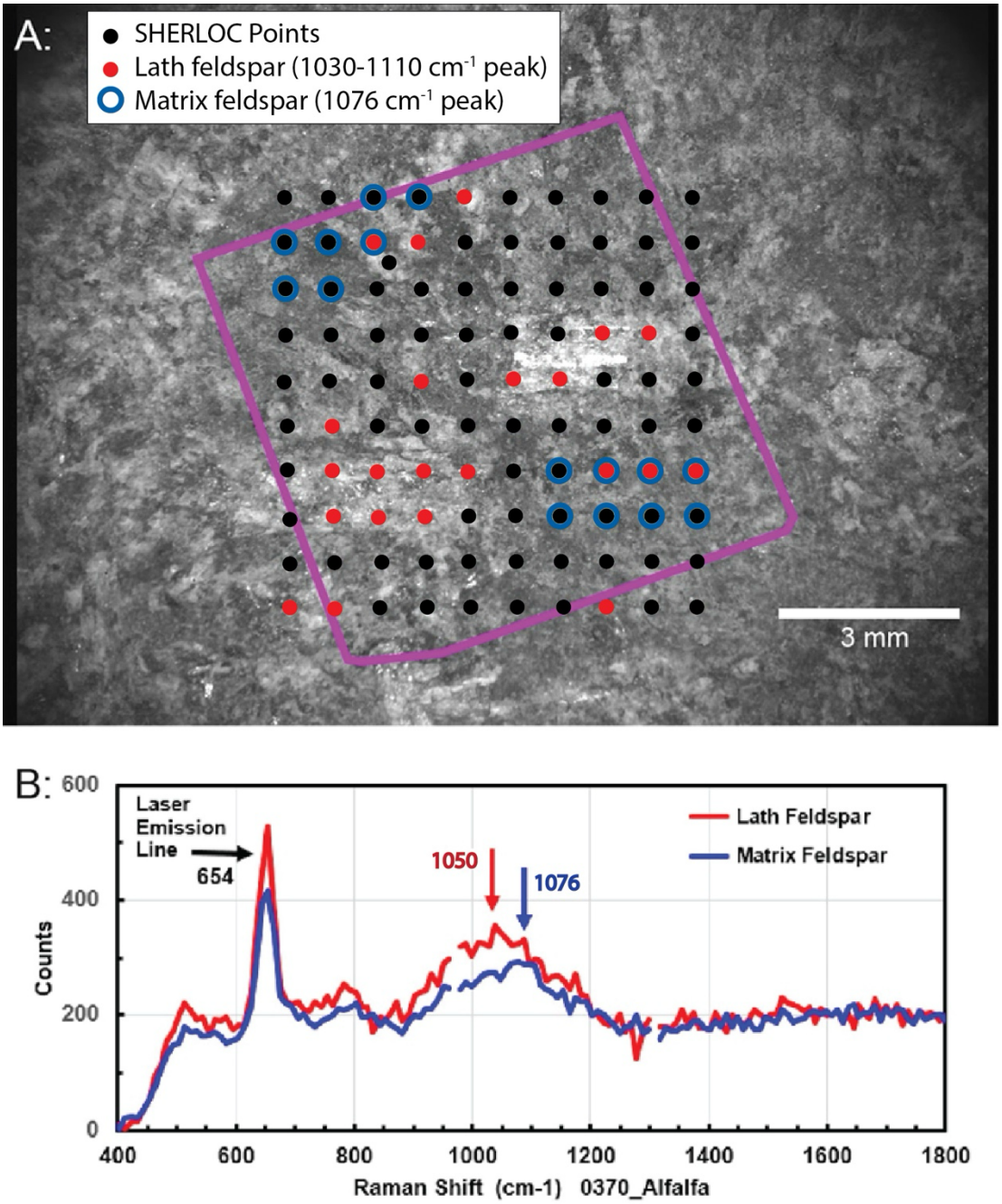


**Figure S11.** A: SHERLOC ACI image (SC3_0370_0699816377_617FDR_N0110108SRLC10600_0000LMJ01.IMG) of *Alfalfa* abrasion with Raman raster points and PIXL map outline (pink). B: Plot of counts vs. Raman shift ($cm^{-1}$) illustrating two types of feldspars identified in the *Alfalfa* scan: lath feldspar (1000 to 1050 $cm^{-1}$ peak) is consistent with sodic crystalline plagioclase and matrix feldspar (peak at 1030-1110 $cm^{-1}$), consistent fine grained alkali feldspar (*112*).

***Comparison with Mastcam-Z results***

Mastcam-Z (Mast Camera - Zoom; (*113*) is a pair of stereoscopic and multispectral cameras mounted on the *Perseverance* remote sensing mast. Mastcam-Z acquires multispectral images of the Jezero landscape, rocks, and abrasion patches through narrowband filters at 14 unique wavelengths across the visible /near-infrared (VNIR; 442-1022 nm), allowing detection of Fe-

bearing primary and secondary minerals (*60*). Mastcam-Z abrasion patch images typically have a resolution of 0.15-0.2 mm (150-200 μm) per pixel, so while the largest grains can often be resolved, spectra are most commonly mixtures of many Fe-bearing phases. For comparison, the PIXL MCC has a surface resolution of ~52 μm per pixel.

Máaz formation outcrops exhibit spectral signatures interred to be dominated by pyroxene, Fe-bearing feldspar, and hematite, which can be tied directly to igneous grains and altered matrix in abrasion patches (*35*). These spectral signatures vary with stratigraphy within Máaz. Hematite signatures weaken downsection, as they are strongest in the Cha'l member, common in Nataani, patchy in Roubion, patchy within abrasions only in Rochette, and uncommon in Artuby. Pyroxene absorption band position is sensitive to Fe and Ca abundance (e.g., (*114*), and bands in the Máaz formation are centered between 900-1000 nm, consistent with Fe-rich pyroxenes. In the Artuby and Rochette members, spectra of natural surfaces are most consistent with Fe-rich augite (band centers near or beyond 1000 nm), and similar spectra are observed in dark gray grains across all Máaz abrasion patches. However, Ca-poor pyroxenes (pigeonite or Fe-rich orthopyroxene) may also be present, based on weak bands centered between 900-950 nm. In abrasion patches, these bands are associated with fine-grained black clusters, which show a clear mixing relationship with the red-stained, hematite-dominated matrix.

These results are generally in good agreement with PIXL results reported here, including the prevalence of Fe/Ca-rich pyroxene, feldspar, and Fe-oxides in Máaz formation rocks. Furthermore, while Mastcam-Z does not detect clear olivine signatures in the Máaz formation, PIXL results suggest that the majority of olivine present is heavily altered. The only significant discrepancy between the datasets is the lack of Ca-poor pyroxene in the Máaz formation in PIXL data. This could suggest that regions with weak orthopyroxene/pigeonite-like absorption bands actually correspond to a different ferric mineral, perhaps including ferric alteration products associated with serpentinization of olivine. These regions are often strongly oxidized, potentially supporting this hypothesis.

**PIXL minor phase analysis**

All PIXL analyses of Fe-Ti-Cr-oxides and Ca-phosphates are mixtures with other minerals due to their small grain sizes (less than, or close to PIXL's spot size of ~120 μm). As such, their compositions were inferred by examining mixing trends with surrounding phases, and correlations between major cations (Fe:Ti:Cr ratios for spinels, and Ca:P, P:Cl ratios for phosphates). Due to the small size and rarity of spinel and phosphate minerals, PIXL adaptive sampling protocols were implemented after Sol 424 that would increase dwell times on these phases, reducing the signal to noise ratio in the resulting spectra to improve data quality (*101*).

Mixing trend analyses presented in Figure S12 for Fe-Ti-Cr oxides indicate that Máaz PIXL scans are dominated by Fe-Ti oxides with Fe:Ti ratios that fall in between the ulvospinel-titanomagnetite solid solution. Due to mixing with surrounding Fe-silicates, the exact proportion of the titanomagnetite component is unconstrained at this time. The oxides have generally similar Fe-Ti-Cr compositions throughout the Máaz fm, excepting one chromite grain in *Montpezat* (see mixing trend towards the Cr apex of the ternary in Figure S12B), and a magnetite grain in *Alfalfa* (see mixing trend towards to Fe apex of the ternary in Figure S12A).

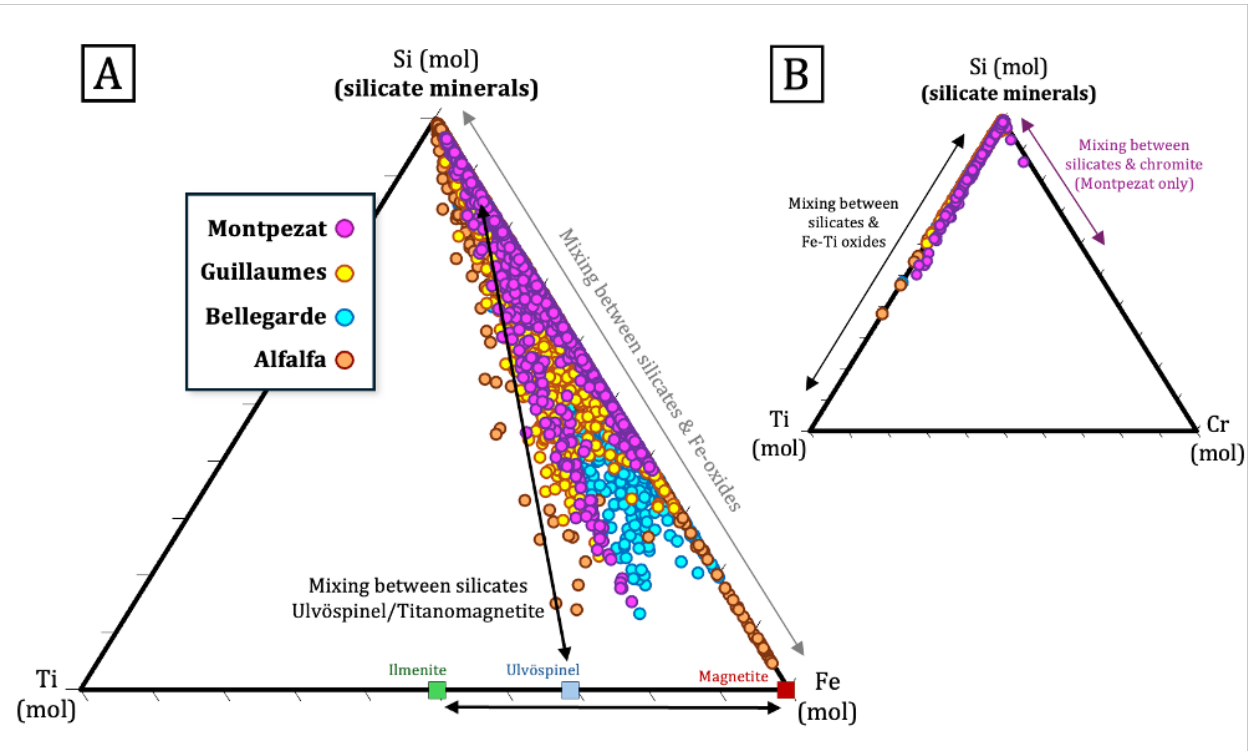


**Figure S12**. Ternary plots for the Máaz PIXL scans used to visualize mixing trends between Fe-Ti-Cr oxides and surrounding silicate phases using mols of A: Si-Ti-Fe, and B: Si-Ti-Cr. Due to the small size of the Fe-Ti-Cr oxides, all PMCs include some Si component (analysis spot includes a mixture of both an oxide and a silicate). By examining the Fe:Ti and Ti:Cr ratios the Si-poor points trend towards, the compositions of the oxide minerals can be inferred. The points for ilmenite ($FeTiO_3$), ulvöspinel ($Fe_2TiO_4$), and magnetite ($Fe^{2+}Fe^{3+}{}_2O_4$) are based on their ideal formulas. Titanomagnetite ($Fe_{3-x}Ti_xO_4$, where $0 < x \leq 1$) compositions exist between ulvöspinel and magnetite. Arrows on all plots are theoretical mixing trends between silicates and Fe-Ti-Cr oxides. Actual mixing trends are much more complicated due to differences in X-ray beam excitation volume for different elements (i.e., (*51*)).

Mixing trend analyses presented in Figure S12 for phosphates indicate that Máaz PIXL scans are dominated by Ca-phosphates with Ca:P ratios that span between apatite and merrillite with some points trending towards a phosphate phase with a Ca:P ratio ~1 (possibly a secondary phase like brushite) in *Bellegarde* and *Alfalfa*. In these two scans, there is also a slight positive correlation between P and Cl, indicating Cl-apatite may be present (Figure S13B).

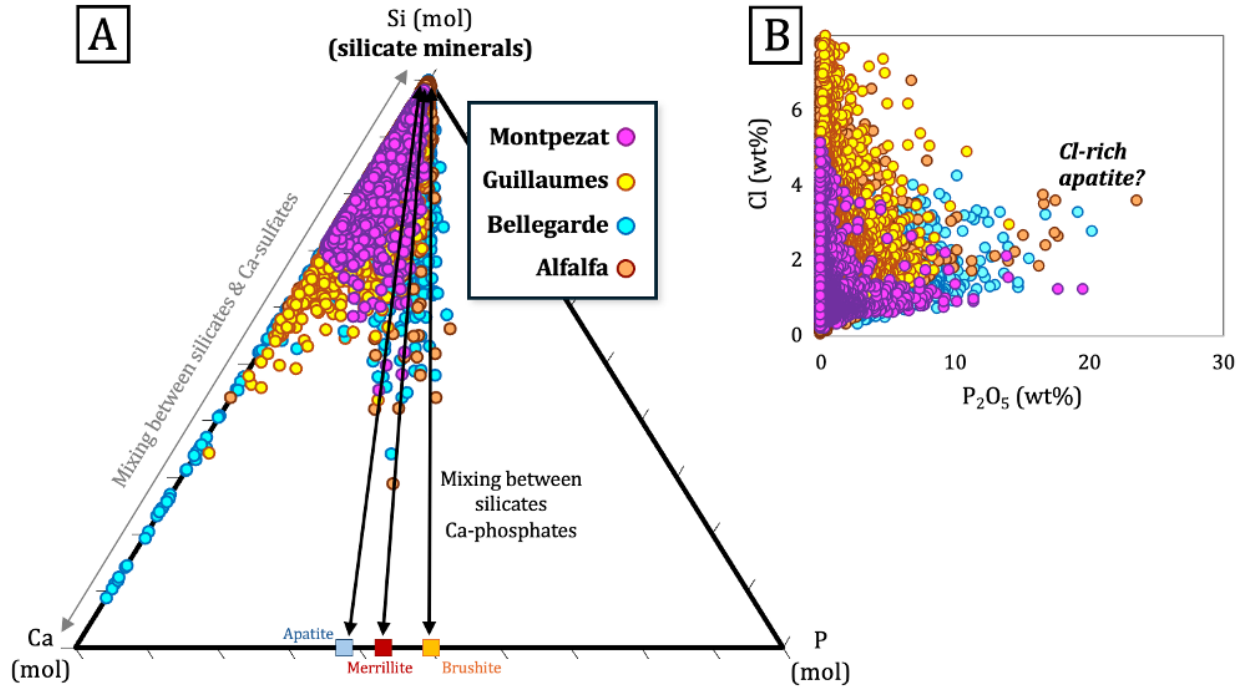


**Figure S13.** Plots to visualize mixing trends between Ca-phosphates and surrounding silicate phases. A: Ternary plot using mols of Si-Ca-P. B: Binary plot of Cl versus $P_2O_5$ (oxide wt%). Due to the small size of the phosphates, all PMCs include some Si component (analysis spot includes a mixture of both a phosphate and a silicate). By examining the Ca:P ratios the Si-poor points trend towards, the Ca:P-ratios of the phosphate minerals can be inferred. The points for apatite ($Ca_5(PO_4)_3(OH,F,Cl)$), merrillite ($Ca_9NaMg(PO_4)_7$), and brushite ($Ca(PO_3OH) \cdot 2H_2O$) are based on their ideal formulas. A slight positive correlation between Cl and P is observed in *Bellegarde* and *Alfalfa* (B) and may indicate a Cl-apatite component is present in these targets. Arrows on the ternary plot (A) are theoretical mixing trends between silicates and phosphate minerals. Actual mixing trends are much more complicated due to differences in X-ray beam excitation volume for different elements (i.e., (*51*)).

Zr-bearing phases are not definitively detected in Maaz PIXL scans. In the *Alfalfa* scan, spots with higher Zr (Figure S14) than seen elsewhere on the Jezero crater floor by PIXL may hint at the presence of Zr-bearing minerals at a scale smaller than the PIXL 1-signma spot size for Zr excitation energy (<80 µm; (*84*)). Due to the small size and rarity of Zr-rich minerals such as baddeleyite ($ZrO_2$) and/or zircon ($ZrSiO_4$), PIXL adaptive sampling protocols were implemented after Sol 424 that would increase dwell times on Zr-rich-phases in order to increase confidence in their detection (*101*).

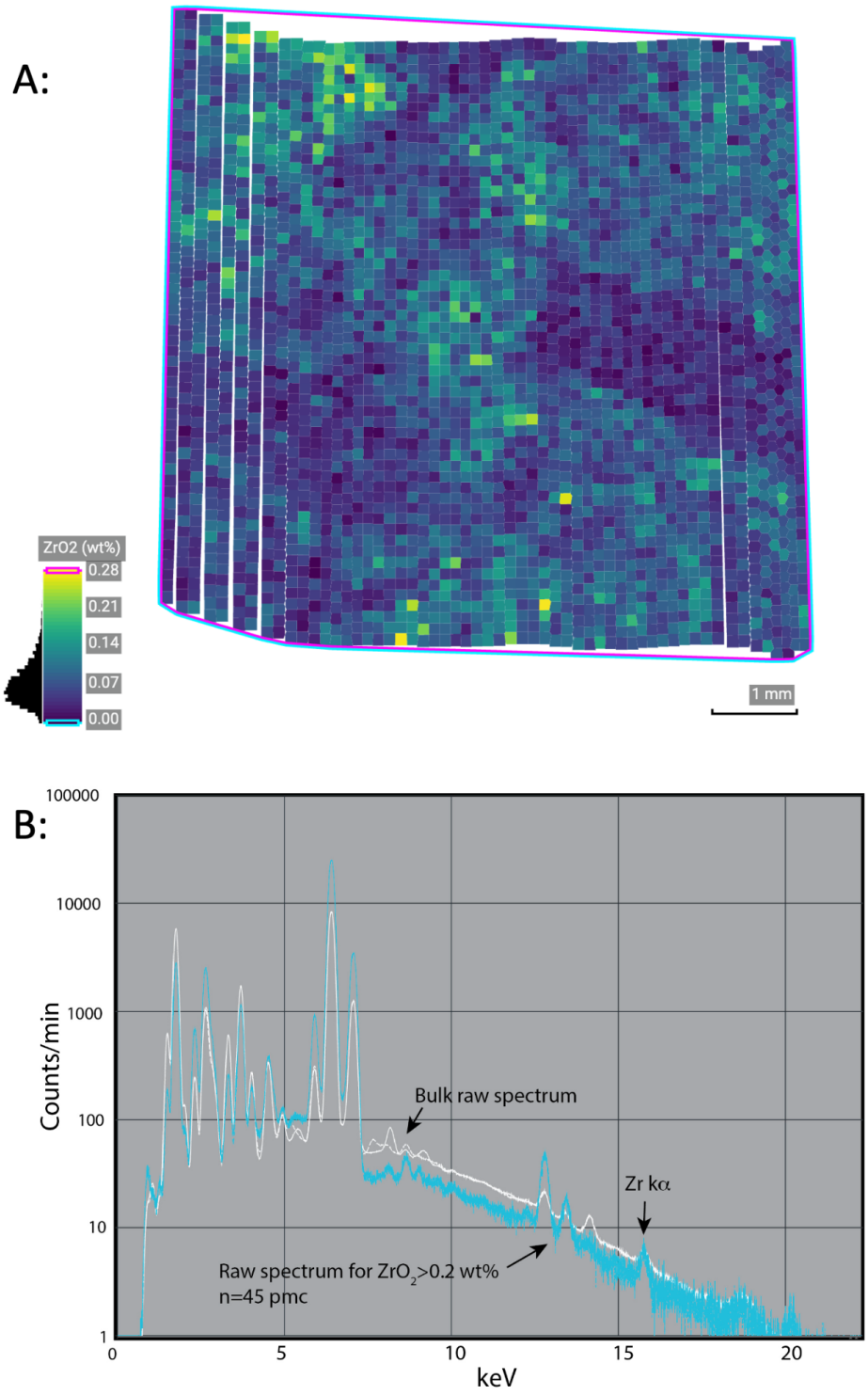


**Figure S14**. A: *Alfalfa* $ZrO_2$ map, corrected for topography and diffraction. Median standard error for $ZrO_2$ is 0.14 wt%. B: X-ray spectrum for *Alfalfa* showing a Zr Ka peak present in the bulk and the amalgamated spectrum for spots with >0.2 wt% $ZrO_2$ (n=45 PMC's).

## Oxygen fugacity estimate

Oxygen fugacity ($fO_2$) is the partial pressure of $O_2$ that is available to react in an environment. Magmatic $fO_2$ can strongly influence mineral stability, particularly the mixed valence Fe-oxides. To estimate magmatic $fO_2$ for the Máaz basalts, we use a modified method after (*10*) that found $fO_2$ for basalts examined by the Spirit Mars Exploration Rover (MER) in Gusev crater using elemental chemistry provided by the Alpha Particle X-ray Spectrometer (APXS) and iron mineralogy determined by Mössbauer spectrometer. For the Máaz basalts, we compared modal mineralogy determined by a combination of stoichiometric ratios and element thresholds (Table 3) and CIPW norm calculations for the igneous compositions (Table 1). We identified at what $Fe^{3+}/Fe_{total}$ do the modes and norms have equivalent (olivine)/(total oxide) ratios (Figure S15). We did not calculate $fO_2$ for *Alfalfa* because it does not produce normative olivine at any $Fe^{3+}/Fe_{total}$. The determined $Fe^{3+}/Fe_{total}$ was then applied to equations of (*115*) to find magmatic $fO_2$ (Table S8). The equations require assumptions of pressure, which was set at present day Mars atmospheric pressure (1150 Pa), and temperature, which is reported for near liquidus and near solidus conditions (T=1500 K and 1200 K, respectively). Generally, $fO_2$ is reported relative to a $O_2$ buffer reaction and here, results are presented as log units relative to the quartz–fayalite–magnetite (ΔQFM) buffer ($3Fe_2SiO_4 + O_2 = 2Fe_3O_4 + 3SiO_2$).

Máaz $fO_2$ estimates range from -1.09 to -2.82 ΔQFM at near liquidus temperatures and -1.47 to -3.21 ΔQFM at near solidus temperatures. These estimates are consistent with igneous $fO_2$ determined for the Adirondack tholeiitic basalts in Gusev crater (*10*) and basaltic and olivine-phyric shergottitic meteorites (e.g., (*9*).

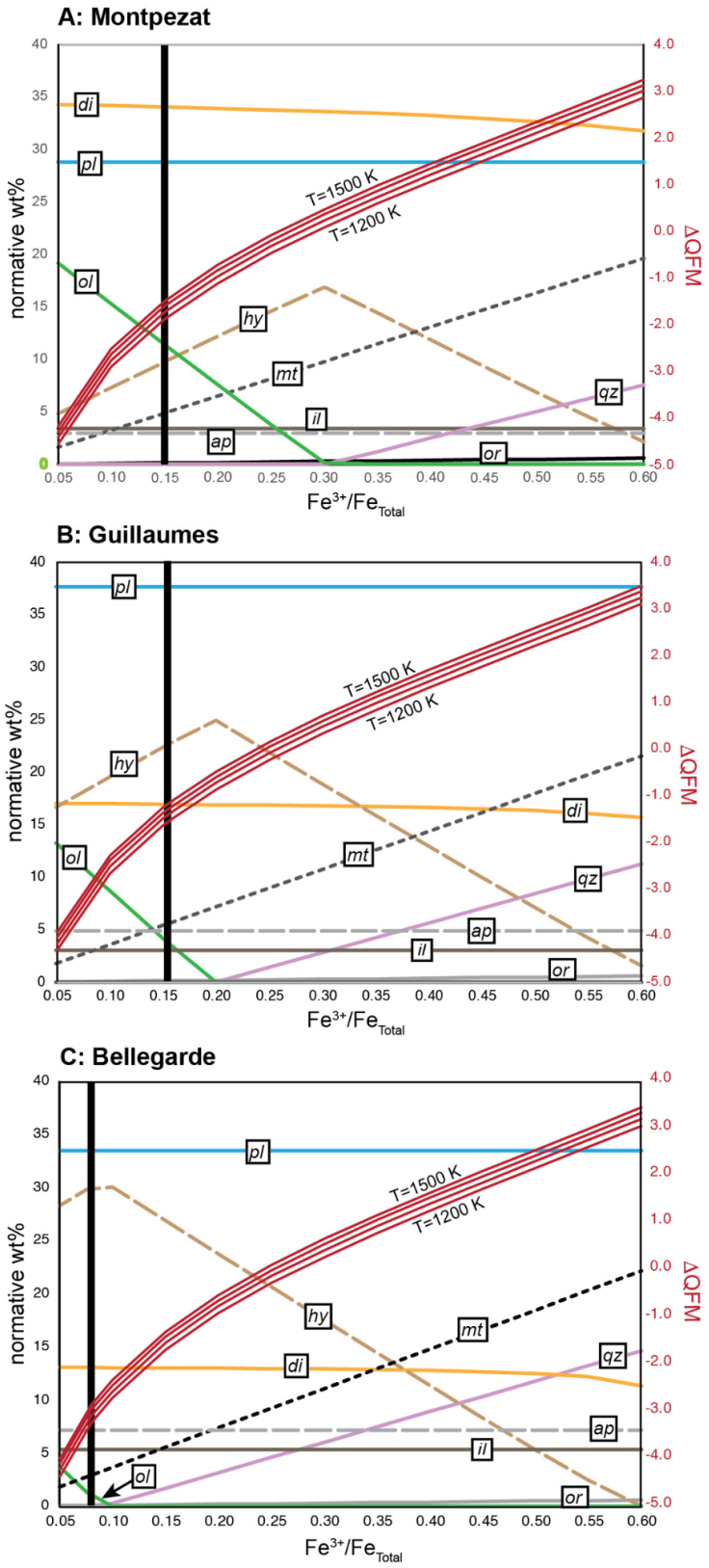


205
206 **Figure S15.** Plots of CIPW normative mineralogy vs. $Fe^{3+}/Fe_{Total}$ for the basaltic Máaz
207 targets. The $fO_2$ curves (red) are plotted as a function of $Fe^{3+}/Fe_{Total}$ for the target igneous
208 composition as log units relative to the Quartz-Fayalite-Magnetite buffer (ΔQFM).

Varying as a function of temperature, the $fO_2$ curves' temperatures range 1500 K to 1200 K and represent near-liquidus to near-solidus conditions, respectively. Heavy vertical line indicates $Fe^{3+}/Fe_{Total}$ where normative and modal olivine/(magnetite+ilmenite) ratios are equivalent, and best estimate for magmatic $fO_2$. A: Montpezat; B: Guillaumes; C: Bellegarde. Abbreviations are pl plagioclase, di diopside, hy hypersthene, mt magnetite, ol olivine, qz quartz, il ilmenite, ap apatite, or orthoclase.

**Table S8. Estimated $Fe^{3+}/Fe_T$[1] and ΔQFM[2] for Máaz fm basalts**

| | $Fe^{3+}/Fe_T$ | ΔQFM (T=1500 K) | ΔQFM (T=1200 K) |
|---|---|---|---|
| *Montpezat* | 0.15 | -1.58 | -1.90 |
| *Guillaumes* | 0.16 | -1.09 | -1.47 |
| *Bellegarde* | 0.08 | -2.82 | -3.21 |

[1] Determined by finding at what $Fe^{3+}/Fe_T$ value the CIPW normative olivine/total oxide equals modal olivine/total oxide.

[2] Calculated relative to the quartz–fayalite–magnetite (QFM) buffer (*116*) and solved using Eq. (7) of (*115*) at T = 1500 K (near liquidus) and T=1200 K (near solidus) and current Mars atmospheric pressure (P = 1150 Pa), where

$$ln\frac{X_{Fe2O3}}{X_{FeO}} = a\ln fO_2 + \frac{b}{T} + c + \sum_i d_i X_i + e\left[1 - \frac{T}{T_o} - \ln\frac{T}{T_o}\right] + f\frac{P}{T} + g\frac{(T-T_o)P}{T} + h\frac{P^2}{T}.$$

$X_i$ is the mole fraction of element *i*. We assume that $T = T_o$. Parameter values for this equation are $a = 0.196$; $b = 1.1492$ ° x $10^4$ K; $c = -6.675$; $d_{Al2O3} = -2.243$; $d_{FeOT} = -1.828$; $d_{CaO} = 3.201$; $d_{Na2O} = 5.854$; $d_{K2O} = 6.215$; $e = -3.36$; f $= -7.01°x10^{-7}$ $KPa^{-1}$; $g = -1.54°x10^{-10}$ $Pa^{-1}$; $h = 3.385$ °$x10^{-17}$ $KPa^{-2}$.

## Petrological Models

### *Perple_X*

Modeling of fractional and equilibrium crystallization was conducted for a liquid with the composition of *Montpezat* using the software PerpleX (*88*); version 6.9.0) with the thermodynamic database of (*117*); hpver633). We considered activity-composition (*a*-x) relationships for silicate melt, olivine, clinopyroxene, orthopyroxene, and spinel from (*118*), ilmenite from (*119*), and ternary feldspar from (*120*). All models were run at 0.1 GPa with starting compositions containing 0 and 1 wt.% $H_2O$ and $Fe^{3+}/Fe_{total}$ ratios of 0.05, 0.10, and 0.15, corresponding to ΔQFM between -2.6 and -1.0 at 0.1 GPa and 1300 °C based on the parametrization of (*115*)). Calculations were also run at 1 bar, but differences with the models presented here, in terms of phase compositions and liquidus temperatures, were negligible. Calculated liquid lines of descent are plotted as a function of MgO content in Figures 7 (main text) and S16.

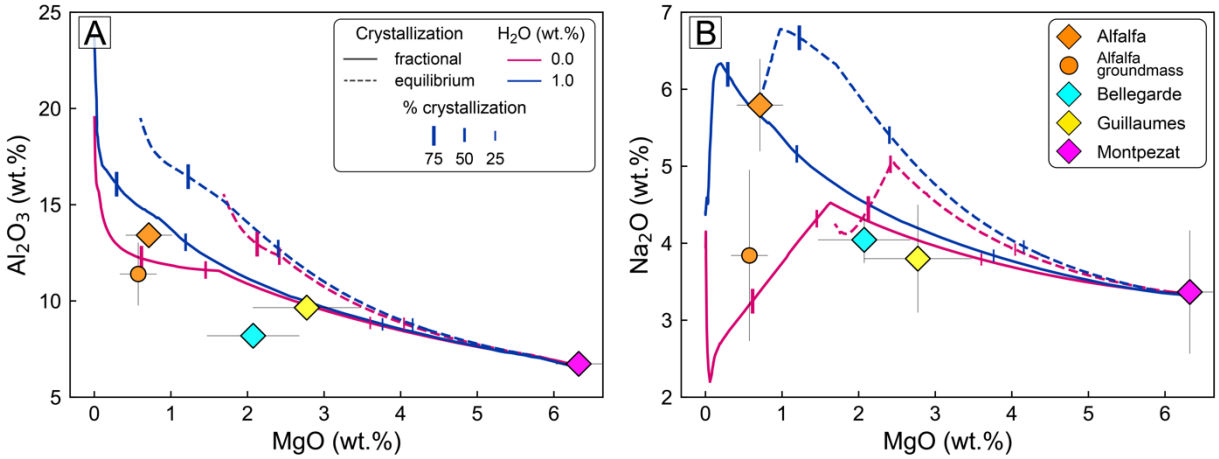


**Figure S16.** Equilibrium and fractional crystallization PerpleX models(*88*); version 6.9.0) of a Montpezat parental magma. Crystallization trajectories and Máaz igneous compositions presented on plots of A: $Al_2O_3$ and B: $Na_2O$ vs. MgO (weight%). Máaz igneous compositions are renormalized to 100% without $P_2O_5$ and MnO to be consistent with the calculated LLD since the model does not include $P_2O_5$ and MnO.

The "effective" liquidus temperatures are at 1276 °C and 1224 °C for the dry and wet compositions considered (Figure S17). For Montpezat, the "effective" liquidus refers to the temperature at which augite starts to crystallize. Minute amounts of spinel are often predicted at supra liquidus temperatures, which is a common artifact of some thermodynamic models (*90*, *118*, *121*). The solidus temperatures for equilibrium crystallization are 1025 °C and 854 °C for the dry and wet starting compositions, respectively. For fractional crystallization, the solidus is at 924 °C for the dry liquid composition and less than 800 °C for the composition starting with 1.0 wt.% $H_2O$.

For a $Fe^{3+}/Fe_{total}$ ratio of 0.10, the starting augite composition for the dry and wet compositions is, respectively, $Wo_{28}Fs_{22}En_{50}$ and $Wo_{34}Fs_{21}En_{45}$. Augite becomes progressively more enriched in the wollastonite and ferrosilite components as the liquid crystallizes. With the dry liquid composition, the augite composition after almost complete liquid crystallization is ~$Wo_{44}Fs_{30}En_{26}$, with an instantaneous composition for fractional crystallization of $Wo_{50}Fs_{50}En_0$. Similarly, near the solidus, crystallization of the starting composition with 1.0 wt.% water yields augite ~$Wo_{45}Fs_{28}En_{27}$, where the instantaneous composition at near complete fractional crystallization is ~$Wo_{50}Fs_{50}En_0$.

Following augite, olivine joins the crystallization assemblage at temperatures that vary with the initial oxidation state and $H_2O$ content of the system. olivine starts crystallizing at ~1220 °C and ~1180 °C for the dry and wet starting compositions in both equilibrium and fractional crystallization. The starting olivine is Fo ~60 and evolves toward more Fe-rich compositions as crystallization occurs. When crystallization is nearly complete, equilibrium and fractional crystallization produce olivine composition with Fo ~30. In the latter case, the instantaneous olivine composition at the last stages of crystallization is nearly pure fayalite.

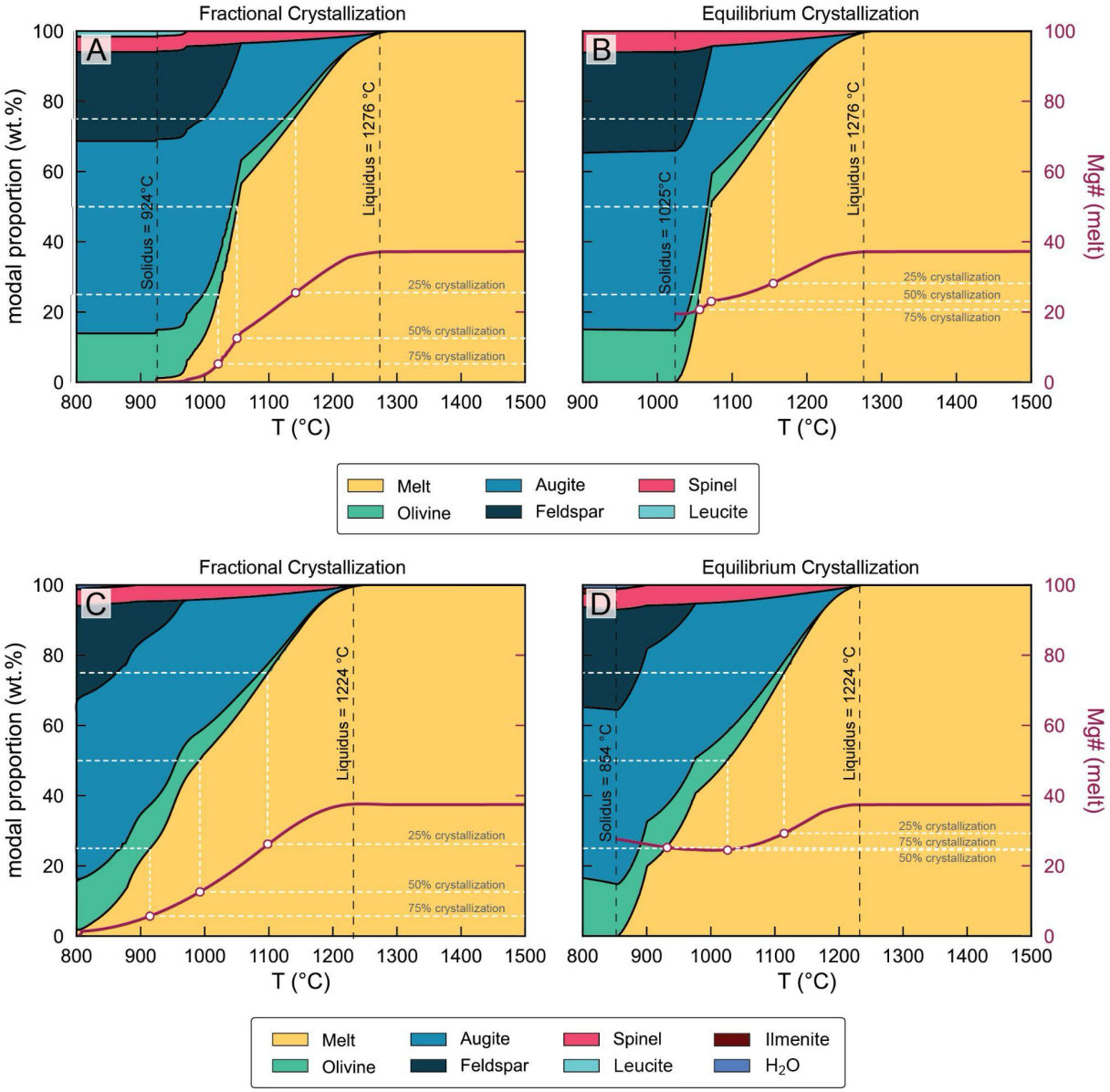


**Figure S17.** Mineral modal proportions (weight %) determined by equilibrium and fractional crystallization PerpleX models ((*88*); version 6.9.0) of a *Montpezat* parental magma. Plots A and B present calculated modes as a function of temperature for anhydrous starting parental melt calculated for fractional and equilibrium crystallization, respectively. C and D are plots of modes vs. temperature determined for fractional and equilibrium crystallization models, respectively for a *Montpezat* parent magma with 1 wt% $H_2O$.

Feldspar is formed at ~1060 °C during fractional and equilibrium crystallization for the dry starting composition, while its crystallization is delayed to temperatures of ~970 °C for the starting compositions containing $H_2O$. With the dry starting composition, the initial felspar is ~$Ab_{86}An_{11}Or_3$, which evolves to ~$Ab_{70}An_{20}Or_{10}$ during equilibrium crystallization and reach an instantaneous composition of ~$Ab_{18}An_{81}Or_1$ near the solidus during fractional crystallization. The wet starting composition produces an initial felspar with ~$Ab_{75}An_{23}Or_2$, evolving to ~$Ab_{70}An_{20}Or_{10}$ upon full crystallization. In contrast, fractional crystallization yields ~$Ab_{60}An_{39}Or_1$ at the onset of feldspar crystallization, reaching an instantaneous composition of ~$Ab_{45}An_5Or_{50}$

close to the solidus. Other minor phases produced when crystallization is nearly complete include leucite for dry fractional crystallization and ilmenite for the starting composition with 1.0 wt.%.

Variations in the oxidation state of the starting composition have a minor effect on the liquidus and solidus temperatures, with temperatures lower by ~10-20 C for higher $Fe^{3+}/Fe_{total}$ ratios. However, the olivine-liquid temperatures decrease from 1237 °C to 1203 °C with $Fe^{3+}/Fe_{total}$ increasing from 0.05 to 0.15, which means olivine joins the equilibrium assemblage at progressively lower temperatures as the oxidation state of the starting liquid increases. Moreover, higher $Fe^{3+}/Fe_{total}$ ratios also result in higher proportions of spinel, which lowers FeOt contents in the liquid during crystallization. It is well known that existing thermodynamic relationships may overestimate spinel crystallization (e.g., (*90*), which may account for liquid lines of descent below the crystallization path defined by *Guillaumes* and *Bellegarde* in FeOt-MgO space.

Residual $H_2O$ contents are plotted as a function of percent crystallization in Figure S18.

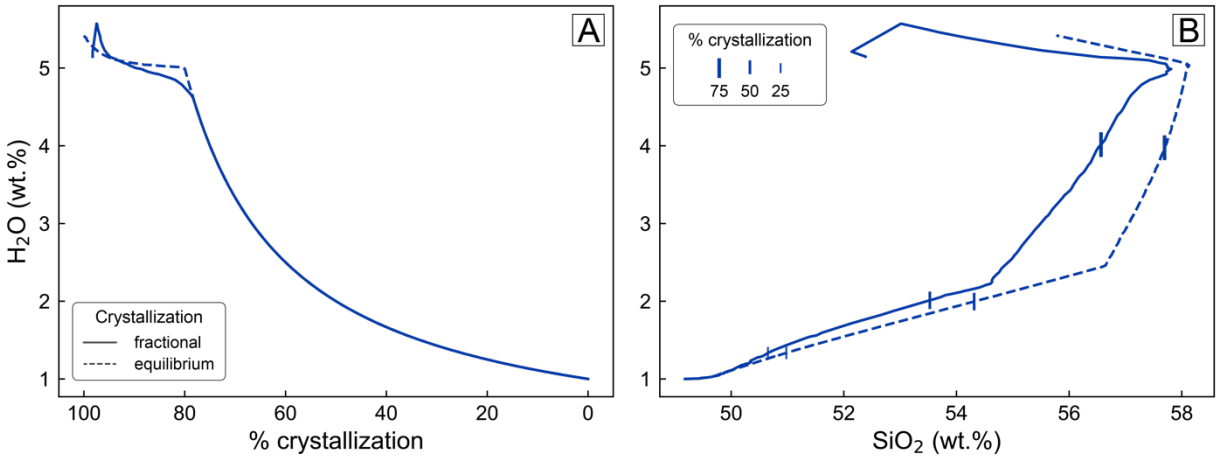


**Figure S18.** Dissolved $H_2O$ enrichment calculated by equilibrium and fractional crystallization PerpleX models(*88*); version 6.9.0) presented on plots of A: $H_2O$ (wt%) vs. percent crystallization, and B: dissolved $H_2O$ (wt%) vs. $SiO_2$.

***Magma Chamber Simulator (MCS)***

Magma Chamber Simulator, or MCS (*89*), was used to model the fractional crystallization of liquids with compositions of *Montpezat*. MCS is a thermodynamic model that calculates the evolution of magma throughout crystallization under open-system conditions. It utilizes the rhyolite-MELTS and pMELTS algorithmsv(*122–124*) for fractional crystallization calculations. It is able to model fractional crystallization, assimilation, and magma recharge. For the fractional crystallization models, only the FC portion of the model was used. All runs were done at 0.1 GPa, at a starting $fO_2$ of QFM -2.6, under both hydrous (1 wt.% $H_2O$) and anhydrous conditions.

The starting composition was that of *Montpezat* (Table 1). The MCS liquidus temperatures ranged from ~1260°C (with a phosphate as the liquidus phase) for the anhydrous (AH) run, to ~1160°C for the hydrous (H) runs. The first major phase to crystallize is olivine, at ~1180°C (AH) and 1160°C (H), followed by spinel at 1160°C (AH) and 1130°C (H), and then clinopyroxene (augite) at 1160 (AH) and ~1105°C (H). Feldspar is the last phase to form at ~1075°C and 1010°C, although minor amounts of phosphates crystallize in both the hydrous and anhydrous runs. For the anhydrous runs, olivine ranges in composition between $Fo_{65-5}$, while for hydrous runs, it ranges

between $Fo_{65-3}$. Both runs crashed before reaching the solidus, which is ~880°C for the anhydrous run, and ~700°C for the hydrous run. MCS liquid lines of descent are plotted on Figure S19 for comparison with Perple_X results in Figure 7 (main text).

Similar to Perple_X, it is recognized that MELTS overestimates spinel stability and overestimates the partitioning of $Fe_2O_3$ in minerals. Additionally, in the anhydrous runs, the high liquidus temperatures may be inaccurate given the liquidus phase is a phosphate which likely has to do with the program needing to place the high amount of $P_2O_5$ in the most stable phase.

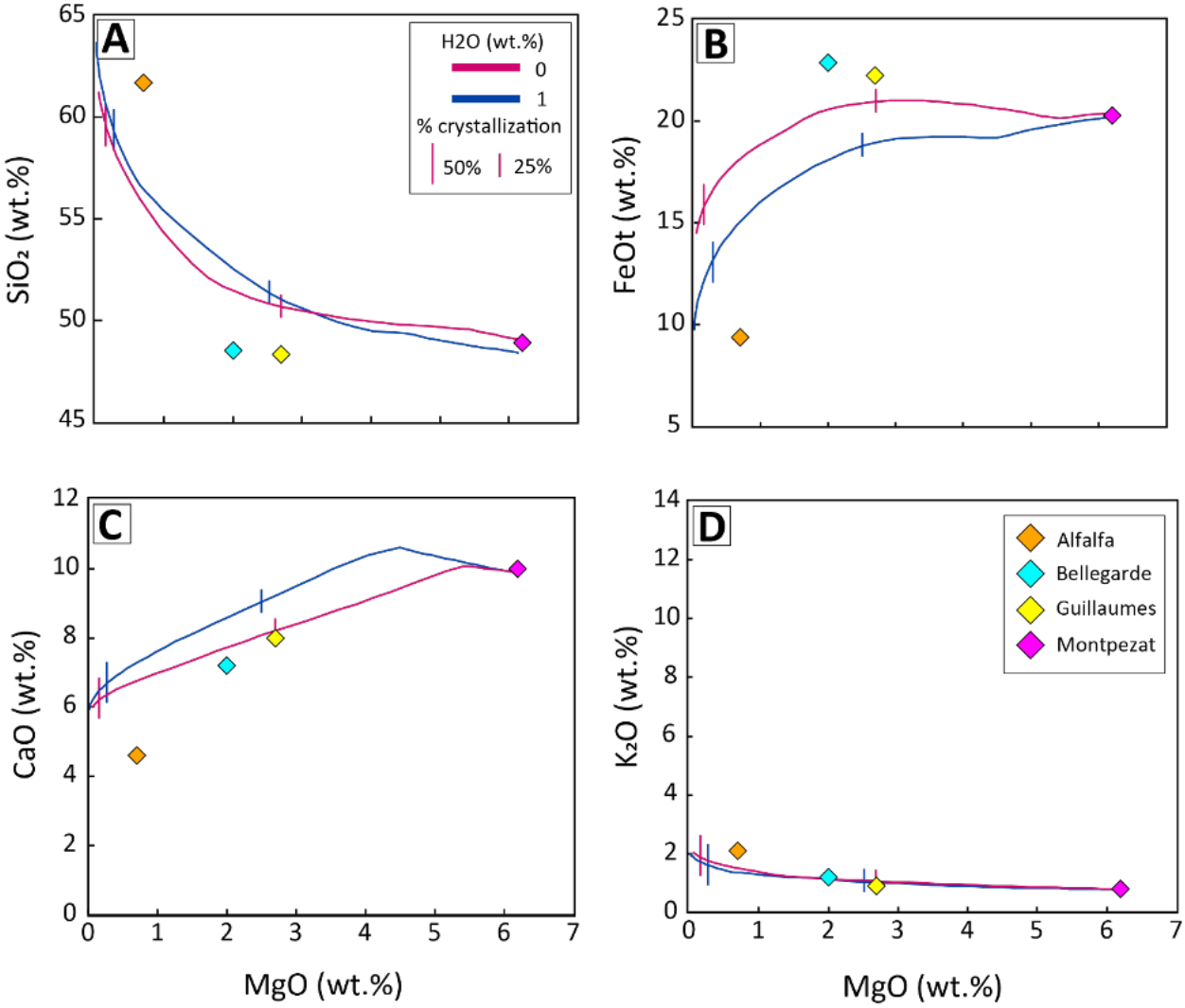


**Figure S19.** Liquid lines of descent (LLD) for hydrous and anhydrous fractional crystallization models using Magma Chamber Simulator (*89*) for comparison with results of PerpleX crystallization models (Figure 7, main text). The starting composition was that of Montpezat (Table 1). LLDs for select oxides: (A) MgO vs. $SiO_2$, (B) MgO vs. FeO, (C) MgO vs. CaO, and (D) MgO vs. $K_2O$. The values of the various igneous Máaz targets are also shown.

***Comparison between petrological models***

To date, petrological models and activity-composition relationships for phases relevant to crystallization of silicate magmas have been calibrated from experiments that encompass mostly

terrestrial compositions. Results from these models may therefore have larger uncertainty when applied to modeling the crystallization of Martian basalts. Here, we used two different, but widely used, models to simulate crystallization of the *Montpezat* composition under similar assumptions. While both models predict similar trends in the evolution of the produced melts, there are some major differences in their chemistry and olivine-liquid temperatures. Notably, MCS predicts olivine at temperatures of ~1160-1180 °C, whereas Perple_X yields augite as the liquidus phase at 1224-1276 °C. This contrasting prediction is significant for fractional crystallization since it results in differences in the liquid composition as crystallization progresses. For example, at ~50% fractional crystallization of the anhydrous *Montpezat* composition, the predicted $SiO_2$ content of the residual magma is ~54 wt.% with Perple_X, whereas the MCS calculations yields ~60 wt.%. Likewise, relative to MCS, larger extents of fractional crystallization are required in Perple_X to reach liquid compositions with FeO and MgO contents like those of *Bellegarde* and *Guillaumes*.

As both modeling approaches yielded similar results, the choice to prefer Perple_X came down to its higher liquidus temperature and augite-bearing near liquidus mineral assemblage more closely resembling phases identified in the Máaz rocks. In addition, a recent study (*125*) found that Perple_X more accurately reproduces multiple saturation points determined experimentally for martian and lunar primary basalts.

**Martian Meteorites**

The petrologic textures and mineral compositions of the Máaz targets analyzed by PIXL are most similar to Fe-rich basaltic shergottites. However, the majority of the Máaz targets analyzed by PIXL are far more enriched in Fe and alkalis (Figure 4, main text). The Mg#s of *Guillaumes*, *Bellegarde*, and *Alfalfa* are 18, 14, and 11, respectively; much lower than the most Fe-rich martian meteorite Los Angeles (Mg# 23-25; (*27*, *126*). The bulk composition of *Montpezat* yields an Mg# of 35, making it the most Mg-rich of the Máaz lithologies and in the typical range of basaltic shergottites (Mg#s 23-58; (*127*). Augite-rich shergottites such as NWA 8159 (*128*) are also relatively Fe-rich (bulk Mg#s of 25–27; (*127*), but have fine-grained ophitic to sub-ophitic textures (pyroxene and plagioclase are ~200 μm in size), much finer than Máaz basalts (Figure S20).

Fe-rich basaltic shergottites are typically coarse-grained, and are dominated by plagioclase and pyroxene up to 5 mm in size with ophitic to sub-ophitic textures (*27*, *43–45*); Figure S20). The Máaz targets analyzed by PIXL have grain sizes ranging between 0.3 to 3 mm for the major rock forming minerals (Table 3, main text), making them finer-grained than Fe-rich basaltic shergottites (Figure S19). PIXL element maps may reveal ophitic to sub-ophitic textures in portions of the *Guillaumes*, *Bellegarde*, and *Montpezat* targets where small plagioclase grains appear enclosed, or partially enclosed in pyroxene (Figure S20). However, the large volume of fine-grained K-rich groundmass across Máaz (Figure 2, main text), and the high abundances of Fe-Ti oxides in *Guillaumes* and *Bellegarde* are inconsistent with basaltic shergottites' mineralogy and textures. Vesicles are also observed in *Guillaumes* and *Bellegarde*, while no primary igneous vesicles (not shock-produced) have been identified in basaltic shergottites.

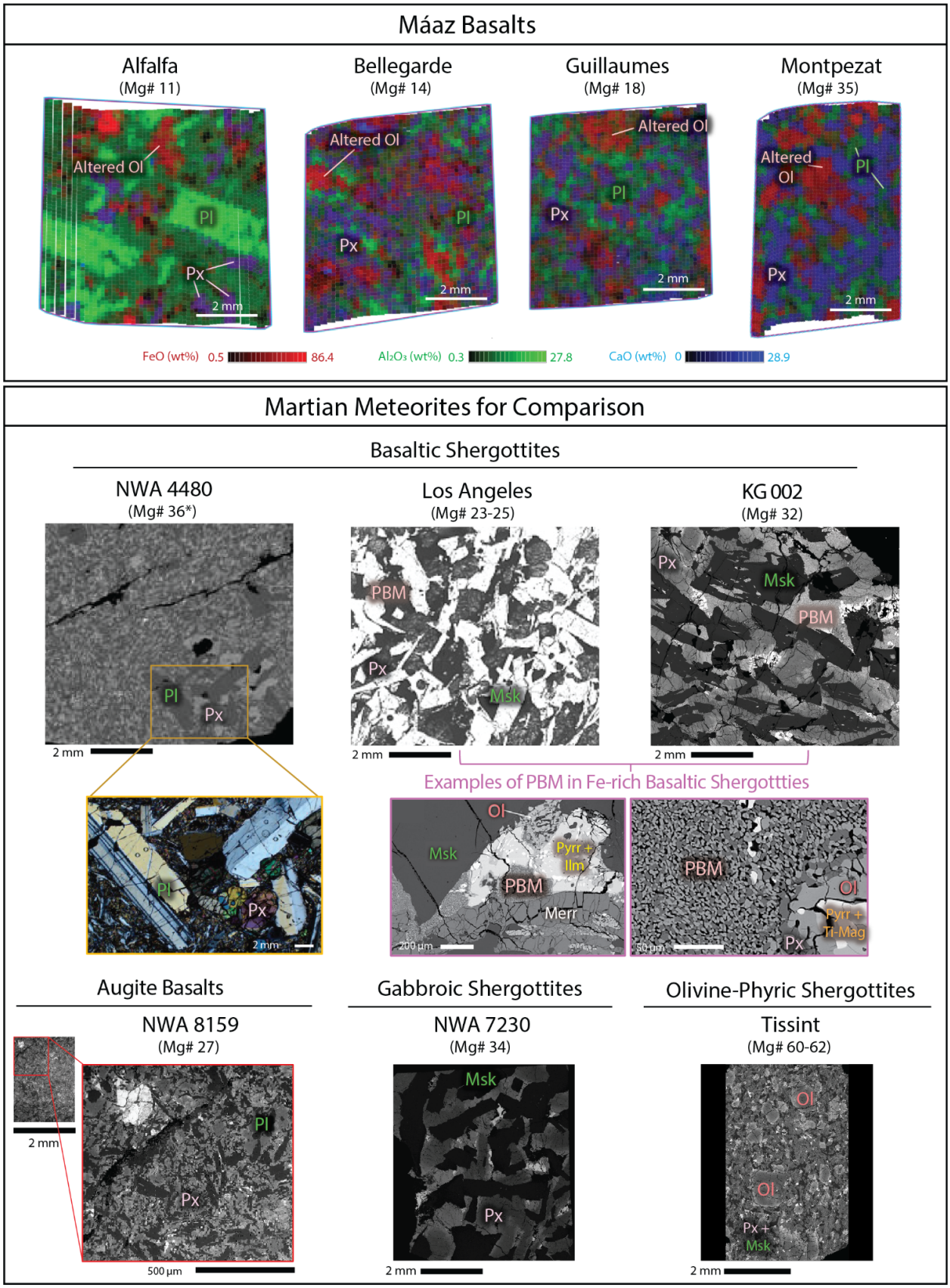


**Figure S20.** Comparison between textures of the Máaz fm abraded targets and martian meteorites. All maps and images (excluding insets) have the same scale for easier texture

and grain size comparisons. Máaz fm textures are shown in the top row using PIXL Red-Green-Blue (RGB) maps for FeO, $Al_2O_3$ and CaO corrected for effects of topography and diffraction. Northwest Africa (NWA) 4480 textures are shown using a backscattered electron (BSE) image (after (*129*)), and an inset of plagioclase glomerocrysts in cross-polarized light (credit: T. Kizovski). Los Angeles textures are shown using a transmitted light image (after (*27*). Ksar Ghilane (KG) 002 textures are shown using a BSE image (after (*29*). Examples of Pyroxferroite Breakdown Material (PBM) typically found in Fe-rich basaltic shergottites including Los Angeles and KG 002 are shown as BSE images from KG 002 (after (*43*). Typical augite basalt textures are shown using a BSE image from NWA 8159 (after (*128*). Typical gabbroic shergottite textures shown using a BSE image from NWA 7320 (after (*75*). Typical olivine-phyric shergottite textures shown using a BSE image of Tissint (credit: Y. Liu). Mineral acronyms for each image: Ilm = Ilmenite, Merr = Merrillite, Msk = Maskelynite (shocked plagioclase glass), Ol = Olivine, PBM = Pyroxferroite Breakdown Material, Px = Pyroxene, Pl = Plagioclase, Pyrr = Pyrrhotite, Ti-Mag = Ti-Magnetite.

The Ca-Fe-rich pyroxene compositions in the Máaz targets ($Wo_{31.8\text{-}25.8}En_{5.6\text{-}25.7}Fs_{39\text{-}66.5}$; Table 2, main text) are similar to those reported in Fe-rich basaltic shergottites such as Los Angeles (*44*, *45*) and Ksar Ghilane (KG) 002 (*43*). However, these extremely Fe-rich compositions are only observed on the rims of zoned clinopyroxene grains in the basaltic shergottites, which have relatively Mg-rich, Fe-poor cores (i.e., Los Angeles pyroxene compositions: Cores = $Wo_{33}En_{40}Fs_{27}$, Rims = $Wo_{15}En_5Fs_{80}$ (*44*). No zoning was observed in Máaz pyroxenes at the resolution of PIXL scans, indicating that they may have crystallized from a melt significantly enriched in Fe in comparison to known martian meteorites, and/or significant equilibration occurred.

Olivine is a minor component in both the Fe-rich basaltic shergottites (i.e., 1.9% modal in Los Angeles; (*44*) and Máaz basalts (3-10%, Table 3, main text). Olivine compositions are also extremely fayalitic in both Máaz ($Fo_{3.1\text{-}20.3}$, Table 2 main text) and the Fe-rich basaltic shergottites (~$Fo_{10}$ and lower; (*43–45*), but textures differ greatly. Olivine in Máaz has been extensively altered to Fe-rich serpentine minerals (see main text), and occurs as relict grains up to 2 mm in size. Conversely, the minor olivine observed in Fe-rich basaltic shergottites most often occurs as ~5-10 μm grains in vermicular to microgranulitic intergrowths of pyroxferroite breakdown materials (PBM - intergrowths of fayalite + hedenbergite + silica that form due to the breakdown of Fe-rich pyroxferroite with cooling; (*43–45*). As noted in the main text, regions of contiguous diffraction indicate relict olivine grains in Máaz are crystalline and are not fine-grained breakdown products of pyroxferroite.

The *Alfalfa* target is unique among the Máaz basalts, with a distinctly porphyritic texture (see main text). *Alfalfa* comprises large plagioclase laths ($An_{31.6}Or_{5.1}$, >3 mm in the longest dimension) embedded in a fine-grained K-rich groundmass (Figure 7, main text). Similar textures are rare in martian meteorites, with the exception of basaltic shergottite NWA 4480, which contains large plagioclase glomerocrysts ($An_{58.4\text{-}61.0}Or_{1.6}$, significantly more Ca-rich than *Alfalfa* plagioclase, and ~2 mm in the longest dimension) embedded in a fine-grained matrix of pyroxene, olivine and plagioclase (Figure S20). Data on this meteorite is limited to a few abstracts (*129–131*), but no K-rich groundmass has been reported. The only bulk chemical data for NWA 4480 is from its fusion crust, which yields an Mg# of 36 (*131*), much higher than the Mg# for *Alfalfa* and the majority of the Máaz basalts. In comparison to Fe-rich basaltic shergottites, plagioclase in Máaz is relatively

444 rich in Na and K (i.e., Los Angeles Plagioclase = $An_{57-40}Or_{1-8}$ (*44*), Máaz = $An_{18.6-38.2}Or_{4.8-14.5}$;
445 Table 2, Figure 3, main text).
446
447